Identification of τ Leptons from Single $\mathbf{W} \to \tau\nu_\tau$ Production with the ZEUS Detector

Diplomarbeit
von
Chi Nhan Nguyen

Institut für Experimentalphysik der Universität Hamburg

25. April 2002

Abstrakt

Es wurde eine Suche nach Ereignissen, in denen ein einzelnes $W^{\pm}$-Boson direkt produziert wird und in ein hadronisch zerfallenes τ lepton zerfällt, mit dem ZEUS Detektor bei HERA durchgeführt. Der untersuchte Datensatz entspricht einer integrierten Luminosität von $\mathcal{L} = 65.5$ pb^{-1}, die in Positron-Proton-Kollisionen aus den Jahren 1999 und 2000 aufgezeichnet wurden. Die größte Herausforderung war die Trennung von Jets, die durch τ-Leptonen induziert werden, von solchen, die durch Quarks oder Gluonen hervorgerufen werden. Zu diesem Zwecke wurde eine Trennungsmethode benutzt, die sechs verschiedene Observablen, die die Eigenschaften des Jets charakterisieren, zu einer kombinierten Größe zusammenfaßt. Bei einer Effizienz von $\epsilon = 33\%$ wurde ein Trennungsvermögen von $S = 211$ erreicht, welches einer Untergrundunterdrückung von $R = 639$ entspricht. Im Vergleich zu einer publizierten ZEUS-Analyse wurde das Trennungsvermögen um einen Faktor von mindestens drei verbessert. Aufgrund des sehr kleinen Wirkungsquerschnitts von $W^{\pm}$-Boson-Prozessen bei HERA, zusammen mit der erzielten Effizienz und dem erzielten Trennungsvermögen, wird kein Signal erwartet. Nichtsdestotrotz wurden zwei Ereignisse gefunden, die alle Anforderungen erfüllen. Die Beobachtung dieser zwei Ereignisse entspricht einer Wahrscheinlichkeit von 0.45% nach Poisson Statistik, wenn man die erwarteten $W^{\pm}$-Boson-Ereignisse und den CC DIS Untergrund berücksichtigt. Diese zwar geringe Wahrscheinlichkeit ist nicht klein genug, daß man von einem signifikanten Überschuß in den Daten reden kann. Jedoch sind die gemessenen Ereignisse sehr vielversprechend und besitzen Merkmale, die möglicherweise durch Prozesse jenseits des Standardmodells hervorgerufen werden können.

Abstract

A search for single $W^{\pm}$ boson production events with the subsequent decay $W \to \tau\nu_{\tau}$, where the τ lepton decays hadronically, has been performed with the ZEUS detector at the positron proton collider HERA. The data sample corresponds to an integrated luminosity of $\mathcal{L} = 65.5$ pb^{-1} collected in the years 1999 and 2000. The major challenge was the separation of τ lepton induced jets from gluon and quark induced jets. For this purpose a multiobservable discrimination technique was applied, which combined six jet observables characterising the jet properties in a single quantity. For an efficiency of $\epsilon = 33\%$ a separation power of $S = 211$ has been achieved, which corresponds to a background rejection of $R = 639$. Compared to a published ZEUS analysis the separation power has been improved by a factor of at least three. Due to the very small cross section of single $W^{\pm}$ boson production at HERA no signal is expected, since for a high signal efficiency the background rejection is not sufficient. However, two events were found which passed all final cuts. These two observed events corresponds to a Poisson probability of only 0.45%, with respect to the expected number of single $W^{\pm}$ boson production events and the CC DIS background. This is not small enough to state that one has found a significant excess in the data. However, these two events are promising and have a striking signature. They might be due to phenomena beyond the Standard Model.

Contents

1 Introduction **7**

2 Motivation **8**

2.1 The Standard Model of Particle Physics 8

2.1.1 Electroweak Interaction 9

2.1.2 Quantum Chromodynamics 10

2.1.3 Limitations of the Standard Model 10

2.2 Lepton Nucleon Scattering 11

2.3 Single $W^{\pm}$ Boson Production and Events with an isolated high-energy Lepton and Missing Transverse Momentum at HERA . . . 14

2.4 Motivation for the Search for $W \to \tau\nu_{\tau}$ 16

3 Search Strategy **18**

3.1 Single $W^{\pm}$ Boson Production with subsequent Decay $W \to \tau\nu_{\tau}$ . . 18

3.2 Background processes 22

3.2.1 Photoproduction 22

3.2.2 Neutral Current DIS 24

3.2.3 Charged Current DIS 24

3.2.4 Lepton Pair Production 24

3.2.5 Z^0 Boson Production 25

3.3 Search Strategy 26

4 HERA and the ZEUS Detector **27**

4.1 The HERA Collider 27

4.2 The ZEUS Detector 29

4.2.1 The Central Tracking Detector 30

4.2.2 The Calorimeter 32

4.2.3 Luminosity Monitor 33

4.2.4 Trigger System and Data Acquisition 34

5 Monte Carlo Simulation **36**

5.1 Event Generators and Detector Simulation 36

5.2 Monte Carlo Samples 36

6 Discrimination Technique **40**
6.1 Jet Classification 40
6.2 The Discrimination Method 41
6.3 The Range Searching Algorithm 43

7 Identification of τ Leptons **45**
7.1 The Decay of τ Leptons 45
7.2 Characteristics of τ Jets 45
7.3 Definition of Observables characterising τ Jets 47
7.4 Separation of τ Jets from QCD jets 53
7.4.1 Preselection 53
7.4.2 Optimisation of the Separation 57
7.5 Results 65

8 Data Analysis - 1999-2000 e^+p **67**
8.1 Definition of Global Event Variables 67
8.2 Event Selection 68
8.2.1 Trigger 68
8.2.2 Offline 70
8.2.3 Comparison of Data and Monte Carlo Simulation 74
8.3 Results 76
8.3.1 Final Cuts 78
8.3.2 Discussion of the Selected Events 80

9 Summary **87**

A Definition of Jets **89**

B Separation of τ Jets from QCD Jets **90**

Chapter 1

Introduction

In the last decades collider experiments all around the world have played a crucial role for a better understanding of the structure of matter. The Standard Model of Particle Physics, developed with the help of many experimental and theoretical physicists, has been very successful in describing the interactions of the fundamental particles. Even though this theory has been tested with high accuracy, it is considered that the Standard Model is only a low-energy approximation to a more fundamental theory, since many fundamental questions can not been answered by the Standard Model. It is hoped that at present high energy colliders like HERA and even more at future high energy projects, such as LHC or TESLA, phenomena beyond the Standard Model can be discovered.

The H1 Collaboration at the HERA electron-proton collider with a center-of-mass energy of $\sqrt{s} = 318$ GeV has reported the observation of isolated lepton events with large missing transverse momentum. While some of those events can be explained by expected properties of single $W^{\pm}$ boson production with a subsequent electronic or muonic decay, six events with muons observed by H1 show properties atypical for such Standard Model processes. On the other hand the ZEUS Collaboration, which performed a similar analysis, could not observe such kind of striking events in both, the electron and muon channel.

The ZEUS and the H1 Collaborations yet have not searched for such events in the τ channel, since the background in such events is difficult to control. In this analysis the ZEUS e^+p data collected in the years 1999 to 2000 will be used to search for single $W^{\pm}$ boson production events, where the $W^{\pm}$ boson decays into a τ lepton and a neutrino and the τ lepton decays hadronically. Any observed deviation from the Standard Model predictions could be an indication for new physics beyond the Standard Model. The major challenge will be the discrimination of τ lepton induced jets from QCD induced jets. Therefore, a multivariate discrimination technique is used.

Chapter 2

Motivation

The main reasons to start the difficult search for single $W^{\pm}$ boson production events with subsequent hadronic decay of the τ lepton is presented in this chapter. An outline of the most important theoretical and general experimental aspects is given. The chapter begins with an overview of the Standard Model of Particle Physics and general considerations concerning lepton nucleon scattering, followed by an introduction to two crucial analyses of the ZEUS and the H1 collaborations. The results of these analyses are the main motivation for this work.

2.1 The Standard Model of Particle Physics

The world as known today is formed by fundamental particles with spin 1/2, called fermions, which constitute the matter, and fundamental forces, mediated by gauge bosons with spin 1. The matter particles are quarks, which form the hadrons and the leptons. They come in families with three generations (see Table 2.1). The forces are the electromagnetic, the weak and the strong force listed in Table 2.2. The inclusion of the gravitational force is not yet understood.

	1.	**2.**	**3.**	**forces**
Leptons	$\begin{pmatrix} \nu_e \\ e \end{pmatrix}$	$\begin{pmatrix} \nu_\mu \\ \mu \end{pmatrix}$	$\begin{pmatrix} \nu_\tau \\ \tau \end{pmatrix}$	electromagnetic, weak
Quarks	$\begin{pmatrix} u \\ d \end{pmatrix}$	$\begin{pmatrix} c \\ s \end{pmatrix}$	$\begin{pmatrix} t \\ b \end{pmatrix}$	electromagnetic, weak, strong

Table 2.1: The fundamental particles grouped in three generations along with the forces in which they participate.

The electroweak theory describes the electromagnetic and the weak force, while Quantum Chromodynamics describes the strong force. The combination of them is called the Standard Model of Particle Physics (SM). Hence, it is the

force	vector boson	quantum number
electromagnetic	γ	charge (1)
weak	$W^{\pm}$, Z^0	weak isospin (2)
strong	8 gluons	colour (3)

Table 2.2: The exchange vector bosons and quantum numbers associated with the three fundamental forces described by the SM.

theory that describes the interplay of particles and forces at subatomic scale, not incorporating the gravitational force.

2.1.1 Electroweak Interaction

The joint description of the electromagnetic (described by Quantum Electrodynamics - QED) and the weak interaction has been achieved by the theory of electroweak interactions, which is implemented by an non-abelian gauge theory based on the group $SU(2)_L \otimes U(1)_Y$ [1]. The index L denotes that the charged weak boson fields are left-handed. The index Y corresponds to the leptonic hypercharge (Y) that is related to the weak isospin (T) and the electric charge through the analogous of Gell-Mann-Nishijima formula ($Q = T_3 + Y/2$). These quantum numbers are assigned to all fundamental fermions, and hence they all participate in electroweak interactions.

The left-handed lepton and quark fields

$$\psi_i^{\ell} = \begin{pmatrix} \nu_i \\ \ell_i \end{pmatrix}, \ \psi_i^{q} = \begin{pmatrix} u_i \\ d_i' \end{pmatrix} \tag{2.1}$$

of the i^{th} fermion family, transform as weak isospin doublets under $SU(2)_L$, while right-handed fermions are $SU(2)$ weak isospin singulets. The quarks in nature are superpositions of the single quark flavours. This quark flavour mixing can be described by the notation $d_i' \equiv \sum_j V_{ij} d_j$, where V is the Cabbibo-Kobayashi-Maskawa (CKM) mixing matrix.

The minimal model consists of three families and a single scalar Higgs field

$$\phi \equiv \begin{pmatrix} \phi^+ \\ \phi^- \end{pmatrix}, \tag{2.2}$$

that is added to the Lagrangian to generate the vector boson and fermion masses in a gauge invariant way via the Higgs mechanism.

At energies below the electroweak unification scale the symmetry is broken spontaneously. In this regime the electromagnetic force is mediated by exchange of massless photons (γ), while the weak interaction is mediated via heavy Z^0 and $W^{\pm}$ bosons, respectively.

2.1.2 Quantum Chromodynamics

It is an experimental observation that only quarks take part in strong interactions, leptons not. The strong interaction can be described by Quantum Chromodynamics (QCD), in which the mediating particles are massless gluons (g). It is a renormalisable non-abelian gauge theory based on the group $SU(3)_C$ of colour. The failure in observing free quarks up to now leads to the concept of confinement, which states that quarks and gluons are confined within colourless hadrons. In QCD, confinement can be qualitively explained by the behaviour of the strong coupling. At short distances the coupling is weak, i.e. the quarks are moving almost freely within the hadrons, while at large distances the coupling gets increasingly strong. If two quarks are moved apart the strong force becomes so strong that it is energetically better that a new pair of quarks is produced in a quantum fluctuation and several hadrons are produced. This process is called fragmentation or hadronisation and is an important ingredient to understand the internal structure of jets.

2.1.3 Limitations of the Standard Model

Within the last decades the SM has been tested at many high energy physics experiments all around the world with very high accuracy, without finding any evidence of inconsistency. Nevertheless, the most fundamental questions are left unexplained by the SM. The SM does not incorporate the gravitational force. But a theory which claims to be the fundamental theory of matter does have to cope with gravitation in a consistent way with Einstein's General Relativity, which has been successfully probed at a cosmological scale. Another open question is: Why are there three generations? - In the SM the three generations are introduced adhoc, without a stringent reason. And why do the fundamental fermions have the masses we observe? The Higgs mechanism only provides a tool to give the fermions masses, but does not give an explanation, why the particles have the measured masses. One of the major topics in present research is also the question, whether leptons can change their flavour, or not. In the SM, there is no a priori reason, why the lepton flavour number should be conserved. However, since in the quark sector a mixing of quarks of different generations has been observed, it is possible that such a mixing could also be present in the leptonic sector. No convincing evidence for lepton flavour violation has been reported so far. The recent observation of neutrino oscillation at experiments measuring atmospheric and solar neutrinos has provide some first hints that there might also be a mixture between the lepton generations [2]. Therefore it is worthwhile to look for lepton flavour violation at high energy collider experiments.

Hence, it is expected that the SM is only an approximation to a correct theory in terms of a more fundamental theory, describing (almost) everything in the physical world. In this context the HERA collider provides a unique opportunity to probe the SM and to search for new physics beyond the SM.

2.2 Lepton Nucleon Scattering

The most suitable way to probe the structure of matter are scattering experiments. They are in principle similar to the famous scattering experiment by Rutherford from the year 1909, where small projectiles, in this case alpha particles, are shot against an extended fixed target, in this case a thin gold foil. By colliding two particles a much higher center-of-mass (CM) energy can be achieved. Nowadays many scattering experiments are performed in colliding-mode, which allows a much deeper insight into the structure of matter. This section gives a general introduction to lepton proton scattering as realised by the HERA collider (see also section 4.1).

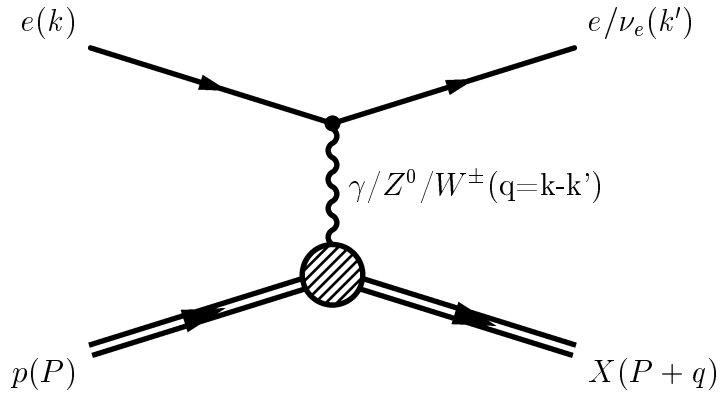

Figure 2.1: Diagram illustrating positron proton scattering. The four vectors of the particles are given in parentheses.

Deep Inelastic Scattering

In deep inelastic scattering (DIS) the electron (e) interacts with the proton (p) by virtual vector boson exchange as depicted in Fig. 2.1, where the lepton is represented by an electron (e) and X stands for the hadronic final state, in which the proton fragments after the interaction.

Assuming that k and k' are the four vectors of the initial and final lepton and P and $P+q$ are those of the incoming proton and the outgoing final state hadronic system X, where q is the four vector of the exchanged boson, the variables usually used to describe the kinematics of DIS are[1]:

$$\sqrt{s} = \sqrt{(k+P)^2}, \tag{2.3}$$

$$Q^2 = -q^2 = (k-k')^2, \tag{2.4}$$

$$x = \frac{Q^2}{2P \cdot q}, \tag{2.5}$$

$$y = \frac{q \cdot P}{k \cdot P}. \tag{2.6}$$

[1]Due to momentum conservation only three out of these four variables are independent.

Where $\sqrt{s}$ is the CM energy of the lepton-proton system. At the moment the HERA CM energy is $\sqrt{s} = 318$ GeV. Q^2 is the four momentum transfer square, equivalent to the negative square of the exchange boson mass. It determines the hardness of the collision. DIS processes correspond to processes, where Q^2 is much higher than 1 GeV^2 and where the invariant mass of the hadronic system is much larger than the proton mass. Processes with $Q^2 < 1$ GeV^2 usually lead to soft interactions. HERA covers a Q^2 region up to 40,000 GeV^2.

The dimensionless variable y can be interpreted as an inelasticity parameter of the interaction. In the proton rest system it measures the fraction of the energy from the electron transferred to the hadronic system, hence it is defined in the range $0 \leq y \leq 1$.

x is the dimensionless Bjorken scaling variable, which can be interpreted in the quark-parton model as the fraction of the proton momentum carried by the massless parton interacting with the lepton. Thus $0 \leq x \leq 1$. In the quark-parton model the proton is considered to consist of three quarks without the occurrence of gluon radiation. The Q^2-x-y coverage at HERA is depicted in Figure 2.2. Compared to the previous fixed-target experiments HERA has extended the coverage of x and Q^2 by about two orders of magnitudes.

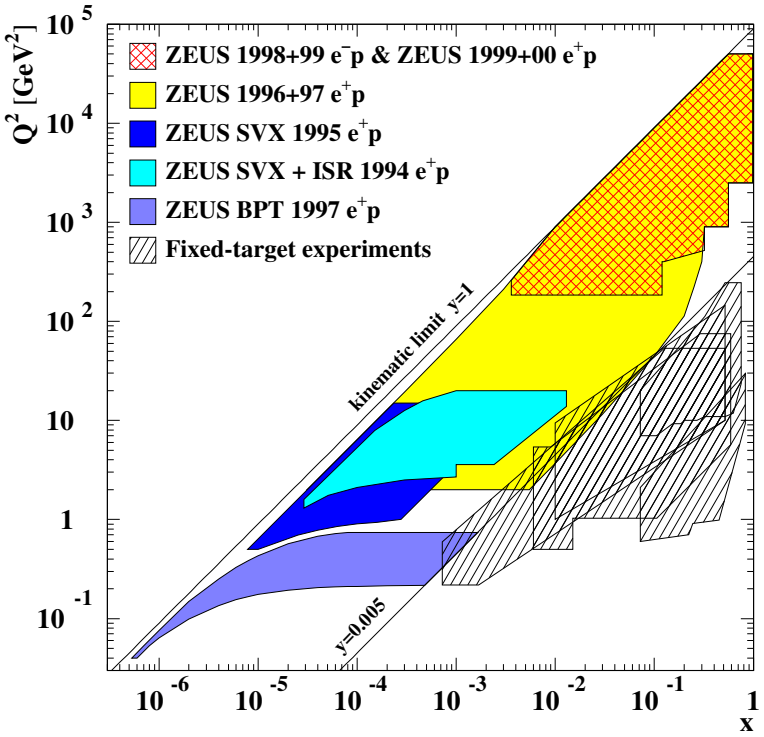

Figure 2.2: (Q^2, x) plane covered by HERA and fixed target experiments.

Processes in which the exchanged boson is a highly virtual photon or Z^0 boson are called neutral current DIS (NC DIS) processes. Those where the exchanged boson is a highly virtual $W^{\pm}$ boson are called charged current DIS (CC DIS) processes. Due to the $W^{\pm}$ boson exchange instead of an scattered electron an electron-neutrino is found in the final state.

If the momentum transfer is high enough the proton breaks up and fragments into a hadronic final state X with a much higher invariant mass than the proton mass. In the quark-parton model this process corresponds to an elastic scattering of the electron with a single massless quark carrying the fraction x of the proton momentum. The hardness or the resolving power of the interaction corresponds to the virtuality of the vector boson. As the boson virtuality increases, it probes smaller transverse distance scales and is able to resolve the structure of the proton.

Therefore one of the main interests in DIS processes is to test the interaction of quarks and gluons in the proton in the perturbative regime and to probe the proton structure down to the 10^{-16} cm scale.

Photoproduction

Photoproduction processes (γp) are characterised by the exchange of a quasi-real photon ($Q^2 \approx 0$) between the incoming electron and the hadronic system (an example Feynman graph is shown in Fig. 2.3b). Most of the interactions are soft. However, jets at high transverse energies can be produced by hard parton-parton interactions. They provide a good testing ground for perturbative QCD and can give insights into the structure of the photon.

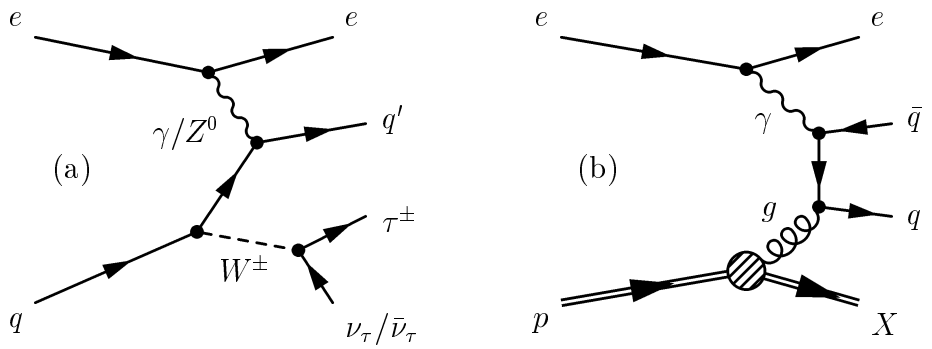

Figure 2.3: Examples of Feynman diagrams for (a) single $W^{\pm}$ production and (b) direct photoproduction.

Single $W^{\pm}$ Boson Production

The Feynman diagram for single $W^{\pm}$ boson production process with the highest contribution to the cross section in ep scattering is shown in Fig. 2.3a. In this diagram a $W^{\pm}$ boson has been radiated from a quark in the proton and this quark interacts with the photon. More details are given in section 3.1. The study of $W^{\pm}$ boson production events is worthwhile, since they have not been unambiguously observed at HERA and since they are a serious background to many analyses searching for rare events, which could indicate phenomena beyond the SM. The observation of muon events with large missing transverse momentum by the H1 collaboration and their possible interpretation in the framework of models beyond the SM is the topic of the next section.

2.3 Single $W^{\pm}$ Boson Production and Events with an isolated high-energy Lepton and Missing Transverse Momentum at HERA

Events with an isolated high energetic lepton and large missing transverse momentum at HERA seem to be powerful signatures to search for new phenomena beyond the SM, such as Supersymmetric Models [3] or dynamical models for fermion mass generation [4]. The ZEUS and the H1 Collaborations have reported in [5] and [6] the observation of such events. While some of those events can be explained by single $W^{\pm}$ boson production (in the following called 'W production') with a subsequent leptonic decay, three events with muons observed by H1 show properties atypical for W production (see Table 2.3).

In the analysis of ZEUS and H1 cuts were made to suppress non-$W^{\pm}$ events such that W production events are the only remaining SM background. The events are required to contain at least one isolated lepton (one electron or one muon) with a high transverse momentum P_T^{ℓ}, together with high missing momentum $\not{P}_T$. They may also contain a hadronic system X with a transverse momentum P_T^X. In Fig. 2.4 the distribution of the H1 events (94-97 data set) in the P_T^X-M_T^{ℓ} plane is shown. M_T^{ℓ} is the reconstructed transverse mass of the lepton system. In the muon channel no significant contribution from SM processes is expected at high P_T^X due to the event selection criteria. But five muon events with $P_T^X > 25$ GeV were found.

ZEUS published 94-97 e^+p (47.7 pb^{-1})	**Electrons and Muons obs./expected**
$P_T^X > 15$ GeV	$2/2.0 \pm 0.2$
$P_T^X > 25$ GeV	$0/1.7 \pm 0.2$
$P_T^X > 40$ GeV	$0/1.4 \pm 0.2$
H1 published 94-97 e^+p (36.5 pb^{-1})	**Muons obs./expected**
$P_T^X > 25$ GeV	$5/0.8 \pm 0.2$

Table 2.3: The published ZEUS and H1 analysis of the data from 1994-1997 correspond to an integrated luminosity of 47.7 pb^{-1} and 36.5 pb^{-1}, respectively. The applied cuts suppress non-$W^{\pm}$ background. The observed event rates at ZEUS are consistent with SM expectation, whereas an excess of muon events at $P_T^X > 25$ GeV in the data was observed by H1.

While the searches reported in [5] and [6] are based on the data from 1994 to 1997, preliminary results were presented in [7] using the data from 1994 to 2000 with an integrated luminosity of 130 pb^{-1} for the ZEUS and 82 pb^{-1} for the H1 collaborations, respectively. This is more than twice the luminosity for both searches than before. Again ZEUS did not observe a deviation from the SM (see Table 2.4). On the other hand H1 observed an excess at high P_T^X in both

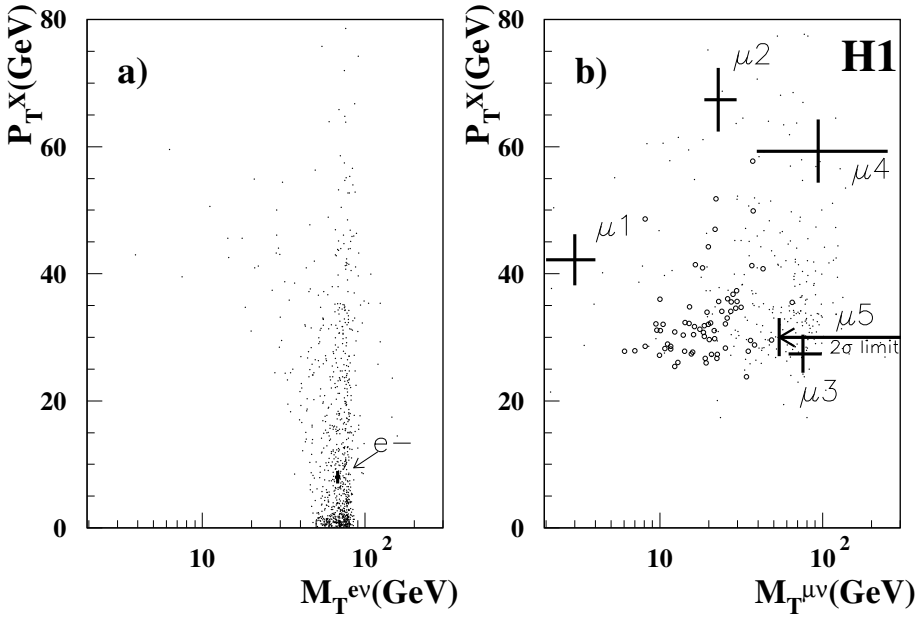

Figure 2.4: Distribution of the published H1 events (94-97 data set) in the P_T^X-M_T^ℓ plane (M_T^ℓ is the reconstructed transverse mass of the lepton system). (a) shows the electron channel and (b) the muon channel. The 1σ uncertainties on the measured kinematic parameters are indicated by the crosses (for event $\mu 5$ the 2σ limit for M_T^ℓ is shown). The dominant SM contributions (dots for W production, open circles for $\gamma\gamma$ processes in the muon channel) are shown for an accumulated luminosity which is a factor 500 higher than in the data (36.5 pb^{-1}). In the muon channel no significant contribution is expected at $P_T^X < 25$ GeV due to the event selection criteria.

ZEUS preliminary 94-00 $e^\pm$p (130 pb^{-1})	**Electrons obs./expected**	**Muons obs./expected**
$P_T^X > 25$ GeV	$1/1.14 \pm 0.06$	$1/1.29 \pm 0.16$
$P_T^X > 40$ GeV	$0/0.46 \pm 0.03$	$0/0.50 \pm 0.08$
H1 preliminary 94-00 e^+p (82 pb^{-1})	**Electrons obs./expected**	**Muons obs./expected**
$P_T^X > 25$ GeV	$3/1.05 \pm 0.27$	$6/1.21 \pm 0.32$
$P_T^X > 40$ GeV	$2/0.33 \pm 0.10$	$4/0.46 \pm 0.13$

Table 2.4: The preliminary ZEUS and H1 results of the analysis of the data from 1994-2000 corresponding to an integrated luminosity of 130 pb^{-1} and 82 pb^{-1}, respectively. The applied cuts suppress non-W background. The observed event rates at ZEUS are consistent with SM expectation, whereas an excess of events at high P_T^X in both 94-97 e^+p and 99-00 e^+p data were observed by H1.

1994-1997 e^+p and 1999-2000 e^+p runs (see Table 2.4). In the electron channel H1 observes three events for $P_T^X > 25$ GeV and two for $P_T^X > 40$ GeV, while 1.05 and 0.33 are expected, respectively. In the muon channel the excess is even more

outstanding. H1 observed six events for $P_T^X > 25$ GeV and four for $P_T^X > 40$ GeV, while 1.21 and 0.46 are expected. The probability to find ten or more events, if 1.7 are expected is $1.01 \cdot 10^{-5}$, according to Poisson statistics. Hence, a significant excess in the data has been found by H1.

2.4 Motivation for the Search for $W \to \tau\nu_\tau$

The excess of single lepton events observed by H1 to be explained within the SM has lead to many speculations on processes beyond the SM that could explain the observed events.

One promising hypothesis is the production of a *stop* quark ($e^+d \to \tilde{t}$) with R-parity violation in the framework of Supersymmetric Models [3]. Events of the observed topology could be due to a gauge decay $\tilde{t} \to W\tilde{b}$ via $\tilde{b} \to d\nu$. In the decay of the $\tilde{b}$ quark R-parity is again violated. This process would naturally produce events with a high P_T lepton of positive charge, a high P_T hadronic jet and significant missing P_T. The kinematics of the observed muon events is found to be compatible with a scenario with a *stop* mass of 200 GeV and a *sbottom* mass of 100 GeV.

Another hypothesis is the production of a single *top* quark via the lepton flavour violating processes $ep \to eXt \to eWb$ with subsequent decay $W \to \ell\nu$ [4]. The Feynman diagram of this process is shown in Figure 2.5. This process also would produce events with a high P_T lepton of positive charge, a high P_T hadronic jet and significant missing P_T.

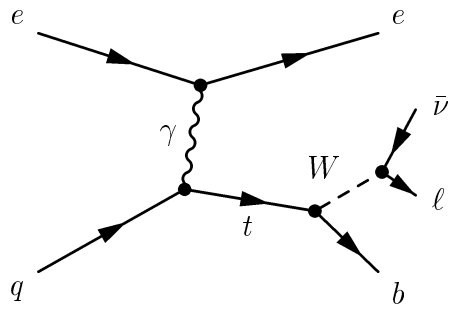

Figure 2.5: Example of a leading order Feynman diagram of single top production at HERA.

The origin of the high P_T^X lepton events and the answer to the question, why ZEUS cannot see these events, can only be clarified with much higher statistics. Since HERA has successfully completed a major luminosity upgrade in 2002, the prospects to accumulate an integrated luminosity of about 1 fb^{-1} are very good [8]. Additionally it is very interesting to investigate also the $W^\pm$ boson decaying into τ leptons. This is an obvious possibility to increase the statistics in the existing data. Furthermore from a physics point of view, particles of the third generation have a higher potential to couple to processes beyond the SM, since in general there are less constraints by existing data. This possibility would be

interesting, if the single leptons do not stem from a $W^{\pm}$ decay, but are produced directly by new interactions.

This analysis searches for SM single $W^{\pm}$ boson production events, where the $W^{\pm}$ boson decays into a τ lepton and a neutrino. Any deviation from SM predictions observed in this investigation could be a signature for new physics.

Chapter 3

Search Strategy

This analysis searches for SM single $W \to \tau\nu_\tau$ events, where the τ lepton decays hadronically, since the leptonic decays are already included in the analyses as mentioned in section 2.3. Additionally the identification of the decays $\tau \to e$ and $\tau \to \mu$ is even more difficult than the direct decays $W \to \mu\nu_\mu$ and $W \to e\nu_e$, since the transverse momentum of the electron and muons from these decays are usually lower. The hadronic decays have not yet been analysed, since additional backgrounds have to be controlled.

The most serious background are hard photoproduction, NC DIS, CC DIS, $\gamma\gamma \to \tau^+\tau^-$ and Z^0 boson production processes. In this chapter the general event topologies of these processes are discussed and the search strategy will be developed.

3.1 Single $W^\pm$ Boson Production with subsequent Decay $W \to \tau\nu_\tau$

The single $W^\pm$ boson production (W production) process $ep \to eWX$ is the most important source for $W^\pm$ bosons at HERA [9]. The Feynman diagrams for this process with the subsequent decay[1] are shown in Figure 3.1. Diagrams (a) and (b) describe the radiation of a W boson by the incoming and scattered quark, respectively. These diagrams, where a quasi-real photon and a massless quark are exchanged in a u-channel configuration, represent the processes with the highest contribution to the W production cross section. Diagram (c) contains the $WW\gamma$ triple-gauge-boson coupling. Since the cross section of W production is sensitive to the triple-gauge-boson vertex, the measurement of the cross section can provide limits on possible anomalous $WW\gamma$ coupling. In diagrams (f) and (g) the $W^\pm$ boson couples to the scattered neutrino and the incoming electron, respectively. While diagrams (a)-(c),(f) and (g) contain on-shell $W^\pm$ bosons (i.e the mass of the $W^\pm$ boson is $M_W = 80.4$ GeV), the diagrams (d) and (e) contain off-shell $W^\pm$'s in order to preserve electromagnetic gauge invariance.

The dominant contribution to the $ep \to eWX \to e\tau\nu_\tau X$ cross section arises

[1] The term '$W \to \tau\nu_\tau$' stands either for '$W^+ \to \tau^+\nu_\tau$' and '$W^- \to \tau^-\bar{\nu}_\tau$'.

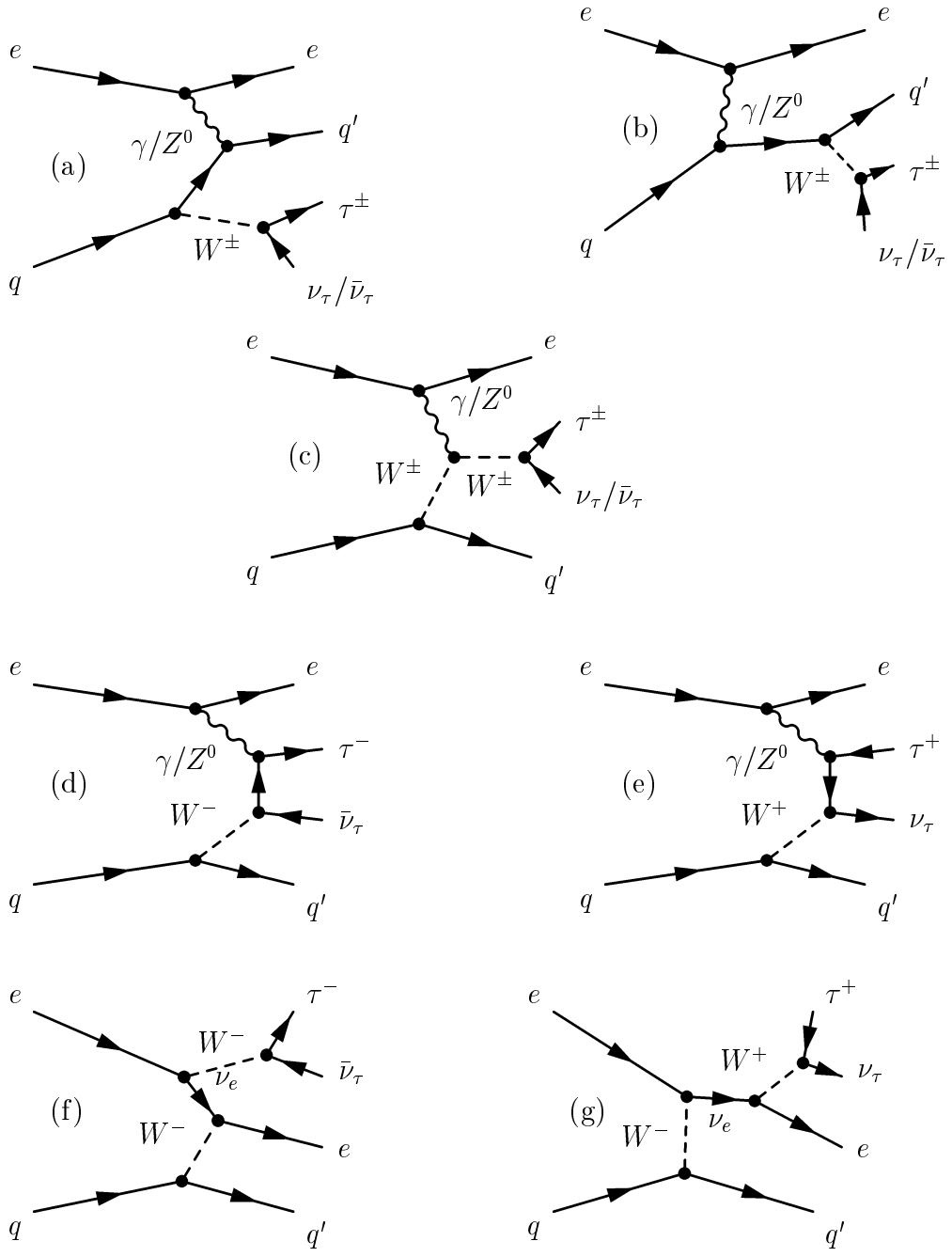

Figure 3.1: Feynman diagrams for the lowest order single $W^{\pm}$ boson production processes in electron quark scattering at HERA including the subsequent decay $W \to \tau\nu_\tau$. The diagrams for positron quark scattering can be constructed in an analogue way.

from the graph in Fig. 3.1a. The presence of the fermion u-channel poles in the calculation of this graph leads to a large logarithmic factor at small u, where the photon is almost on shell and can split into a massless quark-antiquark pair. In

this region the photon acts as a source of partons and one has to make use of the photon structure function to describe the complex structure of the photon. Therefore the phase space is splitted into two regions, the resolved photon region, where $|u| < u_{cut}$ and the deep inelastic (DIS) region, where $|u| > u_{cut}$:

$$\sigma = \sigma(|u| > u_{cut}) + \int^{u_{cut}} d|u| \frac{d\sigma}{d|u|}, \text{ where } \mathrm{u} = (\mathrm{p_q} - \mathrm{q_W})^2 \tag{3.1}$$

and p_q and q_W are the four momenta of the incoming quark and the final state W boson, respectively. The cross section calculation far away from the fermion u-channel pole ($|u| > u_{cut}$) does not require QCD corrections. For $|u| < u_{cut}$ the photon structure function approach has to be used to evaluate the cross section in the Weizsäcker-Williams approximation (WWA). The WWA gives an approximation of the photon flux radiated from the electron.

Using $u_{cut} < 25$ GeV^2 and assuming a branching ratio of 10.4% for the decay $W \to \tau\nu_\tau$ [10] the calculated total cross section is 0.12 ± 0.02 pb including W^+ and W^- boson production with the subsequent decay $W \to \tau\nu_\tau$. W^- boson and W^+ boson contribute in a similar way. The total cross section has been calculated for incoming electrons with energies of 27.5 GeV and proton energies of 920 GeV. The rates for e^+p collision differ by only a few per cents. The contribution from processes to the total cross section, where the photon is resolved is in the order of 25-30%. The highest uncertainties arise from the parametrisation of the quark densities in the photon and the choice of the virtuality of the probing photon.

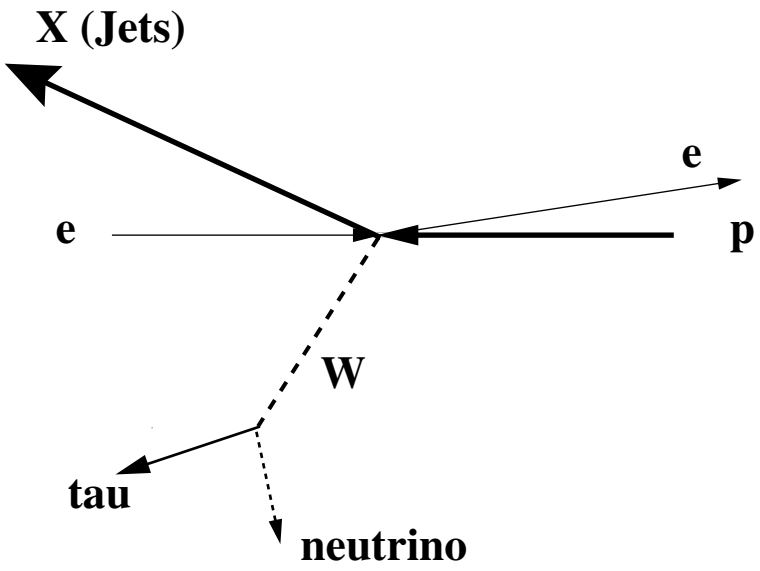

Figure 3.2: Sketch showing the expected topology of an $ep \to eXW \to eX\tau\nu_\tau$ event at HERA.

The expected event topology of the reaction $ep \to eXW \to eX\tau\nu_\tau$ contains the hadronic final state X, typically carrying small transverse momentum, and the τ lepton originating from the $W^\pm$ decay at not to small laboratory angles (typically 15°-120°). In the rest frame of the $W^\pm$ boson the τ lepton and the

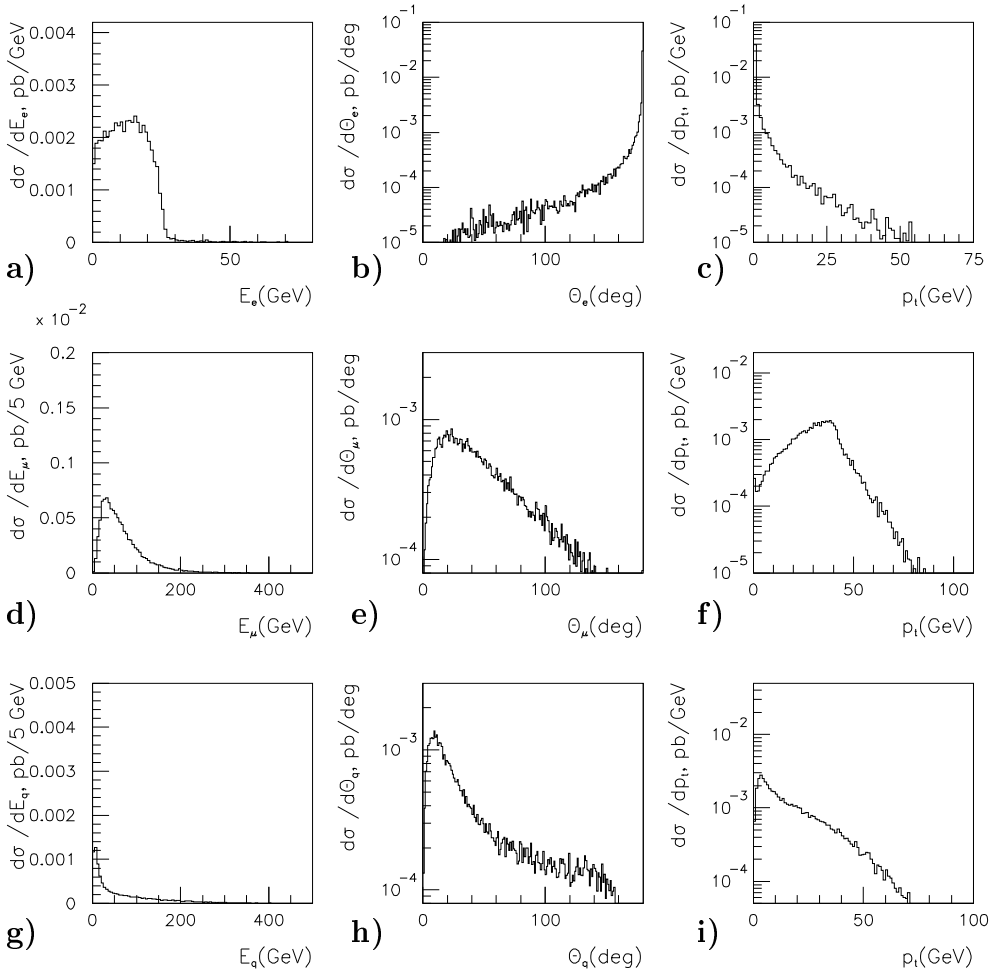

Figure 3.3: Variables characterising the topology of the process $e^-p \to e^-X\mu^+\nu_\mu$ as calculated by CompHEP [11]. Differential cross section distributions of the electron energy (a), scattering angle (b), transverse momentum (c), the muon energy (d), scattering angle (e), transverse momentum (f), the quark energy (g), scattering angle (h) and transverse momentum (i). The parametrisation of the calculations were similar to those made by EPVEC. The distributions for the process $e^-p \to e^-X\tau^+\nu_\tau$ are expected to be similar to the ones shown here.

neutrino ν decay back-to-back, leading to an expected high missing transverse momentum $\not{p}_T$ and a Jacobian peak around the $W^\pm$ mass in the spectrum of the lepton neutrino transverse mass $M_T^{\ell\nu}$. Since the virtuality of the photon is usually small, the incoming electron is mostly scattered at small angles with respect to the beam pipe and is expected to be observed in the central detector ($\theta < 164°$) in only less than 20%. Figure 3.3 [11] shows the distributions of some topology properties for the process $e^-p \to e^-X\mu^+\nu_\mu$, which is expected to be similar to those in the process $e^-p \to e^-X\tau^+\nu_\tau$. The calculations were performed by the Monte Carlo program ComHEP with the similar cuts applied by EPVEC [12], the Monte Carlo simulation program used in this analysis (see section 5.2). Shown are the calculated energy, polar angle and transverse momentum distribution of the scattered electron, the muon from the $W^\pm$ decay and the scattered quark.

To summarise, in $ep \to eXW \to eX\tau\nu_\tau$ events at least a single more or less isolated τ lepton along with large missing transverse momentum $\not{p}_T$ is expected. If the transverse momentum of the hadronic system p_T^X is high a second or even a third jet with large transverse momentum can be observed.

3.2 Background processes

The most serious background is expected to come from high cross section processes with hadronic particles in the final states, which produce hadronic jets[2] similar to jets induced by τ leptons, as well as processes with τ leptons in the final state. Hard photoproduction events are characterised by two or more jets. NC DIS events typically contain a hadronic jet, usually accompanied by an electron, which is back-to-back in the $\{r, \phi\}$-plane with respect to the jet. Also CC DIS events mostly contain one jet and can have large missing transverse momentum due to the scattered neutrino, which escapes undetected. The main processes where two τ leptons are produced are the two photon process $\gamma\gamma \to \tau^+\tau^-$ and $Z^0 \to \tau^+\tau^-$ characterised by a τ pair, where the τ leptons emerge back-to-back in the $\{r, \phi\}$-plane.

3.2.1 Photoproduction

Photoproduction processes (γp) are due to a quasi-real photon ($Q^2 \approx 0$) radiated from the incoming lepton and colliding with the incoming proton. The processes where hard jets are produced can be divided into two different subprocesses: The direct photoproduction process (Fig. 3.4a), in which the photon couples directly to a quark emitted from the proton, and the resolved photoproduction process (Fig. 3.4b), in which the photon acts as a source of partons. One of those partons, carrying only part of the total photon momentum, interacts with a parton in the proton.

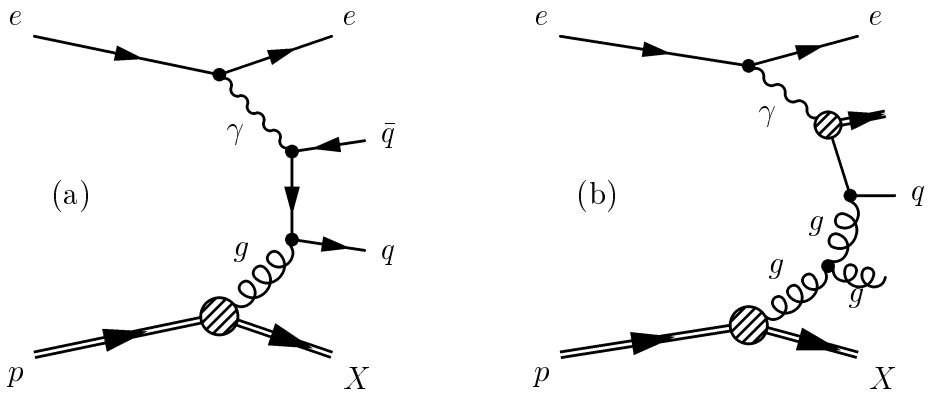

Figure 3.4: Examples for leading order Feynman diagrams for (a) direct and (b) resolved photoproduction processes.

[2]The definition of jets used in this analysis can be found in appendix A.

Due to the low virtuality of the photon, the electron in these reactions is scattered under a small angle, usually not detected by the central detector, since the electron generally does not carry large transverse momentum and usually no neutrino is produced in the final state. Photoproduction events typically contain two or more jets. In the case, where two jets are produced, they are mostly back-to-back.

The cross section of dijet photoproduction events at HERA has been measured by the ZEUS collaboration [13]. Figure 3.5 shows the differential dijet cross sections as a function of x_γ^{OBS} for three different Q^2 ranges. x_γ^{OBS} is the fractional momentum of the photon that takes part in the production of the dijet system. For $x_\gamma^{OBS} > 0.75$ the direct component dominates, while the $x_\gamma^{OBS} < 0.75$ region is sensitive mainly to the resolved component.

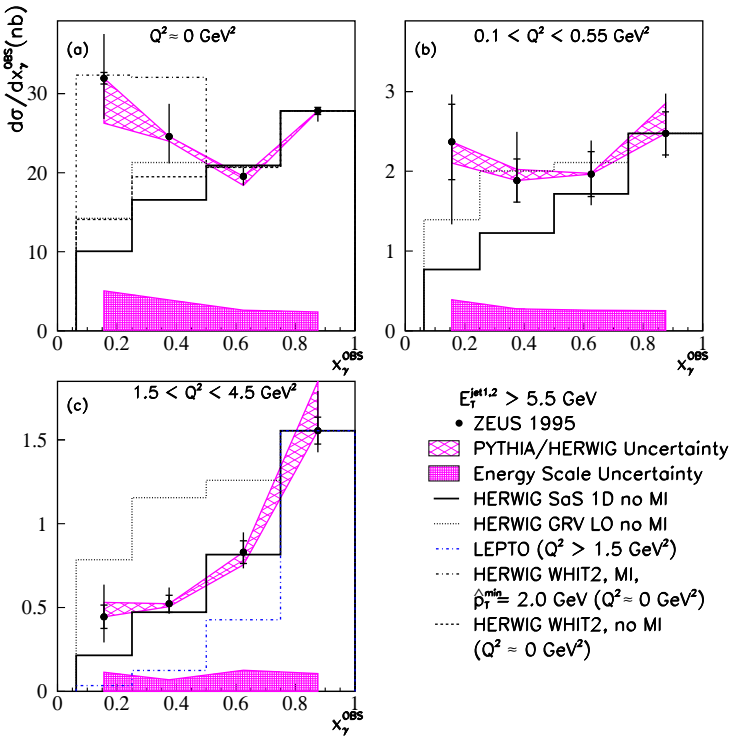

Figure 3.5: Dijet cross sections $d\sigma/dx_\gamma^{obs}$ for jets of hadrons selected with the k_T algorithm in the Q^2 ranges: (a) $Q^2 \approx 0$, (b) $0.1 < Q^2 < 0.55$ GeV^2, (c) $1.5 < Q^2 < 4.5$ GeV^2 for jets with $E_T^{jet} > 5.5$ GeV. The points represent the ZEUS data. The inner error represents the statistical error and the outer the the statistical and systematic errors added in quadrature. The shaded band represents the systematic error due to the uncertainty in modelling the jet fragmentation, estimated using PYTHIA. The shaded horizontal band represents the uncertainty due to the uncertainty in the calorimeter scale. A variety of theoretical curves, representing different models of the photon structure, are shown.

3.2.2 Neutral Current DIS

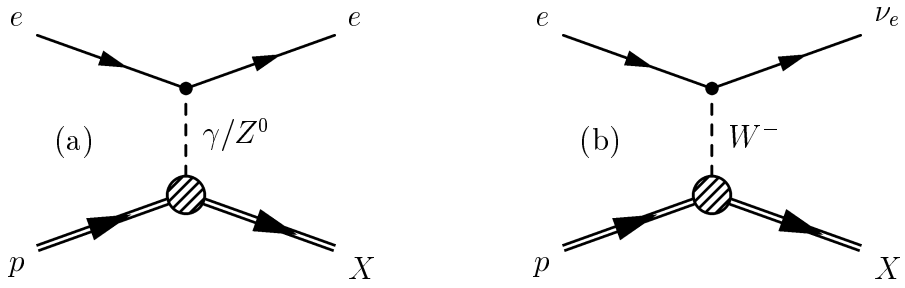

Figure 3.6: Feynman diagrams for (a) Neutral Current DIS and (b) Charged Current DIS.

In Neutral Current DIS processes (NC DIS) the incoming lepton interacts with the proton via photon or Z^0 boson exchange (Fig. 3.6a). The square of the momentum transfer Q^2 is typically a few GeV^2 and higher. In this reaction the electron is scattered at relatively high angles and can be measured by the central detectors. $\not{p}_T$ is expected to be small, since generally no neutrino is emitted and the transverse energy of the electron $p_T^e \sim Q^2(1-y)$ is compensated by the hadronic final state.

The differential cross section for NC DIS at HERA as function of Q^2 measured by the ZEUS collaboration [14] is shown in Figure 3.7.

3.2.3 Charged Current DIS

In Charged Current DIS processes (CC DIS) the exchanged vector boson is a virtual $W^{\pm}$ boson. These processes are characterised by a high Q^2, typically one hadronic jet and a high $\not{p}_T$ corresponding to the escaping neutrino (Fig. 3.6b), which can not be detected by any component of the ZEUS detector. The single differential cross section for CC DIS at HERA as function of Q^2 measured by the ZEUS collaboration [15] is depicted in Figure 3.7.

3.2.4 Lepton Pair Production

In the lepton pair production process $ep \to \gamma\gamma \to l\bar{l}$ a lepton anti-lepton pair is produced in a photon-photon collision. The case where the final state is a τ pair (Fig. 3.8b) can be a serious background. The τ leptons are produced with back-to-back-topology.

The cross section for $\gamma\gamma \to \tau^+\tau^-$ in the HERA kinematic region is estimated to be about 0.5-5.2 pb for deep inelastic scattering, 0.1-3.6 pb for quasi-elastic scattering and about 6.3 pb for elastic scattering processes, leading to total cross section of $\sigma = 17.7$ pb. The cross section ranges in deep inelastic scattering and quasi-elastic scattering processes come from the calculations for different quark flavours which interacts with the electron (see also section 5.2).

The phase space for lepton pair production can be divided into three regions, defined by the momentum transfer squared Q^2 and the invariant mass M^{had} of

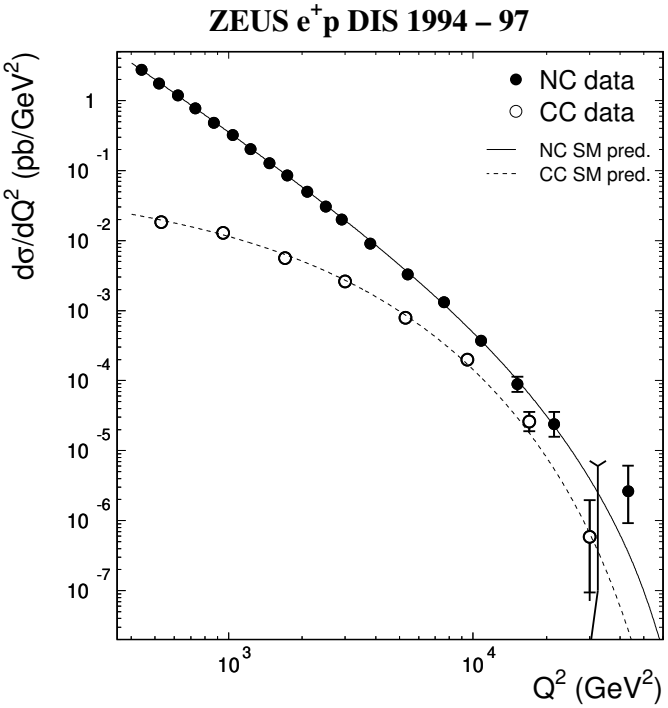

Figure 3.7: The single differential cross section for NC and CC DIS as function of Q^2 obtained by the ZEUS collaboration from the 1994-1997 e^+p data. The solid and the dashed lines correspond to NC DIS SM and CC DIS SM predictions, respectively.

the produced hadronic final state. In the elastic region, the hadronic final state X consists only of the scattered proton, which stays intact in the scattering process, i.e. $M_X = m_p$. In the quasi-elastic region the proton does not stay intact during the scattering process, but is transformed into an excited nucleon state, which decays into a nucleon and mostly pions, i.e. $M_X > m_p$. In the inelastic region the proton breaks off and many hadrons are produced, i.e. $M_X >> m_p$. In this region the momentum transfer between the incoming proton and the final state hadronic system is large, usually more than a few GeV^2.

3.2.5 Z^0 Boson Production

Fig. 3.8b shows an example for Z^0 boson production with the subsequent τ pair decay of the Z^0 boson. This decay has two τ leptons in the final state, where the τ leptons are produced back-to-back. This process is not expected to be serious background, since the cross section is very small:

The calculated cross section for Z^0 production with the subsequent decay $Z^0 \rightarrow \tau^+\tau^-$ is 13.0 ± 1.7 fb (for details see Ref. [9]), assuming a branching ratio of 3.4% for the decay $Z^0 \rightarrow \tau^+\tau^-$ [10]. Hence, the cross section is so small that the contribution of this process to the background can be neglected in this analysis. Nevertheless, it would be interesting to look for these events.

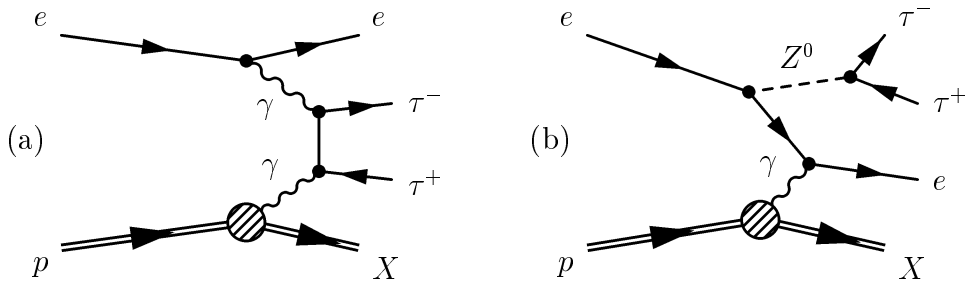

Figure 3.8: Feynman diagrams for the (a) $\gamma\gamma$ process including τ pair production and (b) an example for Z^0 production with a τ pair in the final state.

3.3 Search Strategy

As a summary of the event topology discussion of the signal and background processes in this chapter an outline of the search strategy is given now. The set of selected topology properties of SM single $W \to \tau\nu_\tau$ events, where the τ lepton decays hadronically should be distinct from each of the background processes. Therefore the background has to be rejected without losing too many of the signal events. In the first step this analysis aims to select CC DIS without rejecting $W^\pm$ boson production events in the data and aims to remove all other background events. These cuts are presented in section 8.2. For the remaining events the selected events are required to contain

- a single τ lepton with a large transverse momentun p_T^ℓ, which may be isolated (probably at high laboraty angles),
- large missing transverse momentum $\not{p}_T$,
- a transverse mass of the lepton neutrino system $M_T^{\ell\nu}$ not too far from the $W^\pm$ boson mass $M_W = 80.4$ GeV,
- a hadronic system with low transverse momentum p_T^{had}, typically in the forward region, if any.

The identification of hadronically decaying τ lepton is the major task of this analysis. For this purpose a multivariate discrimination technique is used, it will be introduced in chapter 6 and the identification of τ leptons will be described in chapter 7.

Chapter 4

HERA and the ZEUS Detector

This chapter gives an outline of the HERA storage ring and the ZEUS detector with its trigger sytem and the data acquisition scheme. Only the detector components most important for this analysis will be discussed in more detail. For further and more detailed informations on the ZEUS detector see refs. [16, 17].

4.1 The HERA Collider

HERA (Hadron Elektron Ring Anlage) is the world wide first lepton-proton collider which has been providing luminosity to the experiments ZEUS and H1 since 1992. Fig. 4.1 gives a schematic overview of the accelerator elements. The HERA accelerator has a circumference of about 6.3 km and consists of two separated storage rings, one for electrons (positrons) and one for protons. While the normal-conducting electron (positron) ring operates at room temperature the proton ring is super-conducting and operates at 4.4 K. At two points along the circumference the two beam pipes merge into one in order to provide electron-proton (ep) collisions for the experiments ZEUS and H1. The two other experiments which are located at HERA, HERMES and HERA-B, operate in the fixed-target mode, using the electron beam and the proton beam, respectively.

Year	E_e [GeV]	E_p [GeV]	delivered $\mathcal{L}$ [pb^{-1}]	physics $\mathcal{L}$ [pb^{-1}]
93-94 e^-p	26.7/27.5 (94)	820	2.17	0.82
94-97 e^+p	27.5	820	70.92	48.3
98-99 e^-p	27.5	920	25.2	16.71
99-00 e^+p	27.5	920	94.95	66.3

Table 4.1: Summary of the luminosities and the beam energies for the different running periods.

HERA initially began as an electron-proton collider with a proton energy of 820 GeV and an electron energy of 26.7 GeV. The integrated luminosity achieved in 1993 was 1.09 pb^{-1}. Since that time HERA has been undergoing several upgrade schemes. In table 4.1 the type of the interaction, the proton energy, the

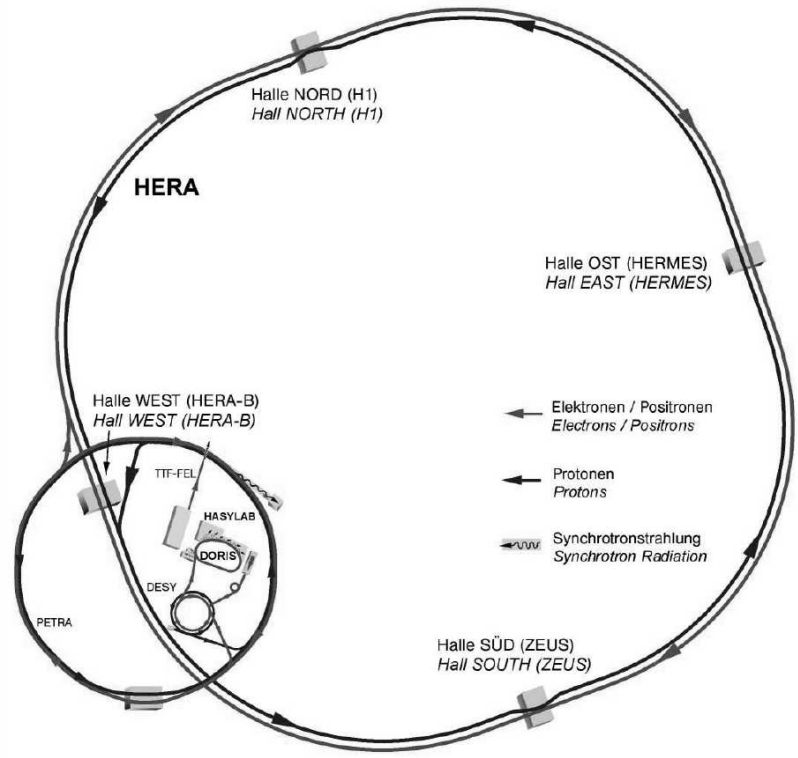

Figure 4.1: Schematic overview of HERA along with the locations of the four experiments.

electron energy, the delivered luminosity and the luminosity useful for physics analysis for the different running periods are listed.

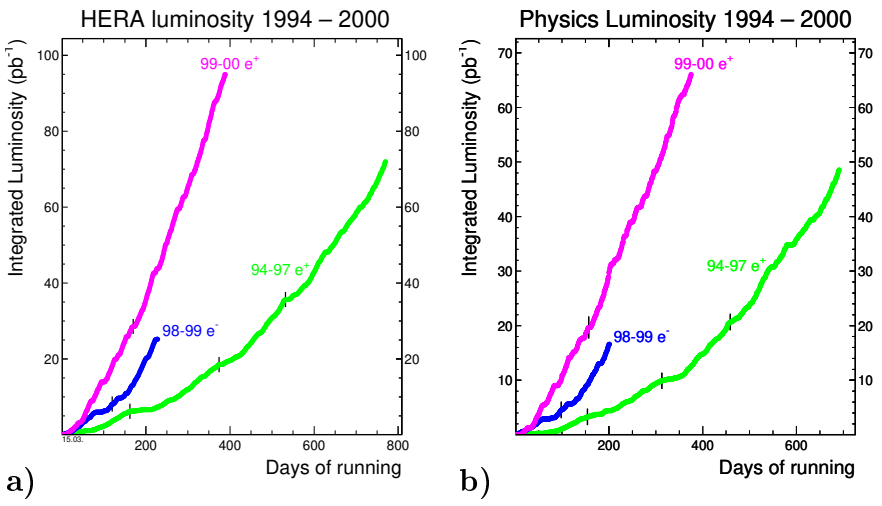

Figure 4.2: (a) Integrated luminosity delivered by HERA and (b) integrated physics luminosity vs. the days of running for the periods from 1994 to 2000.

An illustration of the delivered and the physics luminosity as a function of the days of data taking from 1994 to 2000 is shown in Fig. 4.2. The maximum instantaneous luminosity achieved so far is $\mathcal{L} = 2 \cdot 10^{31}$ cm^{-2} s^{-1} (2000) with 174 colliding bunches. After the upgrade in the year 2000 an increase of the luminosity by a factor of about four ($\mathcal{L} = 7.4 \cdot 10^{31} cm^{-2} s^{-1}$) is expected [8, 17].

4.2 The ZEUS Detector

The ZEUS detector system [16] consists of many components and was designed as a multi-purpose magnetic detector with nearly hermetic coverage.

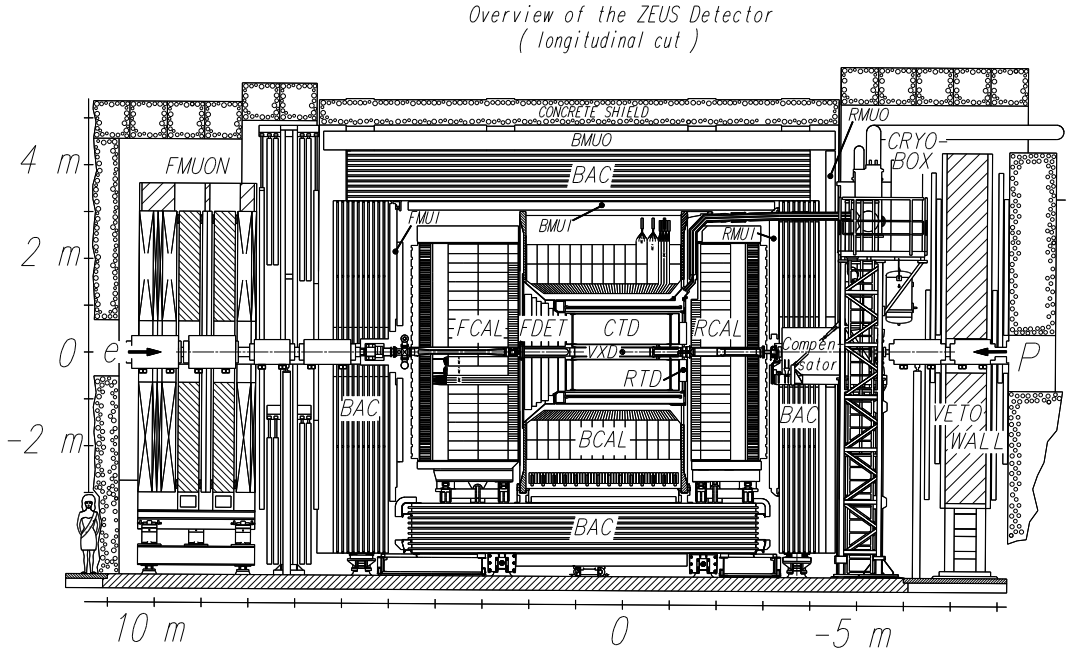

Figure 4.3: Cross sectional view of the ZEUS detector along the beam pipe.

Until 1995 the vertex detector (VXD) was the detector nearest to the beam pipe, but it was removed during the 1995/1996 shutdown period. In 2001, a silicon strip micro vertex detector (MVD) has been installed and is now the innermost component of the ZEUS detector system. A drift chamber acts as the central tracking detector (CTD), complemented by the forward detector (FDET) and the rear tracking detector (RTD). For charge and momentum determination the tracking system is surrounded by a super-conductiong solenoid providing a magnetic field up to 1.8 T. The uranium calorimeter system is divided into a barrel part (BCAL), a forward part (FCAL) and a rear part (RCAL), which provides a nearly hermetic coverage. It is surrounded by a backing calorimeter (BAC), which measures late showering particles and additionally operates as magnetic yoke. The muon detector system consists of the parts located inside (FMUI, BMUI, RMUI) and outside (FMUON, BMUO, RMUON) the magnetic yoke.

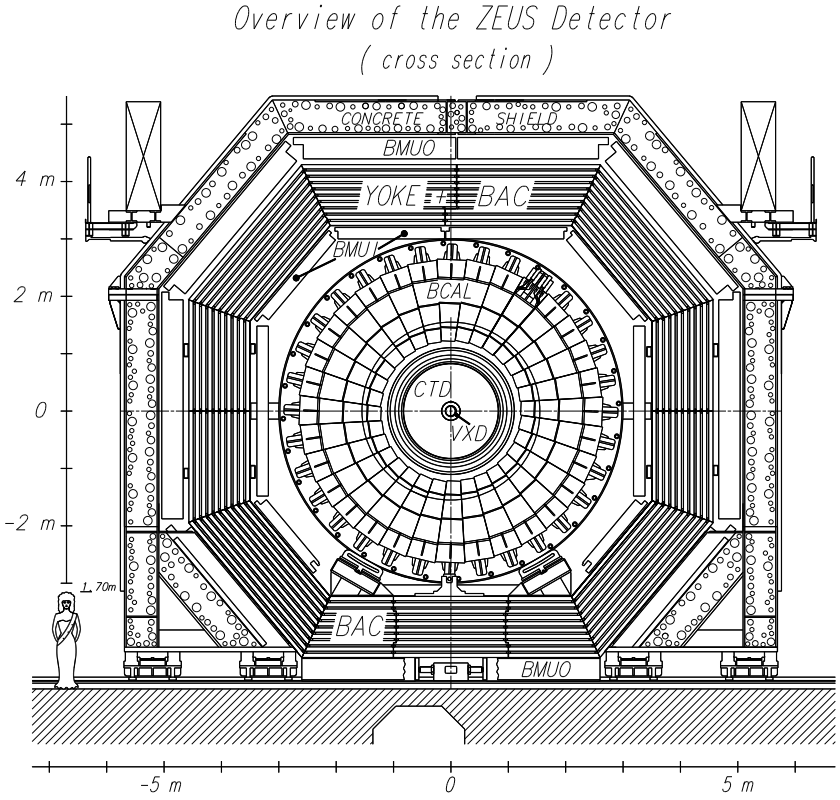

Figure 4.4: Cross sectional view of the ZEUS detector perpendicular to the beam pipe.

Figures 4.3 and 4.4 give a cross sectional view of the ZEUS detector along the beam pipe (r-z-view) and perpendicular to the beam pipe (x-y-view), respectively.

The reference coordinate system of the ZEUS detector is a cartesian system with the origin at the nominal interacting point. The z-axis is pointing into the direction of the proton beam, while the y-axis is pointing to the centre of HERA and the y-axis to the sky.

4.2.1 The Central Tracking Detector

The CTD is a cylindrical wire chamber with nine superlayers, each consisting of eight sense wire layers. Figure 4.5 shows a cross sectional view of a CTD segment.

The chamber has an outer radius of 85 cm and an overall length of 241 cm, while the active dimensions are 18.2-79.4 cm and 205 cm, respectively. The polar angle coverage is $15^\circ < \theta < 165^\circ$ (for a measured track it is required to pass through at least two superlayers). The overall number of sense wires is 4608 arranged in 576 cells. The drift chamber is filled with a gas mixture of argon, carbon dioxide and ethane bubbled through ethanol at atmospheric pressure. The gas will be ionized by traversing charged particles along their trajectories. The produced electrons and ions will drift to different charged wires. In the field of

the sense wire they produce new electron-ion-pairs, which leads to an avalanche effect and a multiplication of the signal of typically 10^4-10^5.

The wires are oriented at an angle of 45° to the radial direction to compensate the Lorentz angle of 45°, resulting from the combined electric and magnetic field. This ensures an optimal drift path and reduces the drift time (max. drift time $\sim$ 500 ns).

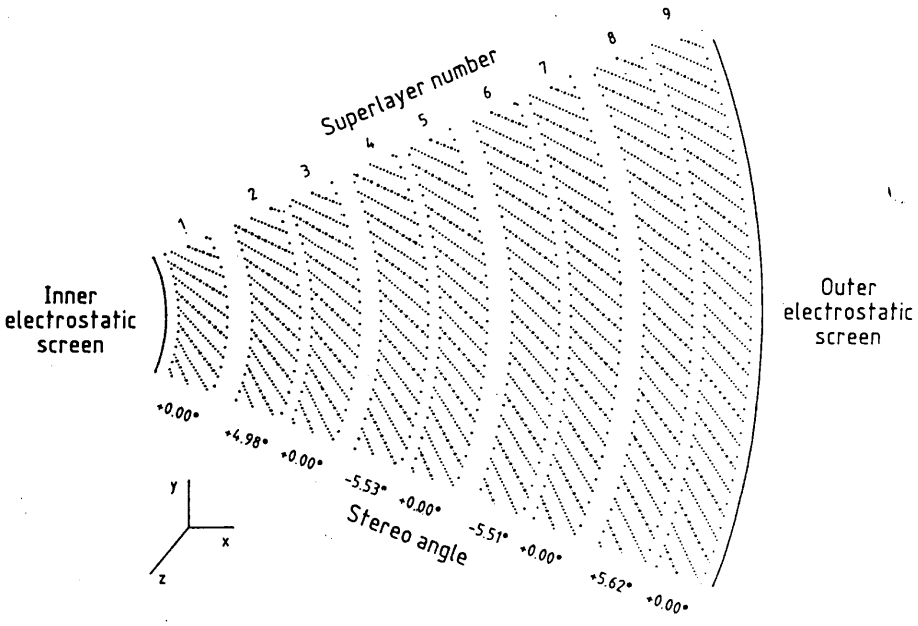

Figure 4.5: Segment of the CTD in cross sectional view: The nine superlayers with their different stereo angles.

From the innermost to the outermost the superlayers are numbered from one to nine. The wires of the five odd numbered superlayers lie in direction of the chamber axis, while those of the four even numbered superlayers are tilted by stereo angles of about $\pm 5°$ with respect to the beam line. This arrangement leads to a position resolution of about $\sigma_{\{r,\phi\}} = 200\ \mu$m ($\theta$-dependent) in the $\{r, \phi\}$-plane and a z-coordinate resolution of $\sigma_z = 2$ mm. Three superlayers are equipped to provide z-by-timing measurements. With this method the z-position is obtained by measuring the difference of the running times of the signal at the two opposite ends of a wire. Since this method is much faster than the stereo method it is used for trigger purposes, although with a lower resolution of about $\sigma_z = 4$ cm. The primary vertex can be calculated by extrapolating the reconstructed tracks to the beam axis. The typical resolution is 0.4 cm in z direction and 0.1 cm in transverse direction, respectively.

The strong magnetic field of 1.43 T provided by the superconducting solenoid ensures a high transverse momentum (p_T) resolution of

$$\frac{\sigma(p_T)}{p_T} = 0.0058 \cdot p_T[GeV] \oplus 0.0065 \oplus 0.0014/p_T\ [GeV] \qquad (4.1)$$

at $\theta = 90°$, where the first term corresponds to the hit position resolution, the second to the multiple scattering within and the third before the CTD.

4.2.2 The Calorimeter

The ZEUS detector is a uranium-scintillator sampling calorimeter with a high resolution, especially for hadronic energies. It consists of three parts: The forward calorimeter (FCAL), the barrel calorimeter (BCAL) and the rear calorimeter (RCAL). The FCAL and the BCAL are divided into three layers - an electromagnetic segment (EMC) and two hadronic segments (HAC1, HAC2) - while the RCAL consists of one EMC and one HAC1. Each part consists of modules, towers and cells as can be seen in Fig. 4.6 and Fig. 4.7. The overall number of cells is 5918 with dimensions in the range from 5x20 cm^2 to 24x35 cm^2.

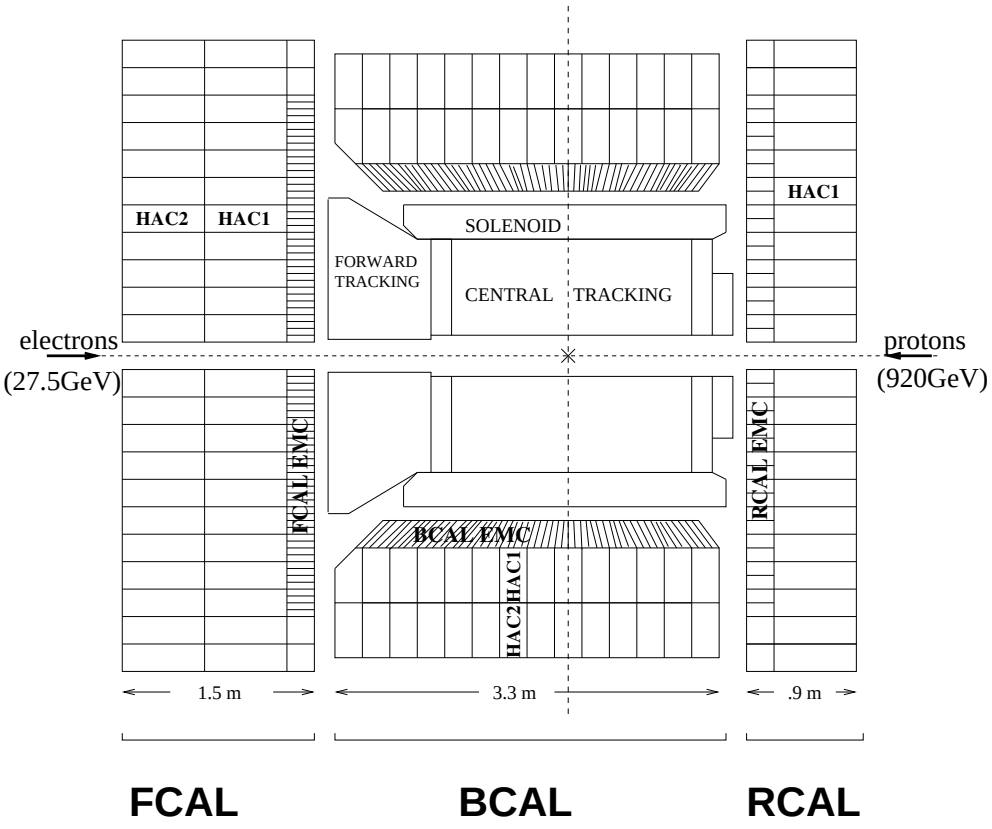

Figure 4.6: The different parts of the ZEUS calorimeter (cross section).

The ZEUS calorimeter is compensating, which means that the response to electrons and hadrons with the same energy is nearly equal. The maximal depths of the HAC1 (HAC2) for the FCAL, the BCAL and the RCAL are 7.14λ, 4.92λ and 3.99λ, respectively, while the ones of the EMC are $25.9X_0$, $22.7X_0$ and $25.9X_0$, where λ is the hadronic absorption length and X_0 is the electromagnetic radiation length. The arrangement of the different calorimeter parts ensures a nearly her-

metic coverage. The angular range for the polar angle, covered by the calorimeter system is $2.2° < \theta < 177.5°$ (see Fig. 4.6).

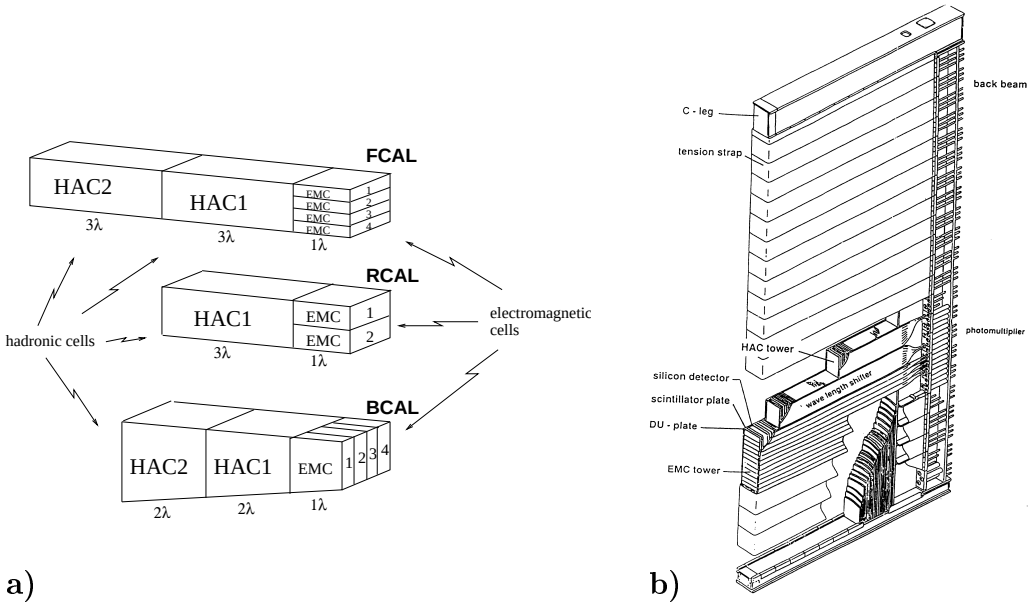

Figure 4.7: (a) Towers from the different calorimeter parts and (b) a module from the FCAL.

As active material 2.6 mm thick organic scintillators are used. When a high energetic particle crosses a scintillator plate it can interact with the atoms and lift an electron to a higher energetic state. This electron will return after a characteristic time to its initial state by emitting light with a characteristic frequency spectrum. The light generated in the scintillator is collected on both sides of a module by wavelenght shifters and is guided to the photomultiplier tubes, which converts it into an electronic signal.

The energy resolution of the calorimeter for electromagnetic showers, measured under test beam conditions is

$$\frac{\sigma(E)}{E} = \frac{18\%}{\sqrt{E\ [GeV]}} \oplus 1\% \tag{4.2}$$

and

$$\frac{\sigma(E)}{E} = \frac{35\%}{\sqrt{E\ [GeV]}} \oplus 2\% \tag{4.3}$$

for hadronic showers.

4.2.3 Luminosity Monitor

The luminosity at ZEUS is measured via the bremsstrahlung process $ep \to e\gamma p$. The cross section for this reaction is very high ($\sigma_{brems} \approx \mathcal{O}(20\text{ mb})$), providing

a fast and continous monitoring of the event rate. The luminosity is determined by measuring the rate of the detected photons in the photon calorimeter, it is defined as:

$$\mathcal{L} = \frac{\dot{N}_{brems}}{\sigma_{brems}}, \tag{4.4}$$

where $\dot{N}_{brems}$ is photon rate and σ_{brems} is the cross section, corrected for detector acceptance.

After the photons exit the beam pipe at small angles $\theta < 0.6$ mrad, they hit the γ detector, located at z= -107 m from the nominal interaction point and shielded by a carbon-lead filter to absorb synchroton radiation. The acceptance of the lead-scintillator photon calorimeter is about 98% and the effective resolution is $23\%/\sqrt{E[GeV]}$. Since photon rates are very high, the statistical uncertaintities are small. The systematic uncertainty is mainly due to the bremsstrahlung of the electrons on the residual gas molecules. The overall sytematic uncertainty is in the order of about 1.6%.

4.2.4 Trigger System and Data Acquisition

The task of the ZEUS trigger system is to select the interesting events amongst the many background events. The bunch crossing frequency of 10.4 MHz (96 ns between two bunch crossings) and the high rate of uninteresting events is a challenge for the trigger system. This leads to the requirement of fast processors and algorithms.

The total event rate is dominated by proton beam gas interactions ($\sim$ 10 kHz), proton beam halo events ($\sim$ 10 kHz) and cosmic muons traversing the detector ($\sim$ 1 kHz). In comparison the physics DIS event rate is several orders of magnitudes smaller. E.g. for neutral current deep inelastic scattering (NC DIS) events ($Q^2 > 100$ GeV^2) the event rate is about 0.1 Hz and for charged current DIS (CC DIS) the event rate is in the order of 1 mHz. The given rates correspond to an intantaneous luminosity of $2 \cdot 10^{31}$ cm^{-2} s^{-1}. The ZEUS trigger system has three levels.

The first level trigger (FLT), which is based on logical circuits, is designed to have an output rate of 1 kHz. The decision time is limited to 4.4 μs after one bunch crossing, which corresponds to 46 bunch crossings between two decisions. To avoid deadtime the data of the detector components and the electronics are buffered to the pipeline, where they are processed with a rate of 10.4 MHz. Each detector component has its own trigger logic, based on fast computable global variables like energy sums and timing information. All individual decisions are stored in the global first level trigger (GFLT) and the accepted events are passed to the second level trigger (SLT).

The SLT is based on a network of programmable transputers. The data can be calculated more precisely and correlations of the informations between the different components are taken into account more accurately, such as track momenta, vertex position, electron and jet finding. The decisions are made after

a time of 10 ms and are stored in the global second level trigger. This requires a pipeline buffering in the component readout systems. The data is reduced by a factor of 10 and is sent to the eventbuilder (EVB), where it is accessible to the third level trigger (TLT).

The TLT runs on a powerful processor farm. It has to cope with an event rate of about 100 Hz and reduces it to $\sim$ 5 Hz. The TLT makes a complete reconstruction of the event variables (tracking, muon, electron and jet finding etc.), using algorithms which are similar to that used in the offline code.

The fully reconstructed events are stored at the DESY computing centre, always accessible for further analysis purposes. During this process a pseudo fourth level trigger is introduced by assigning DST (data summary tapes) bits, which indicate whether an event fulfill a set of requirements or not. This mechanism ensures a fast access to a given class of events.

Chapter 5

Monte Carlo Simulation

Monte Carlo (MC) simulations (an overview of MC generators at HERA can be found in [18]) are indispensible for this analysis. All cuts and algorithms developed to discriminate signal from background are deduced from the study of MC simulations. They can also indicate in which regions certain observables are measured accurately and can be used to understand the effect of the limited detector acceptance and resolution.

5.1 Event Generators and Detector Simulation

MC simulations usually consists of two parts: The event generation and the detector simulation.

The event generator simulates certain processes in ep collisions and generates the four-vectors of all particles in the final state. In the detector simulation the emerging particles interacting with the components of the detector are simulated, including the trigger response. The ZEUS detector simulation program MOZART is based on the GEANT [19] package performing detailed simulation of the geometry and the materials of the detector and calibrated with measurements from test beams.

The Monte Carlo simulations are often the only practical way to evaluate difficult integrals or sample complex probability densities, e.g. occurring within theories and models of high energy physics. The Monte Carlo techniques are based on a reliable random number generator, which generates uniform statistically independent values.

5.2 Monte Carlo Samples

In Table 5.1 all simulated processes are listed, along with the name of the used Monte Carlo generators, the applied kinematic cuts and the corresponding cross sections, integrated luminosities and number of events.

Single $W^{\pm}$ Boson Production

The Monte Carlo generator program EPVEC [12] was used to generate the $W^{\pm}$ boson production events and to compute the contributions of the different Feynman diagrams (see section 3.1) to the total cross section. To increase the number of events the generator was modified in such a manner that the produced $W^{\pm}$ boson was forced to decay into a τ lepton and a neutrino only, all other leptonic and hadronic channels were suppressed. EPVEC is a leading order program and includes no QCD radiation. The hadronisation of the final state is based on JETSET [20].

The phase space for the diagram 3.1a can be divided into two regions, defined by $u = (p_q - q_W)^2$, where p_q and q_W are the four momenta of the incoming quark and the final state $W^{\pm}$ boson, respectively. In the resolved photon region, where u is small, the photon is almost on shell and can fluctuate into a massless quark anti-quark pair. While in the deep inelastic region (DIS) u is comparatively large and the photon highly virtual (for more details see section 3.1 or Ref. [9]).

Photoproduction

The HERWIG [21] Monte Carlo program was used to simulate both, direct and resolved photoproduction events. It is utilised for the simulation of the hard scattering based on the leading order matrix element $\mathcal{O}(\alpha_s)$ and uses the parton shower approach for initial and final state QCD radiation. The transition from partons to hadrons is performed with the cluster fragmentation model. Note that the total number of used MC events corresponds to an integrated luminosity of only 5.59 pb^{-1}. This is less than ten per cent of the integrated luminosity of the data sample (65.5 pb^{-1}) used for the data analysis (see chapter 8).

NC and CC DIS

Simulations of high-Q^2 charged and neutral current DIS were performed, using the event generator DJANGO, an interface to the Monte Carlo programs HERACLES [22] and LEPTO [23]. HERACLES simulates electroweak radiative effects from the electron and the quark. The package LEPTO as well as the colour-dipole model based ARIADNE [24] were used to simulate higher order corrections for QCD, via parton cascades. The first order in α_s is based on the $\mathcal{O}(\alpha_s)$ matrix element. The hadronisation of the partonic final state was performed by JETSET.

τ pair production

The cross section estimations were obtained from a simulation of di-lepton events using the Monte Carlo simulation programme GRAPE-Dilepton [25] with the requirement of at least one τ lepton with transverse momentum greater than 5 GeV in the polar angle range of $5^\circ < \theta < 175^\circ$. The cross section calculation of GRAPE-Dilepton is based on the exact matrix elements, where all the electroweak diagrams at tree level are included except for quark-Z^0 couplings and lepton pair

production through photon radiation from the photon. It is interfaced to JETSET to simulate the hadronisation of the partonic final states. For the cross section calculations the τ pair production process is divided into seven subprocesses: Deep inelastic scattering of e and u quark (DIS1), deep inelastic scattering of e and $\bar{u}$ quark (DIS2), deep inelastic scattering of e and d/s quarks (DIS3), deep inelastic scattering of e and $\bar{d}/\bar{s}$ quarks (DIS4), quasi elastic scattering with hadronic mass > 5 GeV (QELA1), quasi elastic scattering with $1.08 <$ hadronic mass < 5 GeV (QELA2) and elastic scattering (ELA).

Process	**Generator**	**kin. Cuts**	σ **[pb]**	$\mathcal{L}$ **[pb^{-1}]**	**#Events**
$W^- \to \tau^-(DIS)$	EPVEC	$u_{cut} > 25$ GeV^2	$8.68 \cdot 10^{-2}$	$7.12 \cdot 10^5$	62k
$W^- \to \tau^-(res.)$	EPVEC	$u_{cut} > 25$ GeV^2	$2.28 \cdot 10^{-2}$	$2.18 \cdot 10^6$	50k
$W^+ \to \tau^+(DIS)$	EPVEC	$u_{cut} > 25$ GeV^2	$1.04 \cdot 10^{-1}$	$3.52 \cdot 10^5$	37k
$W^+ \to \tau^+(res.)$	EPVEC	$u_{cut} > 25$ GeV^2	$1.88 \cdot 10^{-2}$	$3.45 \cdot 10^6$	65k
Direct Photoproduction	HERWIG 5.9	$Q^2 < 4$ GeV^2, $E_T > 10$ GeV	$6.55 \cdot 10^4$	4.58	300k
Resolved Photoproduction	HERWIG 5.9	$Q^2 < 4$ GeV^2, $E_T > 18$ GeV	$2.96 \cdot 10^5$	1.01	300k
NC DIS	DJANGO 1.1	$Q^2 > 100$ GeV^2	$8.12 \cdot 10^3$	73.89	580k
CC DIS	DJANGO 1.1	$Q^2 > 100$ GeV^2	34.7	$5.76 \cdot 10^3$	200k
$\gamma\gamma \to \tau^+\tau^-$ (DIS1)	GRAPE-Dilepton	$p_T^\ell > 5$ GeV, $5° < \theta^\ell < 175°$	5.24	$1.05 \cdot 10^3$	5.5k
$\gamma\gamma \to \tau^+\tau^-$ (DIS2)	GRAPE-Dilepton	$p_T^\ell > 5$ GeV, $5° < \theta^\ell < 175°$	1.04	$2.88 \cdot 10^3$	3k
$\gamma\gamma \to \tau^+\tau^-$ (DIS3)	GRAPE-Dilepton	$p_T^\ell > 5$ GeV, $5° < \theta^\ell < 175°$	0.95	$3.16 \cdot 10^3$	3k
$\gamma\gamma \to \tau^+\tau^-$ (DIS4)	GRAPE-Dilepton	$p_T^\ell > 5$ GeV, $5° < \theta^\ell < 175°$	0.48	$6.26 \cdot 10^3$	3k
$\gamma\gamma \to \tau^+\tau^-$ (QELA1)	GRAPE-Dilepton	$p_T^\ell > 5$ GeV, $5° < \theta^\ell < 175°$, $M^{had} > 5$ GeV	0.10	$2.87 \cdot 10^4$	3k
$\gamma\gamma \to \tau^+\tau^-$ (QELA2)	GRAPE-Dilepton	$p_T^\ell > 5$ GeV, $5° < \theta^\ell < 175°$, 1.08 GeV $< M^{had} < 5$ GeV	3.56	$1.12 \cdot 10^3$	4k
$\gamma\gamma \to \tau^+\tau^-$ (ELA)	GRAPE-Dilepton	$p_T^\ell > 5$ GeV, $5° < \theta^\ell < 175°$	6.35	$1.02 \cdot 10^3$	6.5k

Table 5.1: List of the simulated processes along with the name of the used Monte Carlo generators, the applied kinematic cuts and the corresponding cross sections, integrated luminosities and number of events. u_{cut} corresponds to the kinematic cut, used to regularise the poles occurring in the cross section calculations for $W^\pm$ production. E_T is the energy scalar sum of all produced particles and Q^2 is the momentum transfer squared. There are seven subprocesses for τ pair production with the following meaning: deep inelastic scattering of e and u quark (DIS1), deep inelastic scattering of e and $\bar{u}$ quark (DIS2), deep inelastic scattering of e and d/s quarks (DIS3), deep inelastic scattering of e and $\bar{d}/\bar{s}$ quarks (DIS4), quasi elastic scattering with hadronic mass > 5 GeV (QELA1), quasi elastic scattering with 1.08 $<$ hadronic mass < 5 GeV (QELA2) and elastic scattering (ELA). p_T^ℓ refers to the transverse momentum of the lowest p_T τ lepton and M^{had} to the invariant mass of the hadronic system. At least one τ lepton with polar angle θ^ℓ is required to be in the range between 15° and 175°.

Chapter 6

Discrimination Technique

The discrimination of τ lepton induced jets from QCD induced jets is considered to be a major challenge in this analysis. For this purpose a multivariate discrimination technique, first introduced in [26], is used.

6.1 Jet Classification

In order to separate a distinct type of jets among a large number of background jets, one has to classify the jets in terms of appropriate jet properties. For a given signal and background the probability, whether a jet belongs to a signal or background type of jet, can be calculated for each jet by combining jet properties (in the following denoted as 'jet observables').

Therefore the density functions of the signal ρ_s and background jets ρ_b at a certain point $\vec{\mathbf{x}}$ in the observable space are calculated. Assuming that we have n jet observables with quantities, described by the n-tuple $\vec{\mathbf{x}} = (x_1, \ldots, x_n)$, the probability, whether it is a signal type of jet or also called the discriminant $D(\vec{\mathbf{x}})$ is calculated through

$$D(\vec{\mathbf{x}}) = \frac{\rho_s(\vec{\mathbf{x}})}{\rho_b(\vec{\mathbf{x}}) + \rho_s(\vec{\mathbf{x}})}. \tag{6.1}$$

For known ρ_s and ρ_b, $D(\vec{\mathbf{x}})$ can be calculated for each jet and gives the probability that this jet is a signal type jet.

The quality of the classification scheme can be charcterised by the quantities efficiency ϵ, rejection R and separation power S, which are defined as follows:

$$\epsilon \equiv \epsilon_s = \frac{N_s^{sel}}{N_s^{tot}}, \tag{6.2}$$

$$R \equiv \epsilon_b^{-1} = \left(\frac{N_b^{sel}}{N_b^{tot}}\right)^{-1} = \frac{N_b^{tot}}{N_b^{sel}}, \tag{6.3}$$

$$S \equiv \frac{\epsilon_s}{\epsilon_b} = \frac{N_s^{sel} \cdot N_b^{sel}}{N_b^{tot} \cdot N_s^{tot}}, \tag{6.4}$$

where N_{sample}^{sel} and N_{sample}^{tot} stands for the number of events which has at least one jet with the required selection criteria and the total number of events, respectively.

6.2 The Discrimination Method

The density functions are estimated in the vicinity of a certain point $\vec{\mathbf{x}}$ with the volume $V(\vec{\mathbf{x}})$ in the observable space. The ratio

$$\ell(\vec{\mathbf{x}}) = \frac{\#signal\ jets\ in\ V(\vec{\mathbf{x}})}{\#background\ jets\ in\ V(\vec{\mathbf{x}})} \approx \frac{\rho_s(\vec{\mathbf{x}})}{\rho_b(\vec{\mathbf{x}})} \tag{6.5}$$

in each box is used to calculate the discriminant

$$D(\vec{\mathbf{x}}) = \frac{\rho_s(\vec{\mathbf{x}})}{\rho_b(\vec{\mathbf{x}}) + \rho_s(\vec{\mathbf{x}})} \approx \frac{\ell(\vec{\mathbf{x}})}{1 + \ell(\vec{\mathbf{x}})}. \tag{6.6}$$

The reference signal and background events/jets are sampled with Monte Carlo generated events, from which a large number is needed to densely populate the whole phase space.

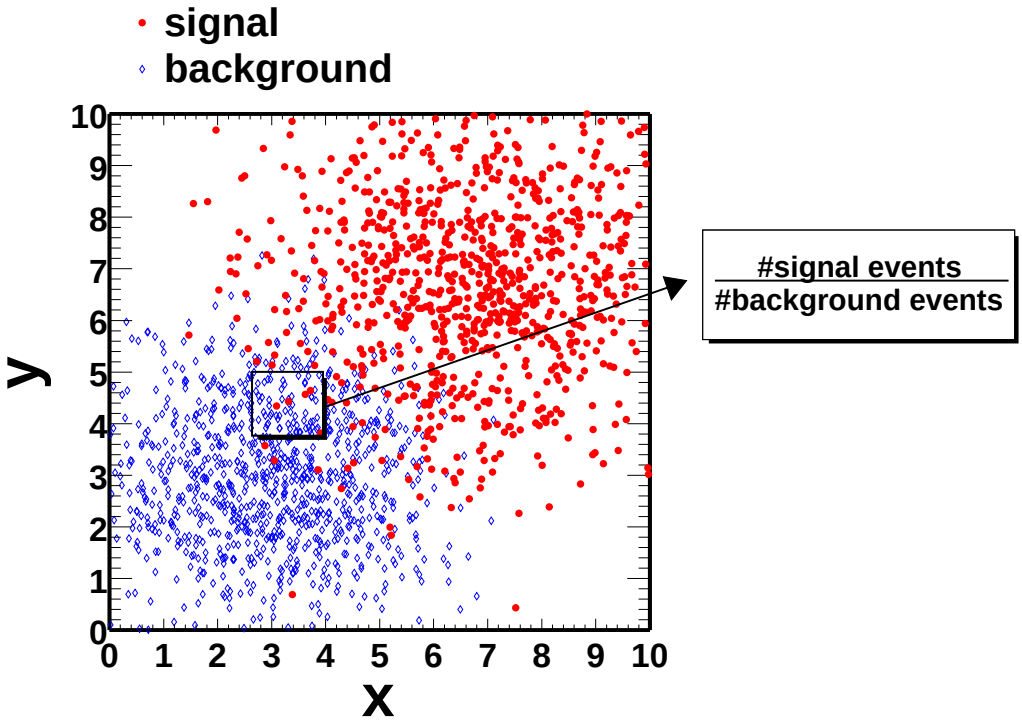

Figure 6.1: Example for a 2-dim. observable space (x, y). The diamonds represent the background and the dots the signal jets. E.g. if the jet that is to be classified is located in the highlighted box, $\ell(\vec{\mathbf{x}})$ of this jet is obtained by counting the number of signal and background jets in this box.

An example is given in Fig. 6.1, in which two arbitrary observables x and y span a 2-dim. phase space. The reference signal sample is represented by the dots and the background samples by the diamonds. E.g. if the jet that is to be classified is located in the highlighted box, $\ell(\vec{\mathbf{x}})$ of this jet is obtained by counting the number of signal and background jets in this box.

The quality of this separation method depends mainly on three parameters:

1. *The choice of the observables*: Each observable has to possess a certain potential to discriminate the two jet classes and correlations between the observables are required to be small. High correlations between observables would not spoil the accuracy of the method, but would lead to a waste of computational resources. Feeding the algorithm with highly correlated variables means calculation of a set of redundant information. Redundancy spoils the efficiency of any computional algorithmn.

2. *The accuracy of the MC reference events*: The event generators and the detector simulations used to sample the signal and background distributions are required to simulate the distributions of the true physical processes very well. In other words the applicability of the discriminant is based on the reliablility of the reference samples.

3. *The number of reference events and box size*: Even the outermost regions of the phase space has to be filled with both signal and background events. To estimate properly the probability density in each region a not too small number of events has therefore to be required. If the number is too small, the statistical precision can be also too small and certain events remain unclassified. The precision depends also on the size of the boxes . But if a large enough number of events is available, the box size does not influence the results very much as it is shown in [27].

In the following the advantages and disadvantage of the used multiobservable discrimination technique (MODT) in comparison with other popular methods like the original Maximun-Likelihood-Method, an Artificial Neuronal Network (ANN) or the combination-of-cuts are listed, for a more detailed discussion see Ref. [27].

Advantages:

- The MODT takes into account the corellation between different observables. The observables in the standard Maximum-Likelihood-methods are projected to the axes of the phase space before calculating the classificator. This spoils the discrimination power, because the correlations are not taken into account accurately.

- The optimisation phase is usually shorter for the MODT than the time to optimise an Artificial Neuronal Network. It is a straight forward calculation and less human intervention in adjusting the parameters of the algorithm is necessary.

Disadvantages:

- Large samples of reference events are required to fill all boxes and to obtain enough statistics needed for a statistically reliable estimation.

- The Monte Carlo simulations are required to describe the true physical quantities very reliably.

6.3 The Range Searching Algorithm

The simplest way to count the number of jets in the vicinity of a certain point in an n-dim. variable space is to divide the space into boxes, loop over all events, calculate their coordinates and store the number of events in each box. With a growing number of events and dimensions this algorithm is very memory and time consuming. Since the discrimination method described in the section 6.2 has to include many MC events, i.e. many jets distributed in a multi-dimensional variables space, a much more efficient algorithm is needed for the implementation.

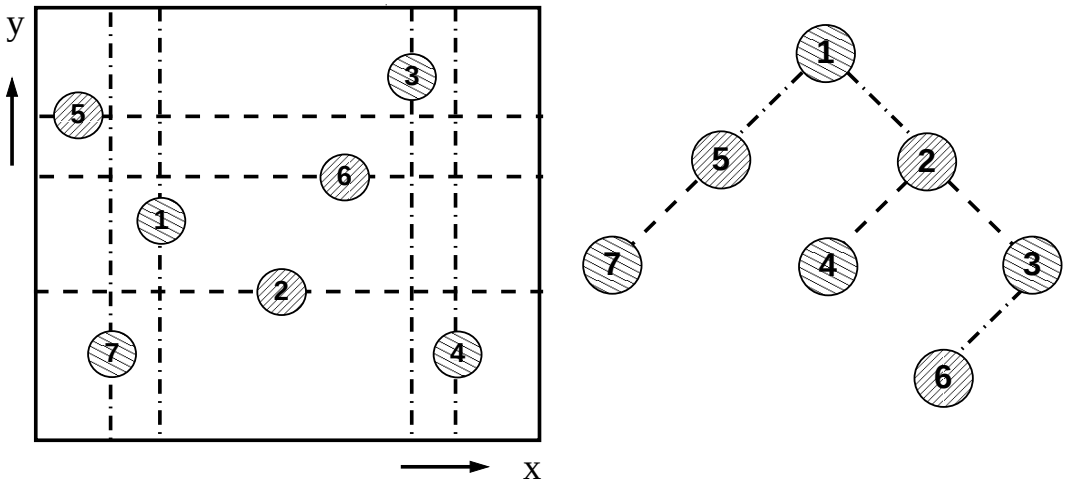

Figure 6.2: Example of a binary tree storing seven jets according to their position in the x-y plane, starting with the first jet on the top node of the tree. According to the x-value of the next jet it is stored as the left or the right node, respectively. In the next iteration step the jets are sorted with respect to y.

Counting the number of jets in the vicinity of a certain point in an n-dim. variable space is known as 'range searching'. Range searching algorithms have been developed which allow a search time $\propto log(n)$, where n is the number of points that have to be searched [28]. The algorithm used in this analysis is described in [27] in detail. This algorithm uses binary trees to store the jets (a 2-dim. example is depicted in Fig. 6.2) and is especially suitable for a large number of jets and dimensions (i.e. observables).

The MC jets are successively filled into the nodes of two binary trees, one for the signal and one for the background jets. While descending the tree the decision quantity cycles through all considered discriminating observables $x_i = x_1, \ldots, x_n$ from the tuple $\vec{\mathbf{x}} = (x_1, \ldots, x_n)$, starting with x_1 of the first jet in the first event, then x_2 etc. After processing x_n in the first jet, again x_1 of the second jet is processed and so on, ending with x_n of the last jet in the last event. The decision whether to descend to the left or to the right of a node depends on the value of the current jet observable (if the value of the current observable x_i is smaller than x_i of the jet before, then store the jet to the left daughter node, otherwise vice

versa). After filling, the position of every jet in the tree is given by its coordinates in the phase space.

The searching in the trees is done in the same manner as the filling. E.g. if the complete box lies below the root jet j_i, only the jets at the left to j_1 has to be considered for further searching. Otherwise, if the complete box lies above j_1, then descend to the right subtree, etc. Hence, after each step the number of searched nodes will be halved, if the initialisation of the tree ensured a well-balanced tree[1].

[1]Therefore the root jet has to lie more or less in the center of the phase space covered by the sample events.

Chapter 7

Identification of τ Leptons

This chapter presents the characteristics of τ lepton decays and introduces the observables exploiting the internal structure of jets[1] induced by τ lepton decays. Based on this information the discrimination technique described in chapter 6 is used to separate τ lepton induced jets (in the following called 'τ jets') from quark and gluon induced jets ('QCD jets').

7.1 The Decay of τ Leptons

With a rest mass of $m_\tau = 1777.03^{+0.30}_{-0.26}$ MeV (world average [10]), which is almost twice the rest mass of the proton ($m_p = 938.272 \pm 0.00004$ MeV [10]), the τ lepton is the heaviest known lepton. Since it is the only lepton which has a rest mass higher than the rest mass of a pion ($m_\pi = 139.67018 \pm 0.00035$ MeV [10]), which is the lightest known hadron, the τ lepton is the only lepton heavy enough to decay into hadrons. The mean lifetime of $\tau = (290.6 \pm 1.1) \cdot 10^{-15}$ s [10] leads to $c\tau = 87.11$ μm. The main decay modes of the τ-lepton and the appropriate branching ratios are listed in Tab. 7.1[2]. With a branching ratio of about 35% the τ lepton decays either into electrons or muons and in almost all other cases ($\sim 65\%$) it decays into one (1-prong), three (3-prong) or five (5-prong) charged hadrons ($\pi^\pm$ or $K^\pm$), a τ neutrino (ν_τ) and zero or more neutral hadrons (π^0 or K^0).

7.2 Characteristics of τ Jets

The hadrons emerging from a decay of a τ lepton can be measured with the ZEUS calorimeter as hadronic jets, i.e. collimated bundle of hadrons. The decay of the τ lepton is a two or more-body decay. If the τ lepton is produced with a high momentum, the decay particles will be strongly boosted in the direction of the τ lepton. Therefore the jet will be collimated. Jets which are induced by quarks or gluons can radiate gluons in the fragmentation phase. Moreover,

[1] The definition of jets used in this analysis can be found in appendix A.

[2] The table corresponds to the decays of τ^- leptons. The decays for τ^+ leptons are analogous and within the given precision the quantities are the same.

τ^-	$\longrightarrow$	$e^-\ \bar{\nu}_e\ \nu_\tau$	17.8%
τ^-	$\longrightarrow$	$\mu^-\ \bar{\nu}_\mu\ \nu_\tau$	17.4%
τ^-	$\longrightarrow$	$had^-\ \nu_\tau\ \geq 0\ neutrals$	49.5%
τ^-	$\longrightarrow$	$2had^-\ had^+\ \nu_\tau\ \geq 0\ neutrals$	15.2%
τ^-	$\longrightarrow$	$3had^-\ 2had^+\ \nu_\tau\ \geq 0\ neutrals$	0.1%

Table 7.1: The main decay modes of τ^- leptons and the appropriate branching ratios [10]. $had^\pm$ indicates a charged hadron and *neutrals* denotes a neutral hadron. The table for τ^+ leptons can be written in an analogous way.

they are connected by the colour charge to the rest of the final state. Due to the colour neutrality of the τ lepton, which inhibits quark and gluon radiation, they are expected to be more collimated than jets induced by quarks and gluons. τ jets can be distinguished from QCD jets by exploiting the following properties:

1. Low charged particle multiplicity
2. Pencil like shape of the energy depositions
3. Total charge of ± 1
4. Secondary vertex

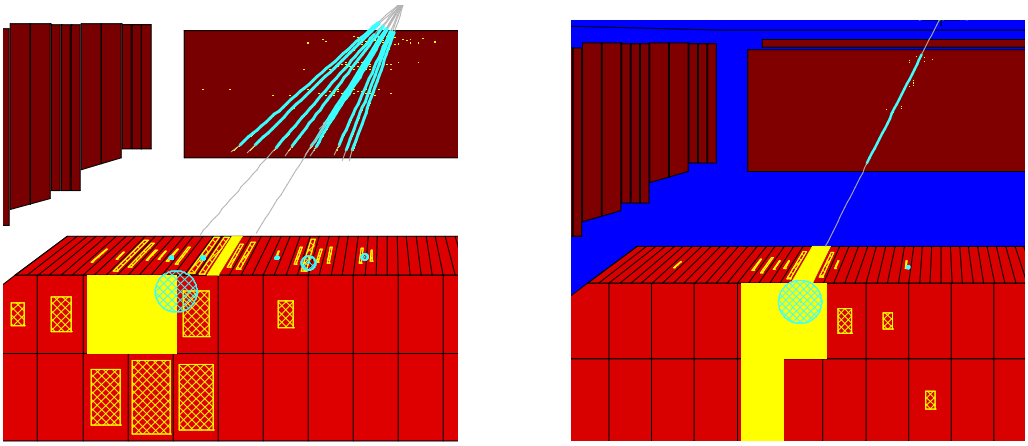

a) **b)**

Figure 7.1: Response of the ZEUS detector to (a) a typical QCD-jet and to (b) a typical τ jet.

Low charged particle multiplicity means that the number of tracks associated with the jet is small. A pencil like shape of the energy depositions corresponds to a highly collimated jet, i.e. a relatively narrow cluster in the calorimeter. The charge of the jet is defined as the summed charge of all tracks associated with the jet. The expected decay length of the τ lepton is so small, that the secondary vertex can not be measured with the present ZEUS detector[3].

Fig. 7.1a shows the typical response of the ZEUS detector to a typical QCD-jet originating from a photoproduction process. The cluster cells are widespread and the number of tracks pointing to this cluster is high. In contrast the τ jet (Fig. 7.1b) has a narrow cluster and only a small number of tracks (one track in Fig. 7.1b) is associated with the jet.

7.3 Definition of Observables characterising τ Jets

In order to exploit the general properties of τ jets, described in section 7.2, appropriate observables are defined in the following. Many of these observables are correlated. The goal is to find the optimal set of observables with highest separation power and lowest correlations, in order to use them as input to the MODT algorithm (see chapter 6). The selection of the final set of observables will be described in section 7.4.2.

The 13 jet observables, which are studied in this analysis are called $ntrk$, $trkfrac$, $|charge|$, $|chargeEW|$, $rmean$, $rrms$, $lmean$, $lrms$, $r90$, $remc$, $ncells$, $mass$ and $subj$. In all following figures the term '*jet density*' denotes that the distributions giving the number of jets are normalised to one ('shape normalised'). Each plot shows the distributions for the $W \to \nu\tau$ MC[4], where the τ lepton decays hadronically, and for the CC DIS MC, providing a representation sample of QCD jets. Note that the index i occurring in the formulae either denotes calorimeter cells or tracks associated with the jet. Also note that all distributions are shown after the preselection cuts, described in section 7.4.1. The observables are defined as follows:

Track based Observables

- $ntrk$: Number of tracks associated with the jet[5].

- $trkfrac$: Fraction of the momentum of the leading track to the momentum

[3]Recently, a silicon micro vertex detector (MVD) has been installed. It was designed to be able to measure impact parameters of $\mathcal{O}(100\ \mu\text{m})$ [29]. Hence, a possible identification of the secondary τ lepton vertex will require an excellent understanding of this new detector.

[4]In the following the term '$W \to \nu\tau$' stands for both, '$W^+ \to \tau^+\nu_\tau$' and '$W^- \to \tau^-\bar{\nu}_\tau$'

[5]A track is required to have a transverse momentum higher than 200 MeV and the reconstructed track trajectory should point to the reconstructed primary vertex with at least three CTD superlayers hit ('vertex fitted track'). A track is associated with the jet, if the $\{\eta,\phi\}$-distance R_i between the jet axis and the track i is less than or equal 1, with $R_i = \sqrt{\Delta\phi_i^2 + \Delta\eta_i^2}$, where ϕ is the azimuth angle and $\eta \equiv -\ln(\tan\frac{\theta}{2})$ is the pseudorapidity and θ is the polar angle, measured with respect to the proton beam direction.

of all tracks associated with the jet, where the leading track is the highest transverse momentum track.

$$trkfrac = \frac{p(leading\ track)}{\sum_i p_i} \tag{7.1}$$

$ntrk$ and $trkfrac$ are highly correlated, because in about two third of all hadronic decays the charged track multiplicity is expected to be one (see Tab. 7.1), due to the 1-prong decays of the τ lepton. Hence, the distributions of both observables are expected to peak at $(\pm)1$ (see Fig. 7.2).

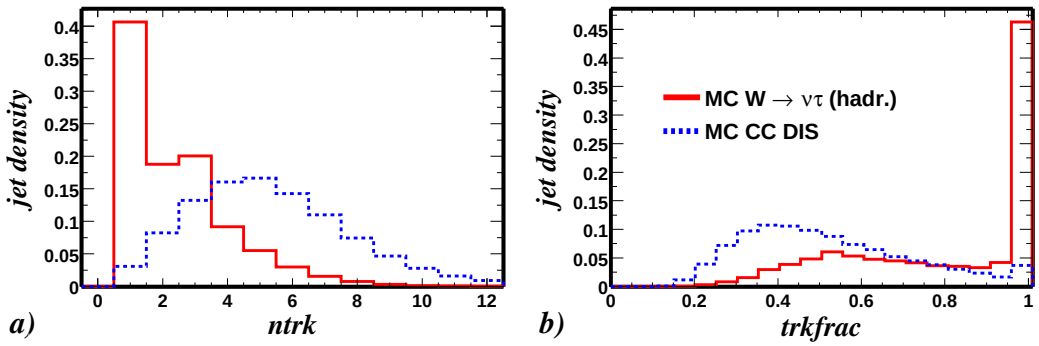

Figure 7.2: Jet density of (a) $ntrk$ and (b) $trkfrac$. The $W \to \nu\tau$ and the CC DIS MC are represented by the solid and the dashed line, respectively.

Charged based Observables

- $|charge|$: Absolute value of the total net charge of all tracks associated with the jet.

$$|charge| = \left\| \sum_i Q_i \right\|, \tag{7.2}$$

  where Q_i is the charge of track i.

- $|chargeEW|$: Absolute value of the energy weighted total net charge of all tracks associated with the jet.

$$|chargeEW| = \left\| \frac{\sum_i \{E_i \cdot Q_i\}}{\sum_i E_i} \right\| \tag{7.3}$$

In Figure 7.3 the distributions for $|charge|$ and $|chargeEW|$ are depicted. Both, $|charge|$ and $|chargeEW|$ are also expected to be highly correlated with $ntrk$ and $trkfrac$, since if $ntrk$ is one $|charge|$ and $|chargeEW|$ also have to be one.

Calorimetric Jet Moments

The observables $rmean$, $rrms$, $lmean$, $lrms$ constitute the first and second moment characterising the radial and longitudinal extension of the jet. They measure the shapes of jets in the $\{\eta, \phi\}$-plane (radial) and along the jet direction (longitudinal).

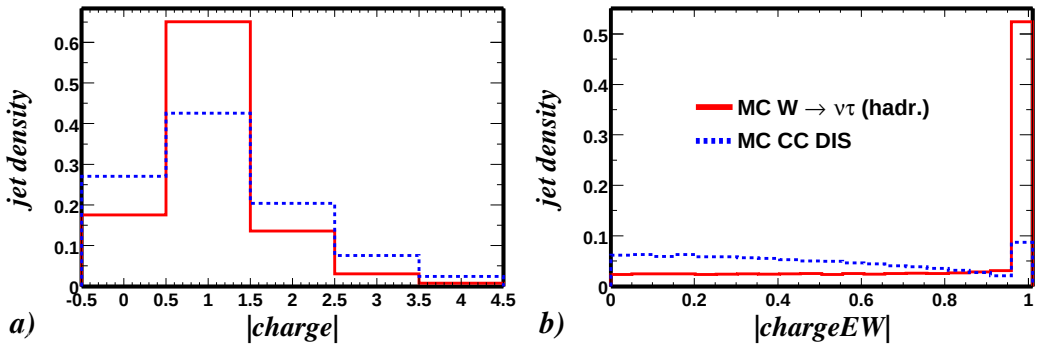

Figure 7.3: Jet density of (a) *charge* and (b) *chargeEW*. The solid line shows the distribution for $W \to \nu\tau$ MC and the dashed line shows the one for CC DIS MC.

- *rmean*: Energy weighted mean of the $\{\eta, \phi\}$-distance R_i of each cell in the jet with respect to the jet axis or first moment of the radial extension quantity R.

$$rmean = \langle R \rangle = \frac{\sum_i \{E_i \cdot R_i\}}{\sum_i E_i} \tag{7.4}$$

- *rrms*: Energy weighted root-mean-square (RMS) of R_i of all cells in the jet with respect to the jet axis or second moment of the radial extension quantity R.

$$rrms = \sqrt{\frac{\sum_i E_i \cdot (\langle R \rangle - R_i)^2}{\sum_i E_i}}, \tag{7.5}$$

  where $\langle E_i \cdot R_i \rangle$ indicates the mean of $E_i \cdot R_i$.

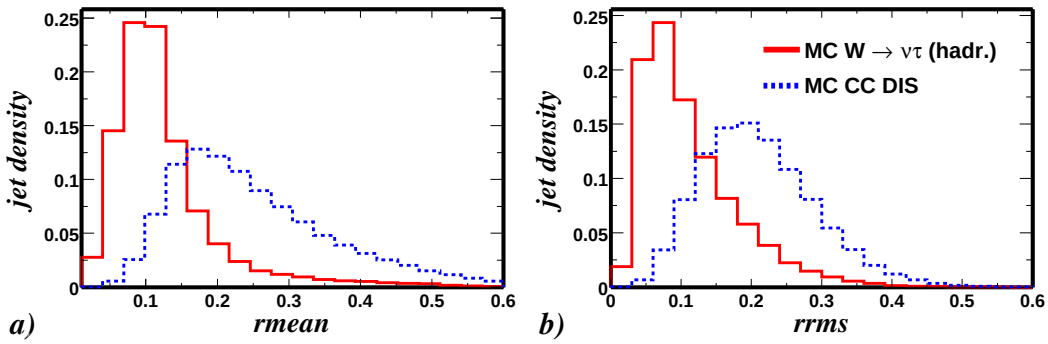

Figure 7.4: Jet density of (a) *rmean* and (b) *rrms*. The solid line shows the distribution for $W \to \nu\tau$ MC and the dashed line shows the one for CC DIS MC.

- *lmean*: Mean of the reconstructed momentum of each particle[6] which is associated with the jet and projected to the direction of the jet axis or first

[6]Here, a hit calorimeter cell is identified as a particle: hit cell ≡ particle. The index i runs over all particles.

moment of the longitudinal extension quantity L.

$$lmean = \langle L \rangle = \frac{\sum_i L_i}{N}, \text{ with } \mathrm{L_i} = \mathrm{p_i} \cdot \cos\theta_\mathrm{i}, \tag{7.6}$$

where p_i is the magnitude of the particle's reconstructed momentum three-vector (see Fig. 7.5).

- $lrms$: RMS of the momentum of each particle associated with the jet projected to the direction of the jet axis or second moment of the longitudinal extension quantity L.

$$lrms = \sqrt{\frac{\sum_i (\langle L \rangle - L_i)^2}{N}}. \tag{7.7}$$

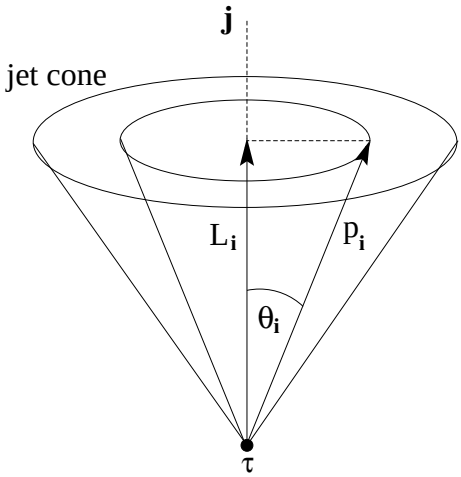

jet cone: Cone of the whole jet.

τ: Vertex of τ decay.

j: Jet axis.

p_i: Momentum vector of one particle.

θ_i: Angle between jet axis and p_i.

L_i: Projected p_i to jet axis.

Figure 7.5: Sketch to illustrate the definitions of the calorimetric jet moments.

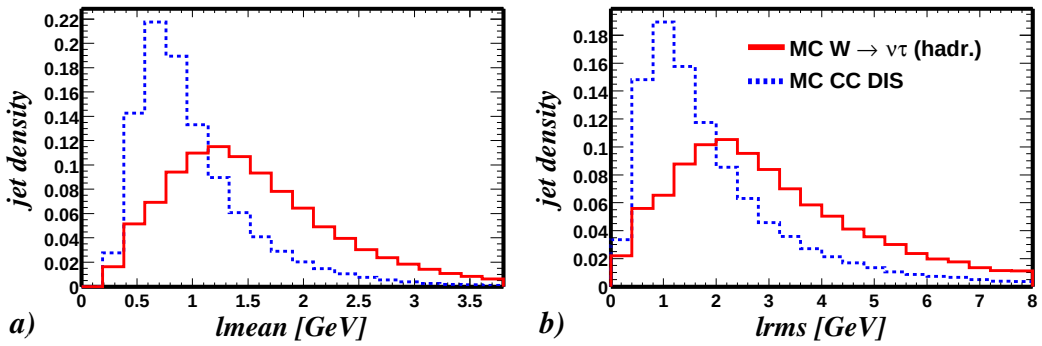

Figure 7.6: Jet density of (a) $lmean$ and (b) $lrms$. The solid line shows the distribution for $W \to \nu\tau$ MC and the dashed line shows the one for CC DIS MC.

The quantities defining $lmean$ and $rmean$ are illustrated in Figure 7.5. In this picture τ indicates the vertex, where the τ lepton decays into hadrons. The

vector declared as p_i denotes the reconstructed momentum of one particle which is associated with the jet. θ_i is the angle between p_i and the jet axis. The vector L_i is the particle momentum projected to the jet axis.

The values of *rmean* and *rrms* for τ jets are small compared with the ones for QCD jets as can be seen in Figure 7.4a-b, since small values indicate the pencil-likeness of a jet. Whereas *lmean* and *lrms* is greater for τ jets than for QCD jets as can be seen in Figure 7.6a-b.

Further Calorimetric Jet Observables

- $r90$: Radius of the $\{\eta, \phi\}$-cone centered around the jet axis that contains 90% of the total jet energy.

- *remc*: $\{\eta, \phi\}$-distance of the remotest EMC cell, which belongs to the jet with respect to the jet axis.

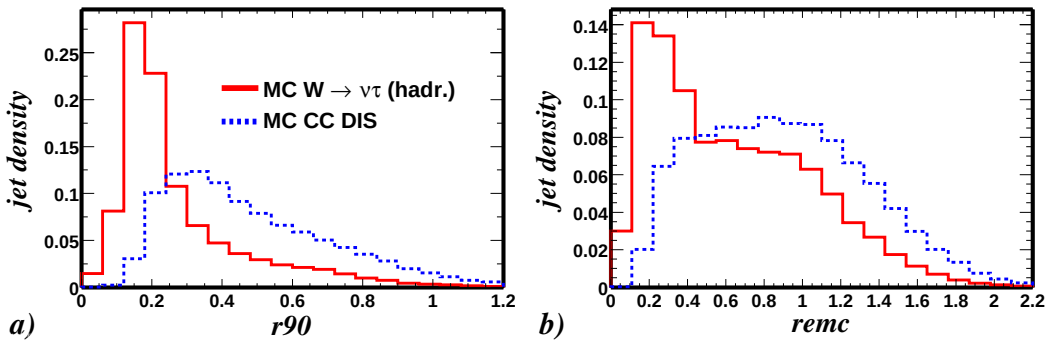

Figure 7.7: Jet density of (a) *rmean* and (b) *remc*. The solid line shows the distribution for $W \to \nu\tau$ MC and the dashed line shows the one for CC DIS MC.

These two observables are also closely connected to the pencil-likeness of a jet. Hence, they are both expected to be smaller for τ jets than for QCD jets (see Fig. 7.7a-b).

- *ncells*: Number of cells associated with the jet.

- *mass*: Invariant mass of all cells associated with the jet.

$$mass = \sqrt{(\sum_i E_i)^2 - (\sum_i p_{i,x})^2 - (\sum_i p_{i,y})^2 - (\sum_i p_{i,z})^2} \qquad (7.8)$$

- *subj*: Number of subjets with a y_{cut} of $5 \cdot 10^{-4}$.
  The subjet multiplicity identifies the number of localized energy depositions within a jet that can be resolved using a certain resolution criterium called y_{cut}. A value $y_{cut} = 5 \cdot 10^{-4}$ was found to give the best separation. The number of localised energy depositions (subjets) is found by applying the same algorithm as was used to find jets. Fig. 7.9 demonstrates the meaning

of y_{cut}. The jet is defined by clustered energy depositions in the calorimeter. With decreasing y_{cut} the power to resolve subjets in the jet increases. This leads to an increasing number of subjets[7].

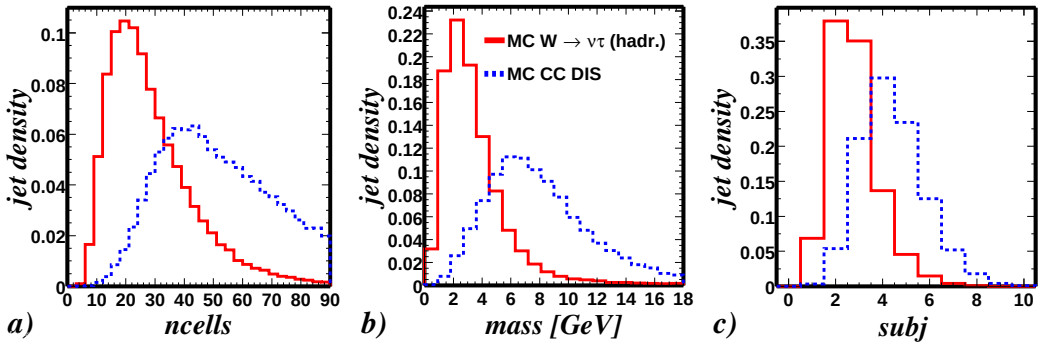

Figure 7.8: Jet density of (a) *ncells* (b) *mass* and (c) *subj*. The solid line shows the distribution for $W \to \nu\tau$ MC and the dashed line shows the one for CC DIS MC.

For τ jets the quantities for *ncells*, *mass* and *subj* should be small compared with the values for QCD jets, since they are also connected to the pencil-likeness of a jet (see Fig. 7.8a-b).

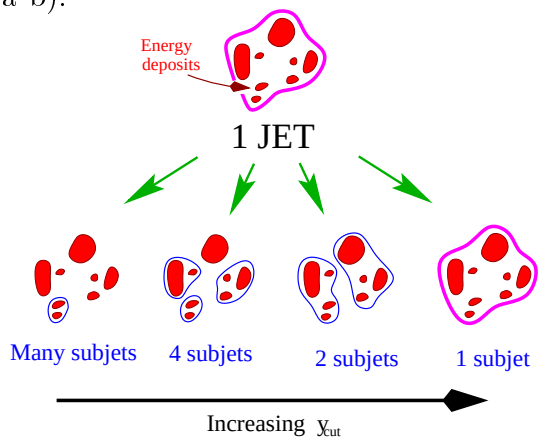

Figure 7.9: Subjets and the meaning of y_{cut}. The smaller y_{cut} the higher the resolution power of the subjet algorithm and the more subjets can be seen.

Observables to reject Electrons

Since electrons can also produce a narrow cluster in the calorimeter with only one track associated with the jet, they are a serious background source. To reject electrons a combined cut on two additional observables is applied, $emfrac$ and $fltf$, where $fltf = emfrac + ltf$, which are defined as follows:

- $emfrac$: Energy fraction deposited in the EMC.

$$emfrac = \frac{E_{EMC}}{E_{tot}} \tag{7.9}$$

[7] For a detailed description of subjets and the meaning of the parameter y_{cut} see [30].

- ltf: Ratio of the highest p_T track with respect to the jet energy.

$$ltf = \frac{p_T(leading\ track)}{E_{jet}} \tag{7.10}$$

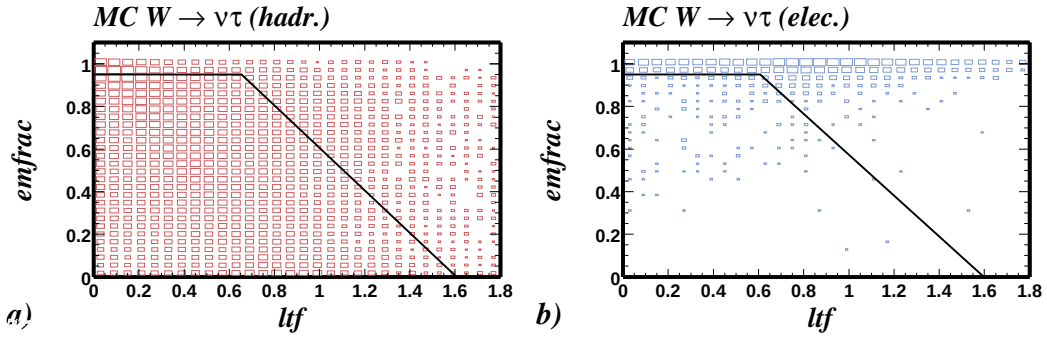

Figure 7.10: Correlation between $emfrac$ and ltf for a) τ jets and b) electrons coming from a $W^{\pm}$ boson decay, respectively. The solid line in each plot corresponds to $emfrac = 0.95$ and $fltf = emfrac + ltf = 1.6$.

Figure 7.10 shows the correlation between $emfrac$ and ltf. A cut at $emfrac = 0.95$ and $fltf = emfrac + ltf = 1.6$, indicated by the solid lines, leads to a good separation of electrons and τ jets. 78.5% of the τ jets passed this cut, while 96.8% of the electrons are rejected.

7.4 Separation of τ Jets from QCD jets

The multi observable discrimination technique (MODT), described in chapter 6 is the major tool in this analysis to separate τ induced jets from QCD jets. It allows to combine the observables defined in section 7.3 in a single quantity - the discriminant ($D(\vec{\mathbf{x}})$), which can be used to discriminate different classes of jets (e.g. τ jets and QCD jets). The aim is to find the optimal set of observables with highest separation power, which will be described in the following sections.

7.4.1 Preselection

This section presents the preselection cuts, applied to ensure the quality of the measured jets and tracks before they are processed in the MODT algorithm. Additionally, the electron rejection cut is applied, since electrons can mimic τ jets. A very strict $\not{p}_T$-cut is made to reject most of the photoproduction and NC DIS backround events. This cut is necessary, since the shapes of the jet distributions depends on the underlying physical process, i.e. the kinematics of the jets. The higher the transverse momentum of jets the more collimated they are. The jet transverse momentum disribution in high missing transverse momentum events is shifted to higher p_T values with respect to the one in low missing transverse momentum events as can be seen in Figure 7.11a. The minimum at about 10 GeV

is due to the jet energy correction algorithm, which takes into account the inactive materials before the calorimeter. This algortihm is waranted for jet transverse momentum higher than 14 GeV and was applied for jets with $p_T^{jet} > 10$ GeV. The energy correction for jets in the transverse momentum range from 10 to 12 GeV is in general too high, leading to an depletion of this p_T^{jet} band. Since the contribution of this band is small after the $\not{p}_T$-cut, it can be neglected and is not expected to spoil the further analysis. As can be seen in Figures 7.11b-c *rmean* is slightly shifted to lower and *lmean* is shifted to higher amounts for the high missing transverse momentum jets as expected. In the case of *ncells* the distribution is shifted very slightly to higher values, even though the jets are more collimated. This is due to the higher energy of the jets leading to a higher energy deposition in the calorimeter. Also the distribution of the invariant jet mass are shifted to higher values. The distribution of *subj* remains nearly unchanged.

Hence, it important that one has to define the background jets in order to find the signal jets.

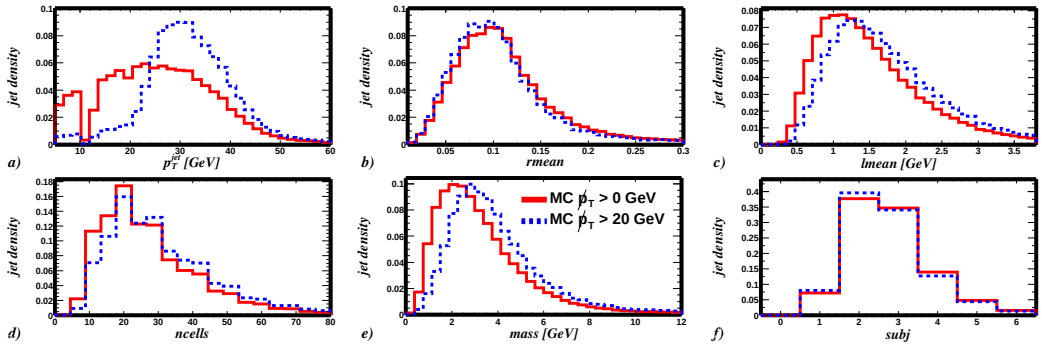

Figure 7.11: Shape normalised number of jets with (dashed line) and without (solid line) the cut $\not{p}_T > 20$ GeV for (a) the jet transverse momentum, (b) *rmean*, (c) *lmean*, (d) *ncells*, (e) *mass* and (f) *subj*.

Quality Cuts

To ensure that only well measured jets and tracks are used, some quality cuts were applied:

- The energy of EMC cells are required to measure an energy higher than 100 MeV, while those from the HAC1 and HAC2 are required to be above 150 MeV:
  - $E_{EMC} > 100$ MeV
  - $E_{HAC} > 150$ MeV
- Good tracks are required to have a transverse momentum higher than 200 MeV and point to the primary vertex:
  - $p_T^{track} > 200$ MeV

- A good jet is defined with a transverse momentum above 5 GeV and with at least one track pointing to the cluster:
  - $p_T^{jet} > 5$ GeV
  - $ntrk \geq 1$
- Due to the CTD acceptance the jet polar angle θ_{jet} should lie between 15 and 164 degrees:
  - $15^\circ < \theta^{jet} < 164^\circ$
- The z-component of the event interaction $zvtx$ is required to be less than 40 cm from the nominal interaction point:
  - $|zvtx| < 40$ cm

Electron Rejection

- In order to reject electrons the combined cuts $emfrac < 0.95$ and $fltf = emfrac + ltf < 1.6$ are applied (see section 7.3):
  - $emfrac < 0.95$
  - $fltf < 1.6$

Transverse Missing Momentum

Figure 7.12 shows the cross section[8] per bin as a function of the missing transverse momentum for the signal and background processes. The solid line corresponds to the $W \to \nu\tau$ MC, where the τ leptons decay hadronically (in the following denoted as 'τ MC') and the dashed line corresponds to the CC DIS MC. The dotted and the dashed-dotted lines correspond to the photoproduction and the NC DIS MC's, respectively. The hatched histogram shows the distribution for τ pair production. As expected the CC DIS and the τ MC populate a wide range up to $\not{p}_T = 90$ GeV (τ MC) and $\not{p}_T > 100$ GeV (CC DIS MC), whereas most of the MC events from photoproduction, NC DIS and τ pair production lie at small $\not{p}_T$. To reject most of the background the events are required to have a missing transverse momentum higher than 20 GeV. The main background after this cut is expected to be CC DIS events. Hence, this analysis is especially tuned to discriminate the τ signal from CC DIS jets at high missing transverse momentum[9]. A good separation is needed, since the cross section for $W \to \nu\tau$ processes is small ($\sigma_\tau(\not{p}_T > 20$ GeV$) \approx 44$ fb) compared to CC DIS processes ($\sigma_{CC}(\not{p}_T > 20$ GeV$) \approx 25$ pb), even for the very strict requirement of $\not{p}_T > 20$ GeV.

[8] This is the experimental cross section as measured in the ZEUS detector. The number of MC events is normalised with the luminosity of each subprocess.

[9] A general approach to separate τ jets from jets originated from CC DIS, NC DIS and photoproduction processes is presented in appendix B.

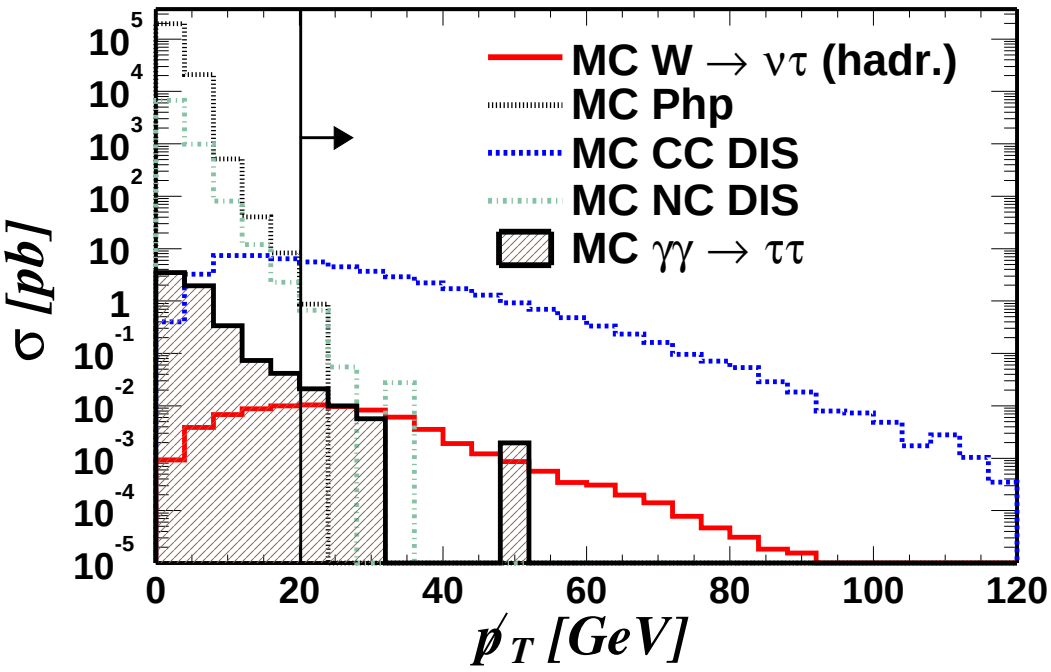

Figure 7.12: The cross section as a function of the missing transverse momentum / p_T for the signal and background MC processes: $W \to \nu\tau$ MC, where the τ leptons decay hadronically (solid line), CC DIS (dashed line), NC DIS MC (dashed-dotted line), τ pair production (hatched) and photoproduction MC (dotted line). The line and the arrow indicate the cut $\not{p}_T = 20$ GeV.

In Figure 7.12 one can see that the MC statistics is not sufficient for NC, photoproduction and τ pair production at high $\not{p}_T$. NC DIS, γp and $\gamma\gamma \to \tau\tau$ events are still expected to contribute a not negligible amount of events to the background after applying the $\not{p}_T$-cut. Note that the NC MC statistics approximately corresponds to the data luminosity. The photoproduction MC corresponds to less than ten per cent of the data luminosity. Unfortunately there was not enough time left to include more MC events or to investigate further cuts in order to obtain cleaner data samples.

Summary

After sequentially applying all cuts, which are summarised in Table 7.2, the main background is expected to be CC DIS events, as can be seen in Table 7.3. There the number of events passing each cut for the different process are listed, where the cuts 1.-5. in Table 7.2 are called 'Quality Cuts'. One of the main efficiency losses is due to the fact that many τ jets are not produced in the acceptance range of the CTD or have low transverse momentum.

Since the percentage of events which pass all preselection cuts is below 1% for the photoproduction, the NC DIS and the two photon processes, the remaining background after these cuts are CC DIS events. Hence, in the following the selec-

Preselection Cuts	
1. Good cells	$E_{EMC} > 100 MeV$ $E_{HAC} > 150 MeV$
2. Good track	$p_T^{track} > 200 MeV$
3. Good jet	$p_T^{jet} > 5$ GeV
4. CTD acceptance	$15° < \theta^{jet} < 164°$
5. Good vertex	$\|zvtx\| < 40$ cm
6. Electron rejection	$emfrac < 0.95$ $fltf < 1.6$
7. $\not{p}_T$-cut	$\not{p}_T > 20$ GeV

Table 7.2: Summary of the preselection cuts applied before feeding the MODT algorithm.

MC Events	Quality Cuts	Electron Cut	$\not{p}_T$-cut
$W \to \nu\tau$ (hadr.)	65.0%	61.7%	34.0%
Photoproduction	34.6%	34.1%	0.8%
NC DIS	53.4%	38.9%	0.0%
CC DIS	70.6%	70.2%	35.6%
τ pair	16.4%	14.8%	0.9%

Table 7.3: The number of events for the MC processes, which pass each cut. The cuts 1.-5. of Table 7.2 are called 'Quality Cuts'.

tion for the optimal set of observables should be especially tuned to discriminate τ jets from CC DIS jets.

7.4.2 Optimisation of the Separation

The aim of this section is to show, how the optimal set of jet observables is obtained. As mentioned in 7.4.1 the observables are chosen especially in order to discriminate τ jets from CC DIS jets, since this is the most relevant jet background after the preselection cuts. In principle one has to test each combination of all thirteen observables, but this would be much too time consuming. Hence, another strategy is applied:

As the initial set the observables $\{ntrk, rmean, lmean\}$ are used, since they are considered to be good quantities in measuring the multiplicity and the shape of jets. To investigate the separation potential of the remaining observables, all thirteen observables are plotted with an discriminant cut $D > 0.8$, which was calculated with the MODT algorithm using the three initial observables. If the three chosen observables are already the optimal set, all thirteen shape normalised observable distributions of the signal and the background events should be very similar. If one distribution is not, it is assumed that the corresponding observable has still potential to improve the separation. The statement above is valid only for a very high discriminant cut, typically at $D > 0.9$ or $D > 0.95$. But such a

high cut would lower the statistics of the background sample. A cut at $D > 0.8$ is found to be a good compromise.

Figure 7.13 shows the jet density distributions for the signal and the background MC's versus the thirteen jet observables including the additional requirement $D > 0.8$. The discriminant distribution shown in Fig. 7.13n was made without this cut. One can see that the separation power is already good. For a discriminant higher than 0.9 the separation power is ~ 26 at a signal efficiency of $\sim 34\%$. The high correlations between $ntrk$, $trkfrac$, $|charge|$ and $|chargeEW|$ discussed in section 7.3 are apparent from the plots 7.13a-d. The peaks at one in the distributions of $trkfrac$, $|charge|$ and $|chargeEW|$ are due to the dominance of one-track-jets. Thus the observables $trkfrac$, $|charge|$ and $|chargeEW|$ can be ignored in the further investigation, since they are directly connected to $ntrk$. The observables $lrms$ and $remc$ can also be eliminated for further survey, since their separation potential seems to be already limited as can be seen from 7.13h,j,k. $r90$ will also not be considered in the next iteration step, because this quantity is highly correlated to $rmean$, i.e. they represent two different definitions of basically the same observable. Taking $rmean$ instead of $r90$ for further investigations is an arbitrary choice. The relatively loose discriminant cut at 0.8 is the reason, why the $rmean$ distributions of the τ and the CC DIS MC's do not match very well, even though $rmean$ is one of the observables which was considered in the algorithm. But this fact is understandable, since τ jets are expected to be more collimated than CC DIS jets. $rmean$ seems to be a very good quantity to measure the collimation of jets, thus these distributions are still separated even after having processed them in the MODT algorithm. Hence, the remaining observables are $rrms$, $ncells$, $mass$ and $subj$, from which $mass$ seems to have the best potential to increase the separation power.

Thus, in the next step the observables $\{ntrk, rmean, lmean, mass\}$ are used as input to the MODT algorithm. Figure 7.14 shows the result. The separation has been improved significantly as one can see in 7.14n. The separation power increases to ~ 61 at an efficiency of $\sim 46\%$ for $D > 0.9$. From Fig. 7.14f it can be guessed that $rrms$ has still potential to increase the separation power, since the distributions of the τ MC and the CC DIS MC are still slightly separated, whereas $ncells$ is eliminated for further survey. Hence, in the next iteration step the set $\{ntrk, rmean, lmean, mass, rrms\}$ is used to calculate the discriminant. As can be seen from Fig. 7.15n one achieves a slight improvement. The separation power increases to ~ 83 at an efficiency of $\sim 48\%$ for $D > 0.9$.

Now, the last remaining observable is $subj$. After using the observables $\{ntrk, rmean, lmean, mass, rrms, subj\}$ the result is shown in Figure 7.16. Comparing diagrams 7.16n and 7.15n their seems to be no further improvement possible. However, as shown in Figure 7.17 one can see that a slight improvement of the separation power has been achieved. All plots in this figure show the efficiency ϵ and the separation power S as defined in chapter 6 as a function of the discriminant cut. The dots indicate the efficiency according to the scale on the left ordinate and the stars the separation power according to the scale on the right ordinate, respectively. The term '$[\geq]$' denotes that the event is required to have

at least one jet with the highest jet discriminant greater than or equal the x-value. Diagram 7.17a shows the whole discriminant range from 0 to 1, whereas diagram 7.17b shows an expanded region, when the observables $\{ntrk,\ rmean,\ lmean,\ mass,\ rrms\}$ are used. Diagram 7.17c and 7.17d shows the same quantities, when using the observables $\{ntrk,\ rmean,\ lmean,\ mass,\ rrms,\ subj\}$. The MODT algorithm using the additional observable $subj$ leads to a slightly better separation of τ jets from CC DIS jets without a loss of efficiency. The separation power increases to 92 at an efficiency of 48% for $D > 0.9$.

Since none of the thirteen observables are left for further investigation, the optimisation process ends here. The conclusion is that the six observables $\{ntrk,\ rmean,\ lmean,\ mass,\ rrms,\ subj\}$ form a reasonable set of observables out of the thirteen observables considered in the beginning in order to discriminate τ jets from CC DIS jets. For a discriminant cut of $D > 0.9$ the separation power is found to be 92 at an efficiency of 48%.

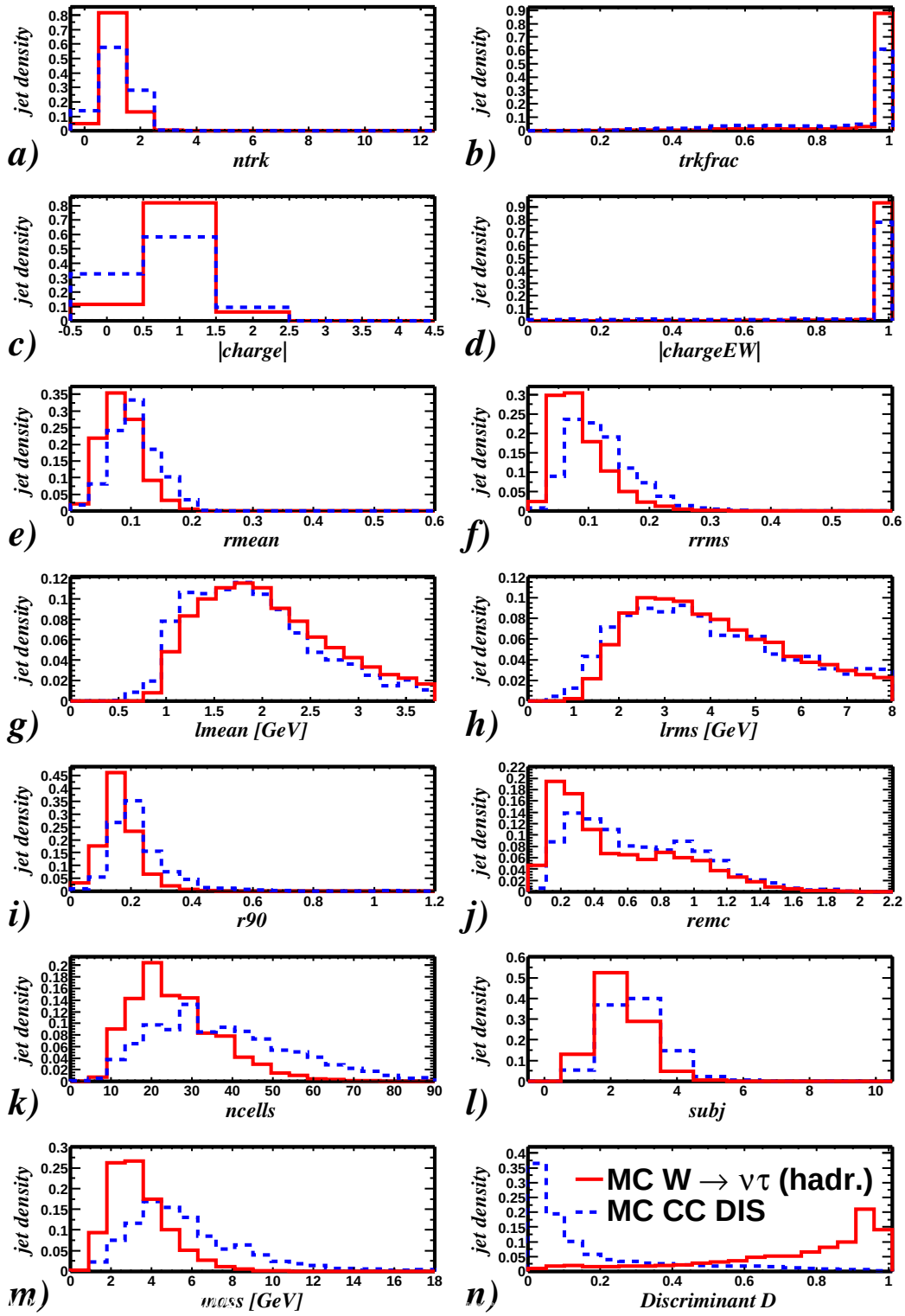

Figure 7.13: Distributions of the shape normalised number of jets vs. the thirteen jet observables and the discriminant, which was calculated by using the initial set of observables $\{ntrk, rmean, lmean\}$. The observable shown in (a)-(m) contain only the jets which have an discriminant higher than 0.8.

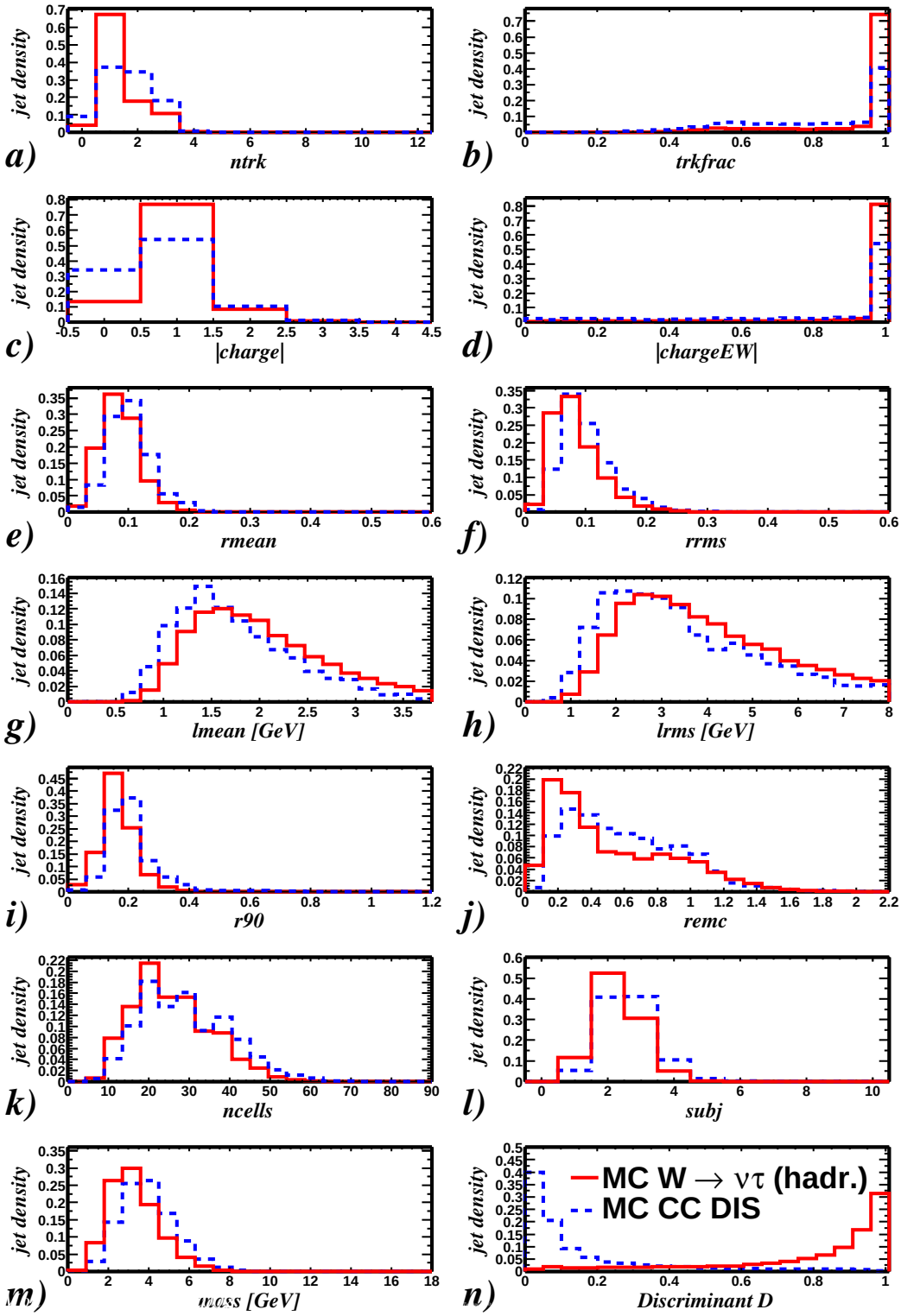

Figure 7.14: Distributions of the shape normalised number of jets vs. the thirteen jet observables and the discriminant, which was calculated by using the set of observables $\{ntrk,\ rmean,\ lmean,\ mass\}$. The observable shown in (a)-(m) contain only the jets which have an discriminant higher than 0.8.

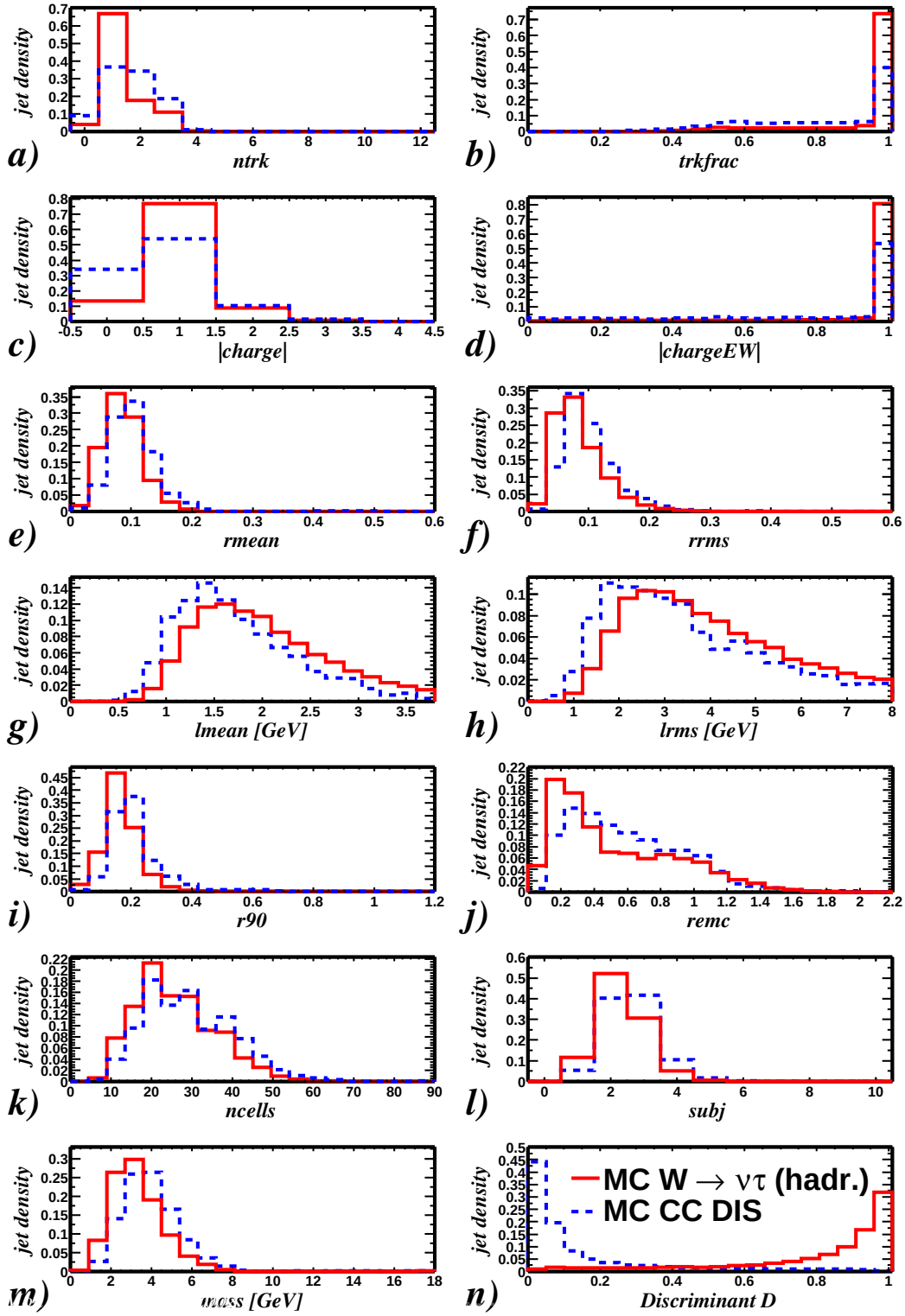

Figure 7.15: Distributions of the shape normalised number of jets vs. the thirteen jet observables and the discriminant, which was calculated by using the set of observables $\{ntrk, rmean, lmean, mass, rrms\}$. The observable shown in (a)-(m) contain only the jets which have an discriminant higher than 0.8.

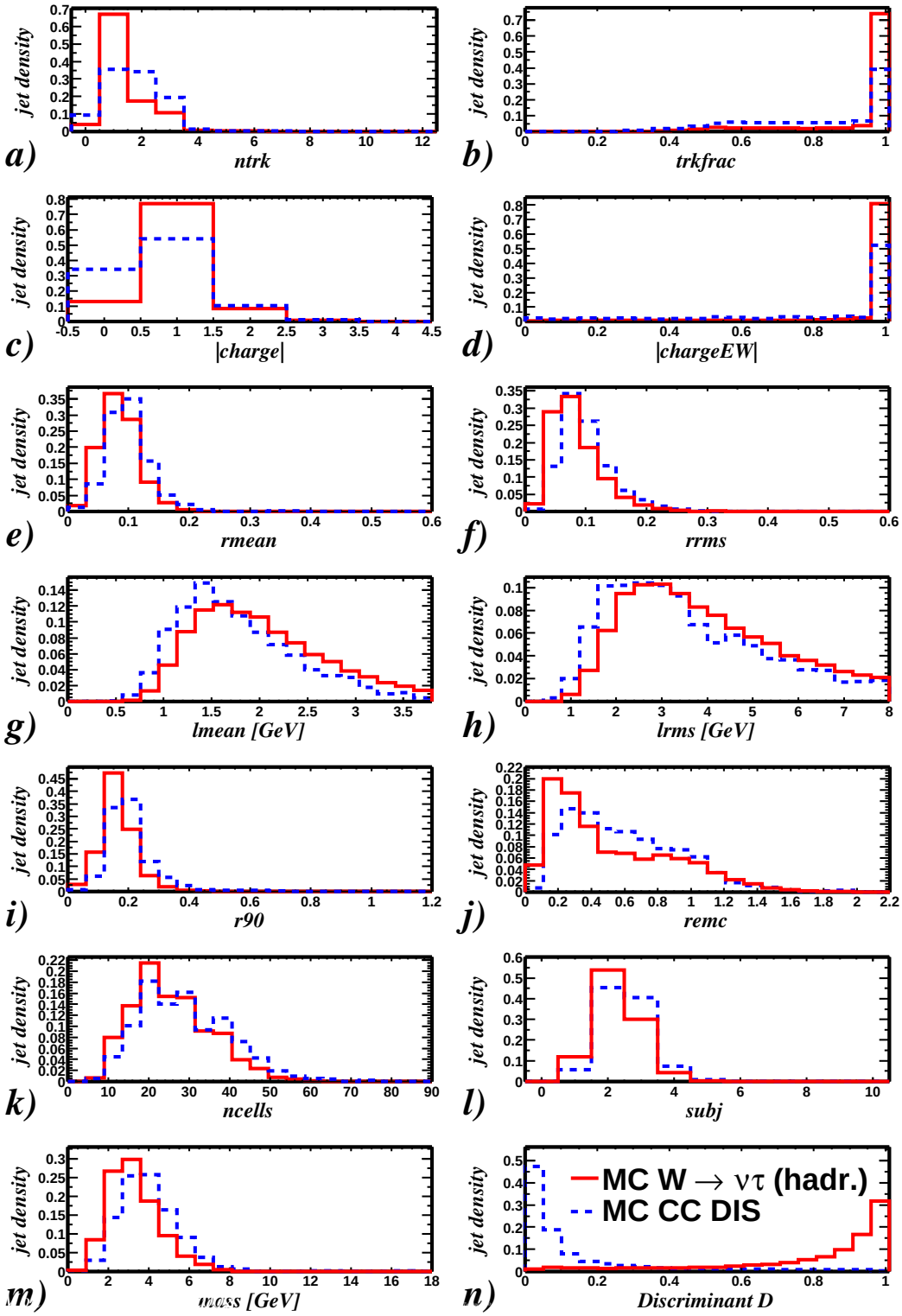

Figure 7.16: Distributions of the shape normalised number of jets vs. the thirteen jet observables and the discriminant, which was calculated by using the set of observables $\{ntrk, rmean, lmean, mass, rrms, subj\}$. The observable shown in (a)-(m) contain only the jets which have an discriminant higher than 0.8.

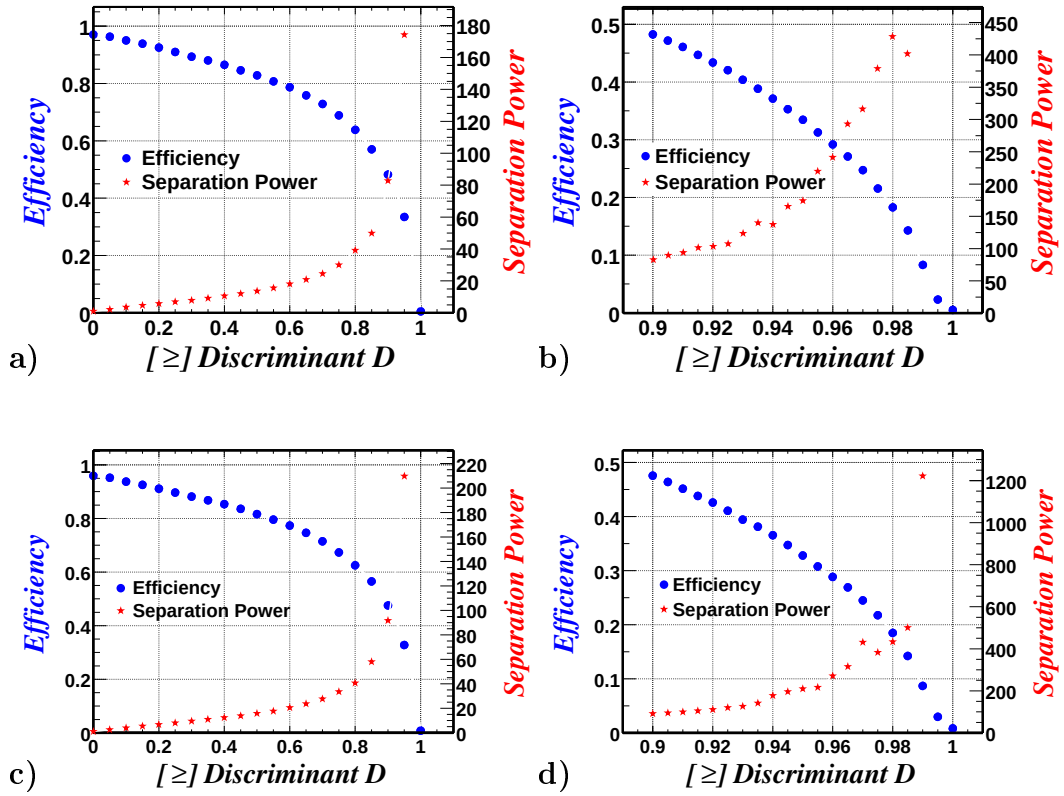

Figure 7.17: Efficiency and separation power as a function of the discriminant cut. The dots indicate the efficiency according to the scale on the left ordinate and the stars the separation power according to the scale on the right ordinate, respectively. The term '[≥]' denotes that the event is required to have at least one jet with the highest jet discriminant greater than or equal the x-value. (a) shows the whole discriminant range from 0 to 1, whereas (b) shows an expanded region, when the observables $\{ntrk,\ rmean,\ lmean,\ mass,\ rrms\}$ are used. (c) and (d) show the analogous plots, when using the observables $\{ntrk,\ rmean,\ lmean,\ mass,\ rrms,\ subj\}$.

7.5 Results

The final set of observables, obtained in section 7.4.2, contains *ntrk*, *rmean*, *rrms*, *lmean*, *subj* and *mass* (see Fig. 7.18). As the reference signal and background sample the $W \to \nu\tau$ (hadr.) MC and the CC DIS MC events are used, respectively. The MODT algorithm was applied in order to classify each jet by the discriminant. The result can be seen on Figure 7.19, where the shape normalised number of jets in each discriminant bin for the CC DIS MC and the τ MC are shown. One can see that a good separation of τ jets and CC DIS jets is obtained.

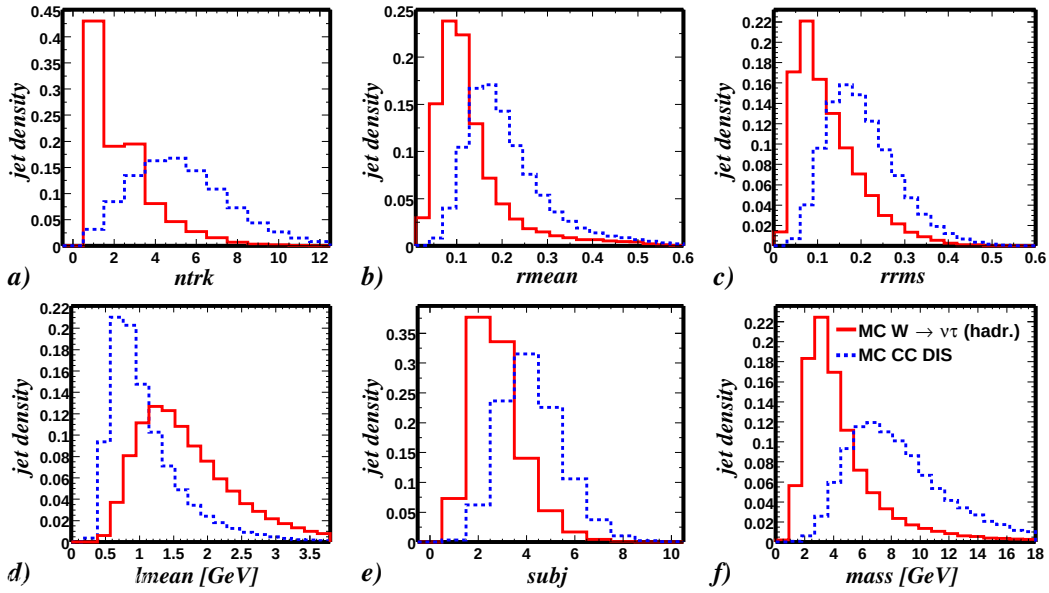

Figure 7.18: The shape normalised distributions of final observable set: The solid line indcates the τ MC sample and the dashed line the CC DIS MC sample.

The efficiency ϵ and separation power S, which are measuring the quality of the separation method, are presented in Figure 7.20. The rejection R can easily obtained by: $R = \frac{S}{\epsilon}$. For example, to get an efficiency of about 33 per cent the cut $D > 0.95$ has to be applied. With this cut one obtains a separation power of ca. 211, which corresponds to a rejection of 639. Note that the efficiency given here is calculated with respect to the number of events, which passed the preselection cuts. This number is defined as 100%. Since a high number of MC events is used, the statistical errors are expected to be small compared to the systematic error due to the different models to calculate the cross sections. Systematic errors have not been estimated in this analysis, because of lack of time.

Compared with an analysis made with single τ MC events published in [31, 32], where the achieved signal efficiency, separation power and background rejection are $\epsilon = 63\%$, $S = 11$, $R = 18$, this analysis has improved the separation of τ jets from QCD jets. In [31, 32] subsequently cuts on the observables *mass*, *ntrk*, *r90* and *ncells* are applied. For the rejection of electrons also the cuts $emfrac < 0.95$

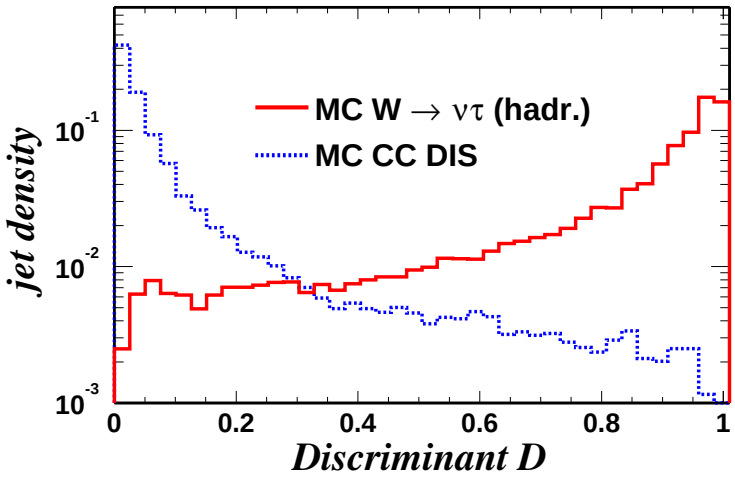

Figure 7.19: The shape normalised number of jets per discriminant bin for the CC DIS MC (hashed line) and the τ MC (solid line) for the observables $\{ntrk$, $rmean$, $lmean$, $mass$, $rrms$, $subj\}$.

and $fltf < 1.6$ are applied. If a similar efficiency of $\epsilon = 62\%$ is chosen for this analysis, which corresponds to a discriminant cut at $D = 0.8$, the separation power becomes $S = 40$ corresponding to a rejection of $R = 65$. This corresponds to an improvement of the background rejection of more than a factor three at a similar signal efficiency. In addition, the discriminant method as presented in this analysis provides the useful ϵ-S diagrams, which are a powerful tool to find the appropriate efficiencies and separation powers for any analysis.

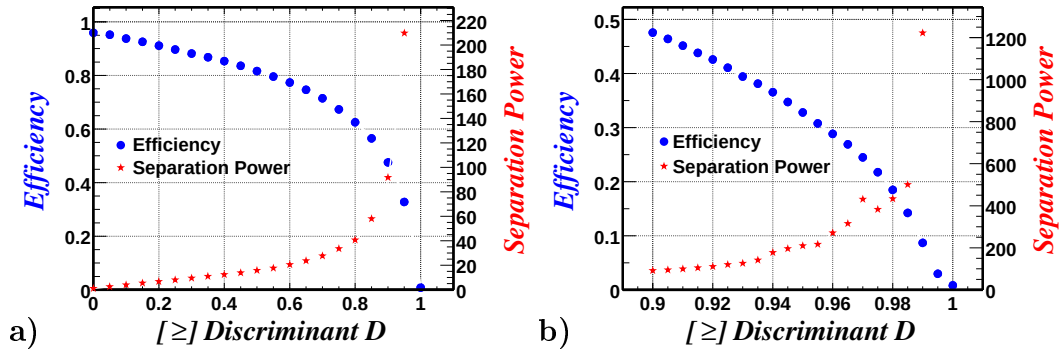

Figure 7.20: Efficiency and separation power as a function of the discriminant cut. The dots indicate the efficiency according to the scale on the left ordinate and the stars the separation power according to the scale on the right ordinate, respectively. The term '[≥]' denotes that the event is required to have at least one jet with the highest jet discriminant greater than or equal the x-value. (a) shows the whole discriminant range from 0 to 1, whereas (b) shows an expanded region.

Chapter 8

Data Analysis - 1999-2000 e^+p

Single $W^{\pm}$ boson events with subsequent $W \to \nu\tau$ decay, where the τ lepton decays hadronically, have been searched in the ZEUS data taken in the years 1999-2000 (e^+p), which corresponds to an integrated luminosity of $\mathcal{L} = 65.5$ pb^{-1}. This chapter describes how CC DIS events are selected from the data, without rejecting too many single $W^{\pm}$ boson production events, and how the remaining backgrounds from photoproduction, NC DIS, τ pair production and non-ep-processes are removed. The remaining events are expected to orginate from CC DIS or single $W^{\pm}$ boson production. In this data set τ decays are identified by using the MODT algorithm. In the last step the final cuts are applied and the results are presented.

8.1 Definition of Global Event Variables

The total energy of the event E is defined as the sum of all energy deposits in the calorimeter cells fulfilling a certain threshold. The energy of EMC cells are required to exceed 100 MeV, while those from the HAC1 and HAC2 are required to be above 150 MeV [1]:

$$E = \sum_i E_i \tag{8.1}$$

The transverse energy is obtained by:

$$E_T = \sum_i E_{T,i} = \sum_i E_i \cdot \sin\theta_i \tag{8.2}$$

The missing transverse momentum $\not{p}_T$ is obtained by:

$$\not{p}_T \equiv p_T^{cal} = \sqrt{(\sum_i E_i \sin\phi_i \sin\theta_i)^2 + (\sum_i E_i \cos\phi_i \sin\theta_i)^2} = \sqrt{p_x^{cal\ 2} + p_y^{cal\ 2}} \tag{8.3}$$

The total energy minus the longitudinal component of the total momentum vector $E - p_z$ is defined as

$$E - p_z = \sum_i E_i(1 - \cos\theta_i). \tag{8.4}$$

[1] In the following the index i refers to the cells in the calorimeter.

The transverse mass is defined as

$$M_T = \sqrt{2p_T^\ell p_T^\nu (1 - cos\phi^{\ell\nu})}, \tag{8.5}$$

where p_T^ℓ is the transverse momentum of the measured lepton and $\phi^{\ell\nu}$ is the azimuthal angle between the momentum vectors of the lepton and the neutrino, respectively, and p_T^ν is the transverse momentum of the neutrino. Since the neutrino is escaping undetected, its transverse momentum can be identified with the missing transverse momentum: $p_T^\nu \equiv \not{p}_T$. ϕ_{acop} is the acoplanarity angle, which is defined as the azimuthal separation of the outgoing lepton and the vector in the $\{x, y\}$-plane that balances the hadronic transverse momentum vector.
The transverse hadronic momentum is defined as

$$p_T^{had} = \sqrt{(p_x^{cal} - p_x^\ell)^2 + (p_y^{cal} - p_y^\ell)^2}. \tag{8.6}$$

The primary vertex can be calculated by extrapolating the reconstructed tracks to the beam axis. The number of hit superlayers is required to be at least three for a track fitted to the event vertex.

8.2 Event Selection

8.2.1 Trigger

The ZEUS trigger and data aquisition system store the results of a preclassification of the events in the so called data summary tapes (DST) bits, which can be considered as a pseudo fourth level trigger bit. These bits allow a fast access to predefined classes of events. The DST bit 34 (B34) is used to select CC DIS events from the data. B34 uses information from the SLT and TLT. In the following the indices FLT, SLT and TLT denote that a quantity was reconstructed at the first, second or third trigger level, whereas the indices $FCAL$, $BCAL$ and $RCAL$ indicate the different parts of the calorimeter.

SLT

The branch of the SLT, which aims to select CC events is called ExoSLT(4) and has the following logic:

$$(|t_G| < 7 \text{ ns }) \wedge \tag{8.7}$$

$$(((\not{p}_T^{SLT} > 6 \text{ GeV}) \wedge (\mathrm{E_T^{SLT}}(-2\mathrm{ir}) > 6 \text{ GeV}) \wedge (\mathrm{N_{trk}^{good,FLT}} \geq 1) \vee \tag{8.8}$$

$$((\not{p}_T^{SLT} > 9 \text{ GeV}) \wedge (\mathrm{E_T^{SLT}}(-1\mathrm{ir}) > 8 \text{ GeV}) \wedge (\mathrm{E_{FCAL}^{SLT}} > 20 \text{ GeV}))), \tag{8.9}$$

where t_G is the average calorimeter timing, which is first available at the SLT. The time-zero is calibrated to the electron-proton interaction time. The terms '$(-1ir)$' or '$(-2ir)$' indicate that the transverse energy is calculated excluding the innermost or the two innermost rings of FCAL, since the energies deposited in the very forward region are not sufficiently understood. $N_{trk}^{good,FLT}$ and $N_{trk}^{all,FLT}$ denote the number of good CTD tracks and the number all CTD tracks, respectively. For a good track at the FLT the projection of the trajectory in the CTD to the z-direction is required to point to the nominal interaction point.

TLT

The CC event selection at the TLT is performed by the branches ExoTLT(2) and ExoTLT(6). The logic for ExoTLT(2) can be expressed as follows:

$$(\not{p}_T^{FLT} > 6 \text{ GeV}) \wedge (\mathrm{N}_{\mathrm{trk}}^{\mathrm{good,TLT}} \geq 1) \wedge \tag{8.10}$$

$$(|z_{vtx}^{TLT}| < 60 \text{ cm}) \wedge (|\mathrm{t_u} - \mathrm{t_d}| < 8 \text{ ns}), \tag{8.11}$$

where z_{vtx}^{TLT} indicates the z-position of the CTD vertex. t_u and t_d are the timings measured in the upper and lower half of the calorimeter. Muons produced in atmospheric shower induced by cosmic radiation leave an earlier timing in the upper half of CAL than in the lower half ('earlyness'). They are removed by the timing cut.
The logic of ExoTLT(6) is:

$$\text{ExoSLT(4)} \wedge (|\mathrm{t_u} - \mathrm{t_d}| < 8 \text{ ns}) \wedge \tag{8.12}$$

$$(\not{p}_T^{TLT} > 6 \text{ GeV}) \wedge ((\mathrm{N}_{\mathrm{trk}}^{\mathrm{good,FLT}} \geq 1) \vee (\mathrm{E}_{\mathrm{FCAL}}^{\mathrm{TLT}} > 10 \text{ GeV})) \tag{8.13}$$

DST B34

The DST B34 is set, if the following requirements are fulfilled:

1. ExoTLT(2) $\vee$ ExoTLT(6) $\vee$ $p_T^{cal}(-1ir) > 6$ GeV
2. $p_T^{cal} > 7$ GeV
3. Events which satisfy all following 8 conditions are vetoed mainly in order to reject beam gas reactions:
   (a) $\neg$ ExoTLT(2)
   (b) $p_T^{cal}(-1ir) < 10$ GeV
   (c) $p_T^{cal} < 25$ GeV
   (d) $p_T^{cal}/E_T < 0.7$ GeV
   (e) $E - p_z < 10$ GeV
   (f) $p_T^{cal}/p_z^{cal} < 0.8$ GeV
   (g) $p_x^{cal} < 0$
   (h) $|p_x^{cal}| < 4$ GeV

In addition to the DST B34 cuts a strict transverse missing momentum cut of $\not{p}_T > 20$ GeV is applied in order to reject NC DIS and photoproduction backgrounds. The number of events obtained with all these requirements is 854 for the 1999 e^+p data and 1780 for the 2000 e^+p data.

8.2.2 Offline

This section describes the offline cuts made to reject non-ep processes such as halo muon events, cosmic muon events and beam gas reactions as well as ep processes such as NC DIS, photoproduction events and τ pair production. Most of the cuts have been developed in the standard ZEUS analysis to select CC DIS events. More detailed information about the performance of these cuts can be found in Ref. [33].

Beam gas reactions are induced by upstream reactions of electrons or protons with the residual gas nuclei or with beam pipe elements. Sometimes, e.g. if the measured vertex is shifted in such a way that the relation between energy and transverse energy is modified with respect to an event at the nominal interaction vertex, they can produce high E_T clusters.

Halo muons originate from the muonic decays of the hadronic products in the beam gas reactions. They produce a 'halo' moving in the direction of the proton beam. Halo muon events are charcacterized by energy deposits aligned in a narrow cylinder parallel to the beam pipe and not crossing the nominal interaction point.

High energy muons are also produced in cosmic showers in the atmosphere. They can traverse the detector and can leave traces at two diametrical located positions in the muon detector components without going through the nominal interaction point.

The HERA clock runs with a frequency of 10.4 MHz leading to potential electron-proton collsions every 96 ns. If non-ep processes as described above are randomly overlaid with ep processes, these events are not rejected at the trigger level.

Hadronic/Electromagnetic Fraction

To reject halo muon and cosmic muon events all events which fulfill the following requirements are vetoed:

$$E_{CAL}^{EMC}/E_{CAL} < 0.05, \tag{8.14}$$

$$E_{BCAL}^{HAC}/E_{BCAL} > 0.9, \text{ if } \mathrm{E_{BCAL}} > 5 \text{ GeV}, \tag{8.15}$$

$$E_{RCAL}^{HAC}/E_{RCAL} > 0.9, \text{ if } \mathrm{E_{RCAL}} > 5 \text{ GeV}, \tag{8.16}$$

where HAC denotes both hadronic type cells of the calorimeter ($HAC1$, $HAC2$) and EMC corresponds to the electromagnetic cells. RCAL and $BCAL$ indicate the rear and the barrel part of the calorimeter. CAL corresponds to all parts of the calorimeter. Halo muons often and cosmics sometimes fly parallel to the beam pipe, depositing a characteristic too high fraction in the electromagnetic or hadronic parts of the calorimeter. Cuts on the electromagnetic or hadronic fraction must be applied carefully. 170 events are cut off from the 1999 e^+p data and 287 events from the 2000 e^+p data.

Timing

Events which satisfy one of the following timing requirements are vetoed in order to reject cosmic muon events:

$$t_{FCAL} > -99 \text{ ns} \wedge |\mathrm{t_{FCAL}}| > 5 \text{ ns, if } \mathrm{E_{FCAL}} > 4 \text{ GeV}, \quad (8.17)$$

$$t_{BCAL} > -99 \text{ ns} \wedge |\mathrm{t_{BCAL}}| > 5 \text{ ns, if } \mathrm{E_{BCAL}} > 4 \text{ GeV}, \quad (8.18)$$

$$t_{RCAL} > -99 \text{ ns} \wedge |\mathrm{t_{RCAL}}| > 5 \text{ ns, if } \mathrm{E_{RCAL}} > 4 \text{ GeV}, \quad (8.19)$$

$$t_{FCAL} > -99 \text{ ns} \wedge \mathrm{t_{RCAL}} > -99 \text{ ns} \wedge |\mathrm{t_{FCAL-RCAL}}| > 6 \text{ ns, if } \mathrm{E_{CAL}} > 5 \text{ GeV}, \quad (8.20)$$

$$t_u > -99 \text{ ns} \wedge \mathrm{t_d} > -99 \text{ ns} \wedge |\mathrm{t_u} - \mathrm{t_d}| > 6 \text{ ns, if } \mathrm{E_{CAL}} > 5 \text{ GeV}, \quad (8.21)$$

where t_X corresponds to the duration between the time when an ep interaction at the nominal interaction point has occurred and the time, when a particle hits the part X of the calorimeter. $t_u - t_d$ and $t_{FCAL-RCAL}$ are the durations between a hit in the upper and the lower half of CAL and the time between a hit in the FCAL and the RCAL, respectively. These cuts are made to reject too early or too late cosmic events with respect to the nominal ep collision time. They remove 150 events from the 1999 e^+p data and 269 events from the 2000 e^+p data.

Track Counting

For beam gas rejection a cut on the number of 'good' tracks N_{trk}^{good} is performed, which is defined as the number of tracks with polar angles between $15^\circ < \theta^{trk} < 164^\circ$ and transverse momenta $p_T^{trk} > 0.2$ GeV. The requirement is:

$$N_{trk}^{good} > 0.2 \cdot (N_{trk}^{all} - 20). \quad (8.22)$$

A beam gas event tends to contain many tracks, but only a few of them are assigned to the primary vertex. This cut removes 132 events from the 1999 e^+p data and 405 events from the 2000 e^+p data.

Opening Angle of Cosmic Muon Tracks

For events with exactly two tracks fitted to the primary vertex, a cut on the opening angle between the two tracks is made.

$$\Delta\Omega\{\vec{\mathbf{p}}_{\mathbf{trk1}}, \vec{\mathbf{p}}_{\mathbf{trk2}}\} < 178^\circ, \text{ if } |\vec{\mathbf{p}}_{\mathbf{trk1}}|, \ |\vec{\mathbf{p}}_{\mathbf{trk2}}| > 200 \text{ MeV}, \quad (8.23)$$

with $\cos\Delta\Omega\{\vec{\mathbf{p}}_{\mathbf{trk1}}, \vec{\mathbf{p}}_{\mathbf{trk2}}\} = \frac{\vec{\mathbf{p}}_{\mathbf{trk1}} \cdot \vec{\mathbf{p}}_{\mathbf{trk2}}}{|\vec{\mathbf{p}}_{\mathbf{trk1}}| \cdot |\vec{\mathbf{p}}_{\mathbf{trk2}}|}$, where $|\vec{\mathbf{p}}_{\mathbf{trk1}}|$ and $|\vec{\mathbf{p}}_{\mathbf{trk2}}|$ are the reconstructed momentum vectors of the CTD tracks. This cut rejects cosmics. Only 7 and 5 events from the 1999 e^+p and the 2000 e^+p data, respectively, are rejected by this cut.

Crack Holes

Calorimeter cells, where both photomultipliers are not functioning, are called crack holes. NC DIS events where a high p_T electron hits such a crack can fake a CC DIS event. If one high-p_T track with $p_T^{trk} > 3$ GeV points into such a crack the event is rejected. This cut removes 20 events from the 1999 e^+p data and 11 events from the 2000 e^+p data.

Electron Acoplanarity

In NC DIS events the hadronic momentum is balanced by the electron momentum, hence the acoplanarity angle ϕ_{acop} between the vector, which balances the hadronic momentum vector and the electron momentum vector is expected to be zero. In order to reject NC DIS events, a cut on the acoplanarity angle ϕ_{acop} calculated for the highest p_T electron candidate and the hadronic momentum vector is applied:

$$\phi_{acop} < 0.2 \text{ rad, if } \mathrm{p_T^e} > 1 \text{ GeV}, \tag{8.24}$$

where p_T^e is the transverse momentum of the electron. For the identification of electrons the SINISTRA electron finder [34] is used, which is based on an artificial neutral network exploiting shower shape variables. The SINISTRA electron probability is required to be higher than 95%. Only one event from the 1999 e^+p and one event from the 2000 e^+p data is removed by this cut.

Muon Scan

Many cosmic muon events and halo muon events, which were not rejected by appropiate background rejection cuts, can be identified by a visual scan. Halo muon events are charcacterised by a trace of energy deposits in the calorimeter parallel to the beam pipe, indicating that they do not originate from the nominal interaction point. High energetic cosmic muons usually fly completely through the detector leaving traces at two diametrical located positions in the muon detector components. Additionally the interpolation of this trace is distinctly not going through the nominal interaction point. Eleven remaining cosmics and halo muons were found in about 360 visually scanned events from the 1999 e^+p data and the 2000 e^+p data.

Quality, Electron Rejection and $E - p_z$ Cuts

The quality and the electron rejection cuts used in section 7.4.1 as preselection cuts to ensure the quality of the measured jets and tracks and to reject electrons are also used for the data. For ep collsions with electron energies of 27.5 GeV and proton energies of 920 GeV and all particles detected and well measured, momentum conservation requires that the $E - p_z$ distribution peaks at $2E_e = 55$ GeV. For the 1999 e^+p data 91 and 14 events were rejected by the quality and the electron cuts, respectively. For the 2000 e^+p data the number of cut events are 147 and 35, respectively. One and three events are rejected due to the $E - p_z < 70$ GeV cut.

$\not{\mathbf{p}}_\mathbf{T}/\mathbf{E_T}$

To reject NC DIS and photoproduction events the fraction of the missing transverse momentum over the total transverse energy in the calorimeter $\not{p}_T/E_T$ is

required to be greater than 0.5:

$$\not{p}_T/E_T > 0.5. \tag{8.25}$$

This cut has to be applied very carefully, since it can remove signal events. A detailed investigation of this cut can be found in Ref. [33]. This cut rejects 25 events from the 1999 e^+p data and 45 events from the 2000 e^+p data.

Summary

The number of removed events for the 1999-2000 data are summarized in Table 8.1. The number of events, which passed all selection cuts is 802, where 241 are from the 1999 e^+p data and 561 are from the 2000 e^+p data. The CC DIS MC and the $W \to \tau\nu$ MC are used to evaluate the efficiency of the cuts. The number and the corresponding percentage of events, which passed in the CC DIS MC and $W \to \tau\nu$ MC after applying all cuts subsequently are listed in Table 8.2. The timing and crack hole cuts were not applied for the MC simulations, since the timing and crack hole information was not available in the MC data. The visual cosmic and halo muon scan makes no sense for MC simulations. Note that for data the missing transverse momentum cut is already included in the ZEUS standard code, i.e. this cut is already included in the initial number of events in Table 8.1. The number of selected data events from 1999 e^+p and from 2000 e^+p are consistent with the luminosities of 19.7 pb^{-1} and 45.8 pb^{-1}, respectively.

	1999 e^+p	2000 e^+p	99-00 e^+p
Initial	854	1780	2634
HAC/EMC Fraction	684	1493	2177
Timing	534	1224	1807
Track Counting	402	819	1221
Track Opening Angle	395	814	1209
Cracks	384	803	1187
Electron Acopl.	383	802	1185
Muon Scan	372	791	1163
Quality Cuts	281	644	925
Electron Rejection	267	609	876
$\not{p}_T/E_T$	241	561	802
Final	241	561	802

Table 8.1: Summary of the number of events in the 1999 and 2000 e^+p data, which passed the different cuts.

	MC CC DIS	MC $W \to \nu\tau$
Initial	100%	100%
HAC/EMC Fraction	99.7%	98.7%
Track Counting	99.6%	98.6%
Track Opening Angle	99.6%	98.6%
Electron Acopl.	99.5%	98.3%
Quality Cuts	70.1%	62.3%
Electron Rejection	69.8%	59.1%
$\not\!\!p_T/E_T$	68.6%	56.5%
$\not\!\!p_T > 20$ GeV	33.9%	28.7%
Final	33.9%	28.7%

Table 8.2: Summary of the number and percentage of events in the CC DIS MC and $W \to \tau\nu$ MC events which passed the different cuts.

8.2.3 Comparison of Data and Monte Carlo Simulation

The main purpose of the selection scheme is to identify a sample of CC DIS events in the data.

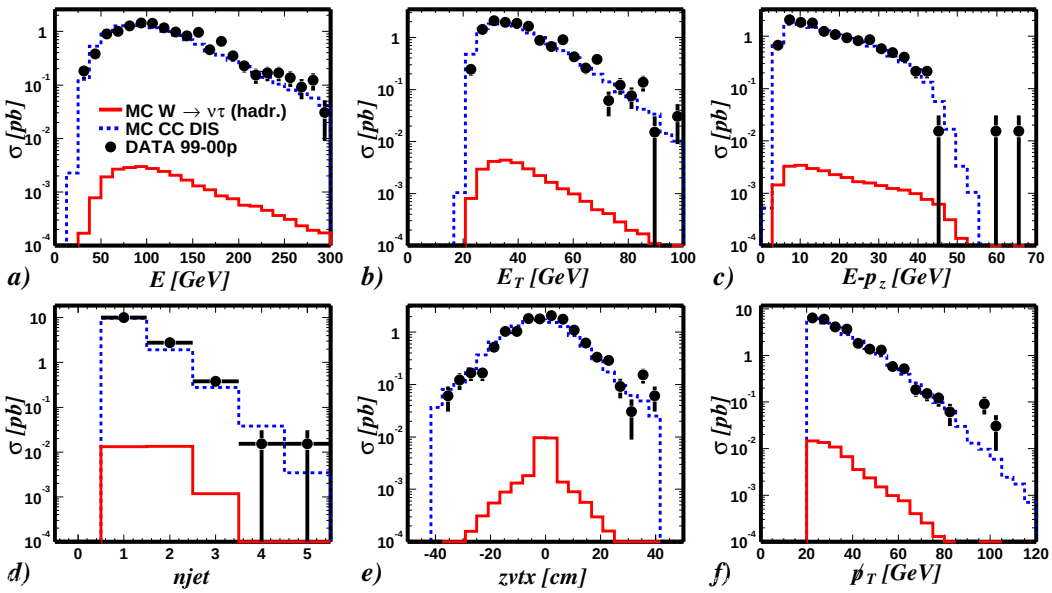

Figure 8.1: Distributions of the CC DIS MC, the $W \to \nu\tau$ MC and the 1999-2000 e^+p data after all selection cuts. Shown are the cross sections vs. the total energy (a), the transverse energy (b), $E - p_z$ (c), number of jets in the event (d), z-component of the vertex (e) and the missing transverse momentum (f). The excess in (f) at $\not\!\!p_T \approx 100$ GeV is not significant.

In this sample also single $W^{\pm}$ boson production events should be contained. The cuts should be chosen such that the efficiency is high for these events. Figures 8.1, 8.2 and 8.3 show the distributions of the CC DIS MC, the $W \to \nu\tau$ MC and

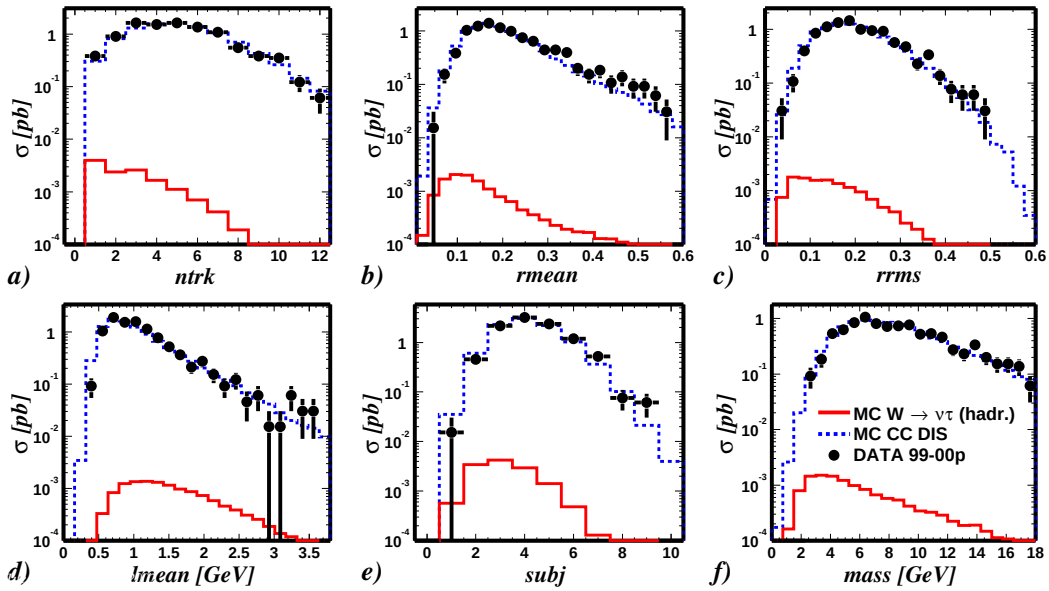

Figure 8.2: Distributions of the CC DIS MC, the $W \rightarrow \nu\tau$ MC and the 1999-2000 e^+p data after all selection cuts. Shown are the cross sections vs. the six jet observables $\{ntrk, rmean, rrms, lmean, subj, mass\}$.

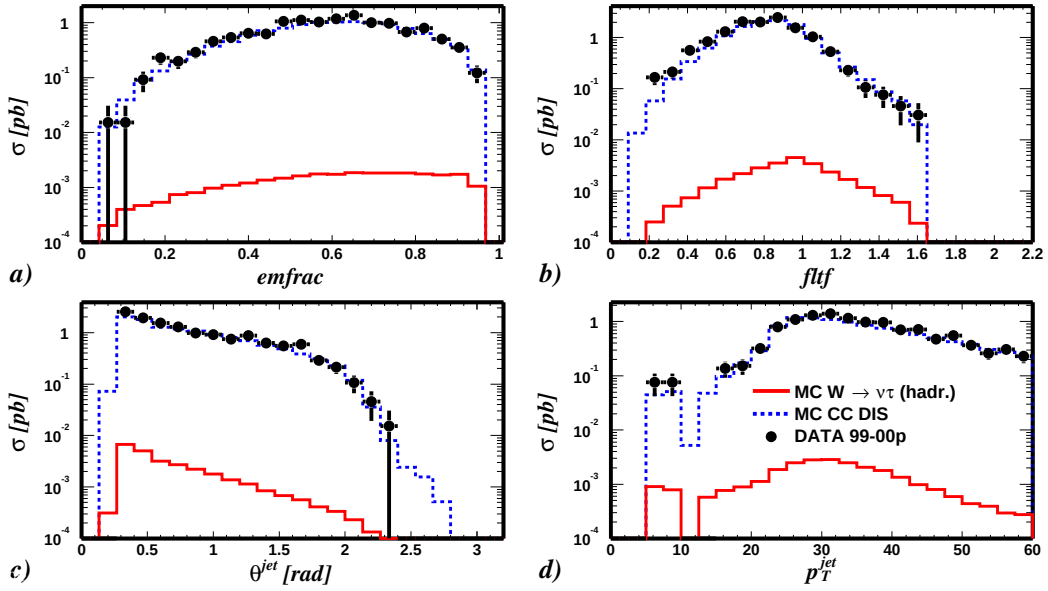

Figure 8.3: Distributions of the CC DIS MC, the $W \rightarrow \nu\tau$ MC and the 1999-2000 e^+p data after all selection cuts. Shown are the cross sections vs. the $emfrac$ (a), $fltf$ (b), jet polar angle (c) and jet transverse momentum (d).

the 1999-2000 e^+p data after all selection cuts. Since a relatively good agreement between the distributions of the CC DIS MC and the data is found, it can be concluded that the selected data samples mainly consists of CC DIS events. The cross section of single $W^{\pm}$ boson production is too small to draw conclusions. Despite the various cuts, in some corners of the phase space background events from ep and non-ep processes might still contribute.

8.3 Results

Figure 8.4 shows the discriminant distributions of the CC DIS MC, the $W \to \nu\tau$ MC and the 1999-2000 e^+p data after all selection cuts. Shown are the number of events containing at least one jet with the highest jet discriminant in the given bin. One can see that the distribution of the $W \to \nu\tau$ MC rise towards the one of CC DIS with growing discriminant. However, the separation power is still not high enough to be able to find a $W \to \nu\tau$ signal in the 1999-2000 e^+p data. The expected number of events, obtained from the MC calculation for an additional requirement of $D > 0.9$ for the highest discriminant jet in the event, is found to be:

D > 0.9

- $N_{CC}^{exp.} = 7.6 \pm 0.3$ (stat.)
- $N_{\tau}^{exp.} = 0.481 \pm 0.004$ (stat.)
- $N_{DATA}^{obs.} = 9$,

where $N_{CC}^{exp.}$ is the number of expected CC DIS events, $N_{\tau}^{exp.}$ is the number of expected $W \to \nu\tau$ events and $N_{DATA}^{obs.}$ the number of events found in the data.

Except for $0.1 < D < 0.25$ the CC DIS is able to describe the data. This might indicate some remaining NC DIS or photoproduction background events. Statistics of this type of background will be needed in future.

The diagrams in Figure 8.5 are plotted with the requirement that an event has to contain one jet with a jet discriminant greater than 0.9. A jet fulfiling this requirement is considered to be identified as a τ decay. These diagrams show the cross sections vs. the transverse energy of the identified τ jet (E_T^{τ}), the pseudorapidity of the τ jet (η^{τ}), the azimuthal angle of the τ jet (ϕ^{τ}), the transverse momentum of the hadronic system (p_T^{had}), the acoplanarity angle between the τ jet and the hadronic system (Φ_{acop}) and the transverse mass of the τ-lepton-neutrino system (M_T). The relatively loose requirement of $D > 0.9$ was chosen for these plots because of the low statistics of the data. The CC DIS MC gives a fair representation of the data. The Jacobian peak at 80 GeV, which is expected in the transverse mass distribution for W production events is visible, but smeared out by the detector resolution.

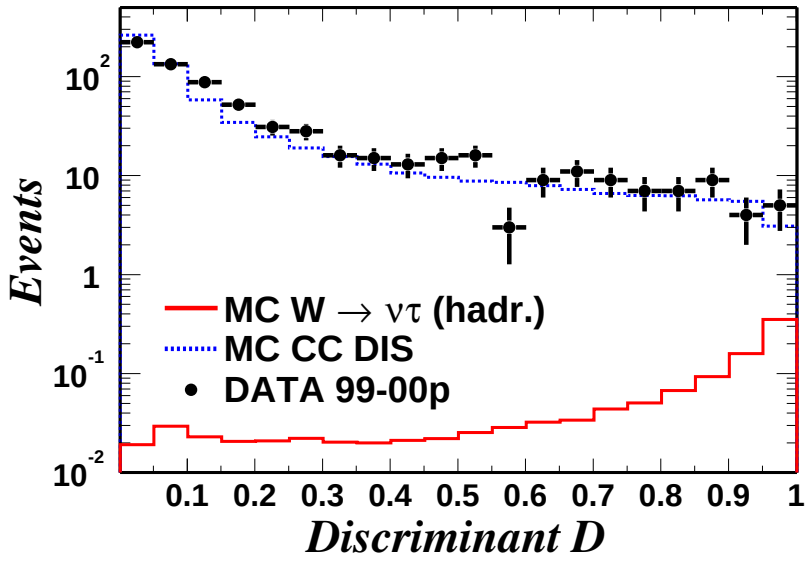

Figure 8.4: The number of events containing at least one jet with the highest jet discriminant in the given bin. The CC DIS MC is denoted by the dashed line, the $W \to \nu\tau$ MC is is denoted by the solid line and the data by the dots.

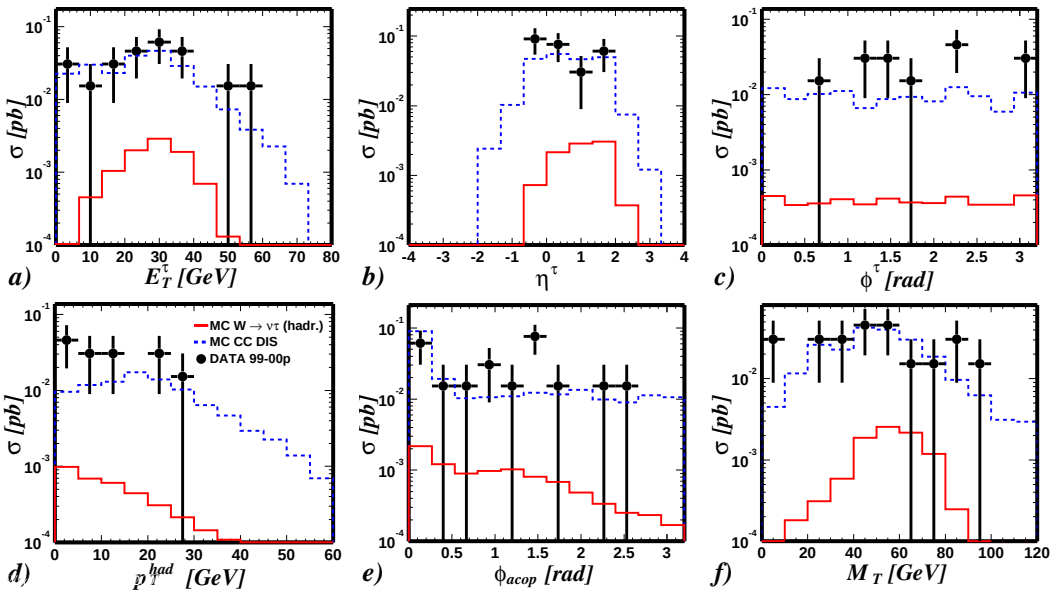

Figure 8.5: The cross sections vs. the transverse energy of the identified τ jet (a), the pseudorapidity of the τ jet (b), the azimuthal angle of the τ jet (c), the transverse momentum of the hadronic system (d), the acoplanarity angle between the τ jet and the hadronic system (e) and the transverse mass of the τ-lepton-neutrino system (f). A jet fulfilling the requirement $D > 0.9$ is considered to be identified as a τ jet.

8.3.1 Final Cuts

With a more strict requirement of $D > 0.95$ for the jet with the highest discriminant in the event, the expected number of events is found to be:

D > 0.95

- $N_{CC}^{exp.} = 2.33 \pm 0.16$ (stat.)
- $N_{\tau}^{exp.} = 0.317 \pm 0.004$ (stat.)
- $N_{DATA}^{obs.} = 5$,

These five events labeled as TAU-1 to TAU-5 are discussed in the following section in detail. The number of expected CC DIS events is much higher than the one for $W \to \tau\nu$ events, i.e. the five found events can not give any constraints to an observed signal. Nor do these five events represent an significant excess in the data, since the probability to find five or more events, if 2.65 background events are expected using Poisson statistics is 7.7%, i.e. not very unlikely.

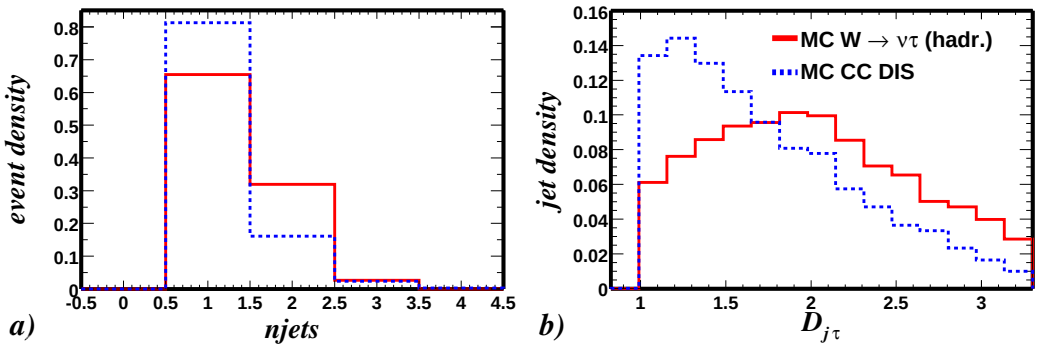

Figure 8.6: (a) The shape normalised number of events vs. the number of jets per event and (b) the shape normalised number of jets vs. the $\{\eta, \phi\}$-distance between the τ jet and the nearest jet ($D_{j\tau}$). The CC DIS MC is denoted by the dashed line, the $W \to \nu\tau$ MC is is denoted by the solid line.

As discussed in section 3.3, single $W^{\pm}$ boson production events more often than CC DIS events contain a second jet (compare with Fig. 8.6a). The second jet should be separated from the τ jet (compare with Fig. 8.6b, where the separation is shown in the $\{\eta, \phi\}$-plane). Therefore two additional requirements to reduce the background are discussed: The existence of a second jet or the existence of a second jet isolated from the τ jet.

For the discriminant plot in diagram 8.7a at least one second jet is required in addition to the requirements mentioned in section 8.2. One can see that the expected number of $W \to \nu\tau$ events approaches the number of CC DIS MC events at high discriminant values. For $D > 0.95$ the expected number of both types of MC events are nearly zero. However, three events were found in the data, identified as events TAU-1, TAU-2 and TAU-4. This excess in the data

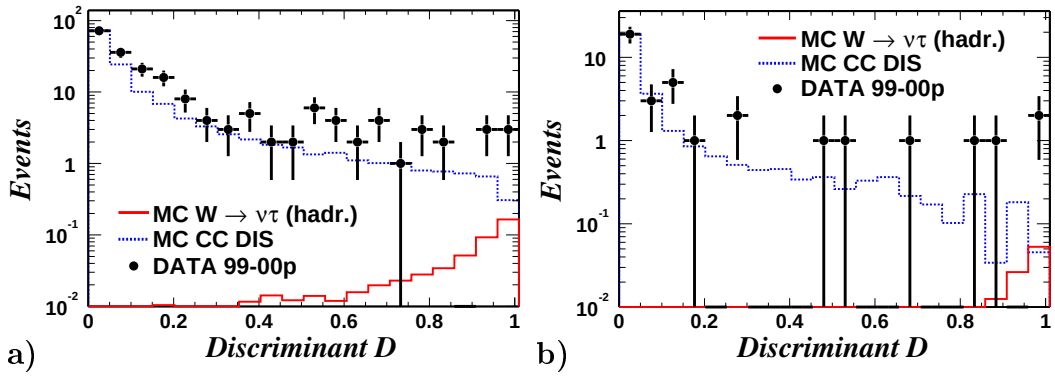

Figure 8.7: The number of events containing at least one jet with the highest jet discriminant in the given bin. The number of jets is required to be at least two (a) and additionally $D_{j\tau} > 1.8$ (b). The CC DIS MC is denoted by the dashed line, the $W \to \nu\tau$ MC is is denoted by the solid line and the data by the dots.

is consistent with SM predictions, since the probability to find three or more events, if 0.5 are expected is 1.26%. Although this is already unlikely, it could still be due to statistical fluctuation. Note that the CC DIS MC does not give a fair representation of the data anymore. E.g. for $0.05 < D < 0.3$, where no τ lepton contribution is expected, the data can not be described by the CC DIS MC. It is an open question, whether in this region the remaining NC DIS and photoproduction background could explain the excess found in the data. This might be also due to yet understood systematic errors, e.g. from the underlying fragmentation model.

D > 0.95, njets ≥ 2

- $N_{CC}^{exp.} = 0.32 \pm 0.06$ (stat.)
- $N_{\tau}^{exp.} = 0.175 \pm 0.003$ (stat.)
- $N_{DATA}^{obs.} = 3$

For diagram 8.7b the identified τ jet should additionally be isolated, i.e. the $\{\eta, \phi\}$-distance between the τ jet and the nearest jet is required to be greater than $D_{j\tau} > 1.8$ (compare with Fig. 8.6b). Only two events (TAU-1, TAU-2) satisfying these requirements were found in the data, while 0.11 ± 0.03 CC DIS and $W \to \nu\tau$ events are expected. The excess in the data has grown. The probabilty to find two or more events, if 0.1 are expected is 0.45%, calculated from Poisson statistics. This is a small probability, but could be still due to a statistical fluctuation.

D > 0.95, njets ≥ 2, $\mathbf{D_{j\tau} > 1.8}$

- $N_{CC}^{exp.} = 0.045 \pm 0.023$ (stat.)
- $N_{\tau}^{exp.} = 0.053 \pm 0.002$ (stat.)
- $N_{DATA}^{obs.} = 2$

Note that only statistical errors were calculated. Unfortunately there was no time left to make a detailed investigation of systematic errors. This might be a worthwhile task in the future, since they would allow a more reliable calculation of the probabilities in terms of the measurement errors. In addition, a more detailed investigation of the NC DIS and photoproduction background is needed.

8.3.2 Discussion of the Selected Events

In the following the five tau candidate events TAU-1 to TAU-5 selected in sections 8.3 with the cut $D > 0.95$ are discussed in detail. Figure 8.8 show their locations in the p_T^{had}-M_T and E_T^τ-$\not{p}_T$-plane, indicated by the filled triangles and the corresponding numbers. For comparison the $W \to \nu\tau$ MC distribution (dots) and the CC DIS MC distribution (open circles) in these planes are shown after all cuts, except $njets \geq 2$ and $D_{j\tau} > 1.8$. The two events TAU-1 and TAU-2, which passed all additional cuts in the section above ($D > 0.95$, $njets \geq 2$, $D_{j\tau} > 1.8$), have a striking topology, not unlike some of the muon events reported by H1.

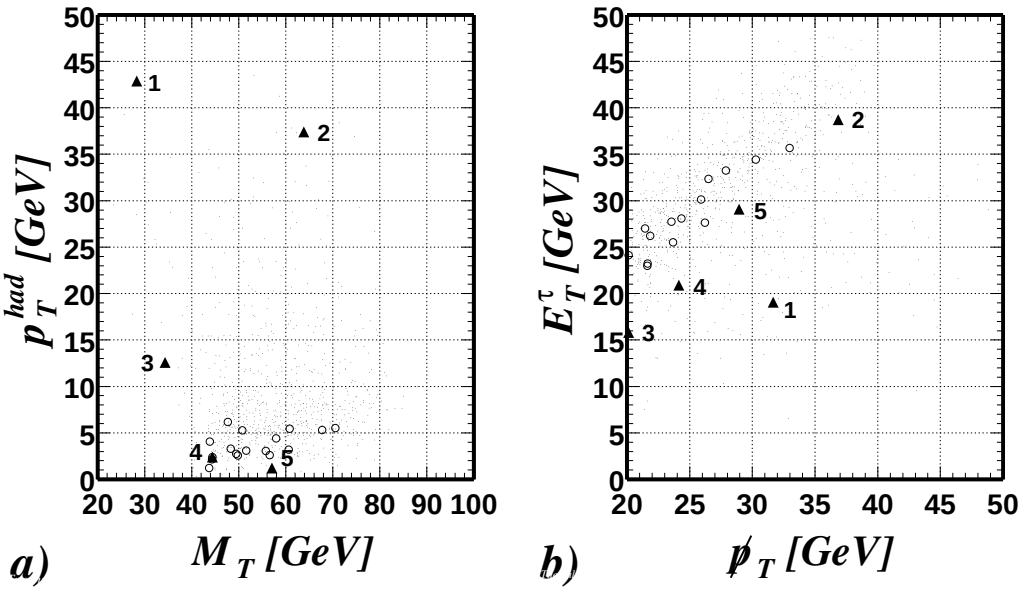

Figure 8.8: The distributions of the $W \to \nu\tau$ MC events (dots) corresponding to 500 fb^{-1} and of the CC DIS MC events (open circles) corresponding to 10 fb^{-1} in the (a) p_T^{had}-M_T-plane and in the (b) E_T^τ-$\not{p}_T$-plane after all selection cuts, except $njets \geq 2$ and $D_{j\tau} > 1.8$. The five selected τ events (TAU-1 to TAU-5) are indicated by the filled triangles and the corresponding numbers.

TAU-1

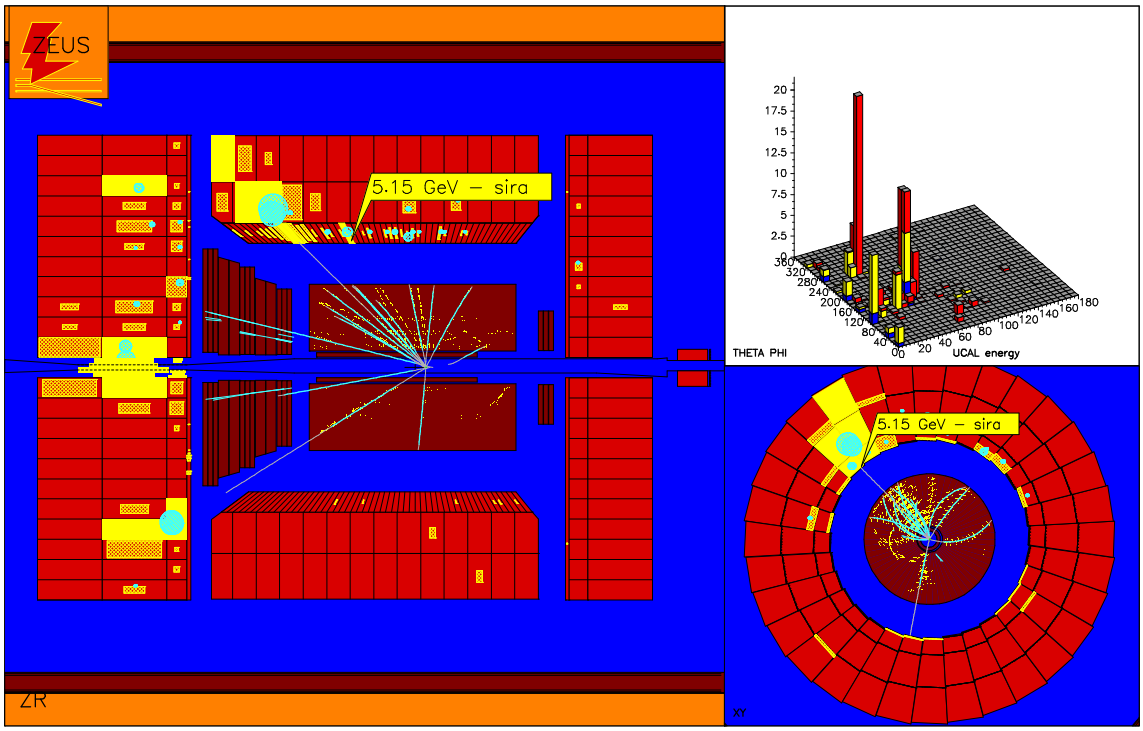

Run Nr.	Event Nr.	E [GeV]	E_T [GeV]	E – pz [GeV]
33358	19167	113.7	61.5	26.2

$\not{p}_T$ [GeV]	$\not{\phi}$ [deg]	zvtx [cm]	njets
31.7	328.0	-11.0	2

E_T^τ [GeV]	θ^τ[deg]	ϕ^τ [deg]	p_T^{had} [GeV]	ϕ_{acop} [deg]	M_T [GeV]
20.7	31.4	256.4	42.9	44.4	29.9

ntrk	rmean	rrms	lmean [GeV]	subj	mass [GeV]	D
1	0.133	0.044	1.87	2	1.36	0.965

E_T^e [GeV]	θ^e [deg]	ϕ^e [deg]	SIN95
4.65	59.4	132.9	0.978

Figure 8.9: First τ candidate event TAU-1 from the 1999 e^+p data.

Since this τ candidate event contains an hadronic system with a very high transverse momentum (42.9 GeV), it is not a typical $W \rightarrow \nu\tau$ candidate, but might be a good candidate for new phenomena. The τ jet lies in the FCAL, has a discriminant value of 0.965 and is isolated from the hadronic system, which is located in the upper BCAL, very near to an electron candidate of 5.15 GeV energy, identified by SINISTRA (SIN95) with a probability of 97.8%. This electron candidate could be produced in an electronic decay of a hadron - possibly of an electronic *bottom* decay, which might come from a top decay. This electron candidate has no primary track pointing to its cluster, which decreases the probability that this particle is an electron.

TAU-2

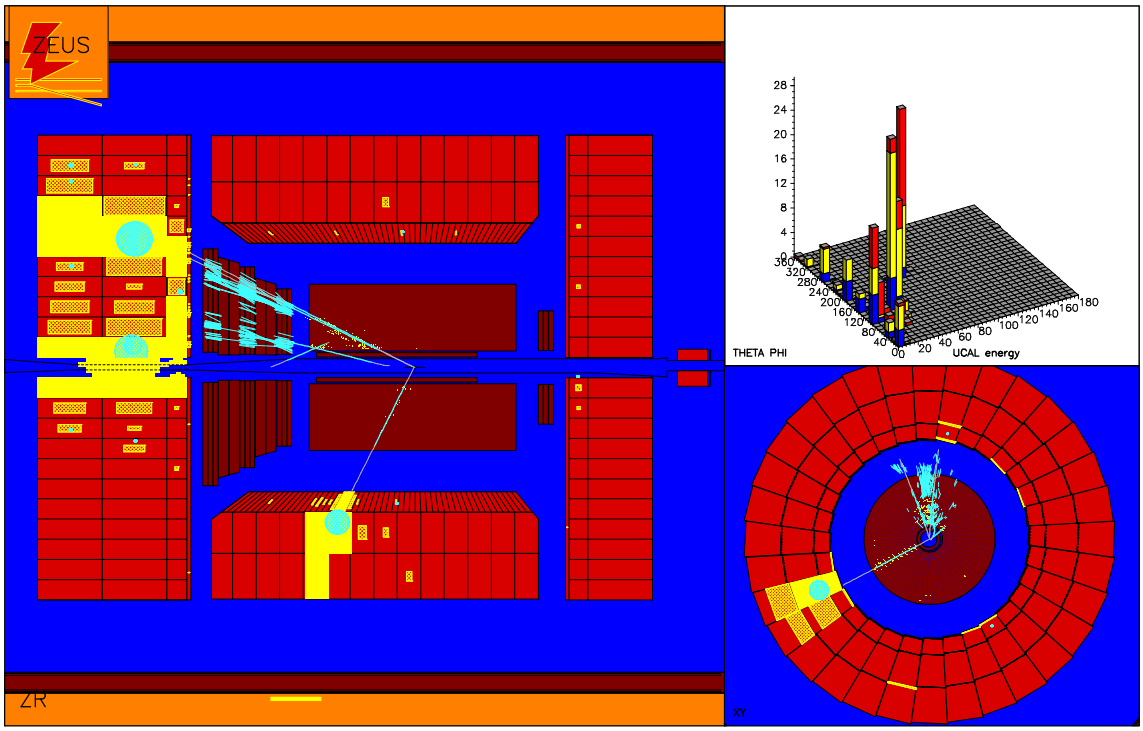

Run Nr.	Event Nr.	E [GeV]	E_T [GeV]	E − pz [GeV]
34169	5711	172.4	69.1	27.7

$\not{p}_T$ [GeV]	$\not{\phi}$ [deg]	zvtx [cm]	njets
36.9	328.3	1.0	3

E_T^τ [GeV]	θ^τ[deg]	ϕ^τ [deg]	p_T^{had} [GeV]	ϕ_{acop} [deg]	M_T [GeV]
38.3	63.5	204.8	35.6	59.8	66.2

ntrk	rmean	rrms	lmean [GeV]	subj	mass [GeV]	D
1	0.162	0.050	2.12	2	2.39	0.988

Figure 8.10: τ candidate event TAU-2 from the 1999 e^+p data.

This is the only event with more than two jets. Both non-τ-jets are lying in the FCAL and carry a tranverse momentum of 35.6 GeV, which is very high for a typical $W \to \nu\tau$ event. The isolated τ jet candidate is found in the lower half of BCAL and carries a tranverse momentum of 38.3 GeV. The value for the τ discriminant for this jet is 0.988. It is the second of the two events, which even passed the additional cuts: $D > 0.95$, $njets \geq 2$, $D_{j\tau} > 1.8$. Hence, this event might also be a candidate for new phenomena.

TAU-3

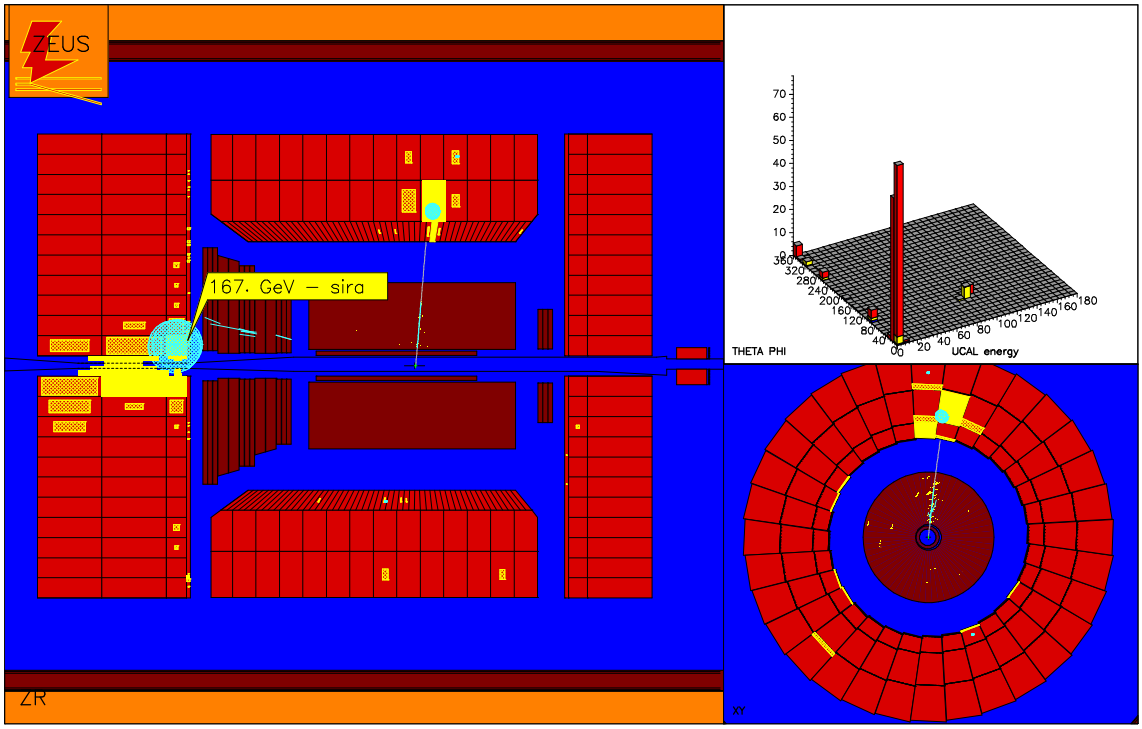

Run Nr.	Event Nr.	E [GeV]	E_T [GeV]	E – pz [GeV]
34287	20342	179.9	17.6	14.9

$\not{p}_T$ [GeV]	ϕ [deg]	zvtx [cm]	njets
20.9	226.7	-1.1	1

E_T^τ [GeV]	θ^τ [deg]	ϕ^τ [deg]	p_T^{had} [GeV]	ϕ_{acop} [deg]	M_T [GeV]
15.8	96.2	84.2	12.7	93.5	34.4

ntrk	rmean	rrms	lmean [GeV]	subj	mass [GeV]	D
1	0.166	0.049	1.14	2	1.6	0.977

E_T^e [GeV]	θ^e [deg]	ϕ^e [deg]	SIN95
18.5	6.4	11.1	0.989

Figure 8.11: τ candidate event TAU-3 from the 1999 e^+p data.

This event contains only one jet, which was identified as a τ jet with a discriminant value of 0.977. The transverse momentum of the hadronic system is $p_T^{had} = 12.7$ GeV and the transverse mass is 34.4 GeV. Since this are not very atypical quantities for $W \to \nu\tau$ events, this might be a good candidate for such kind of process.

TAU-4

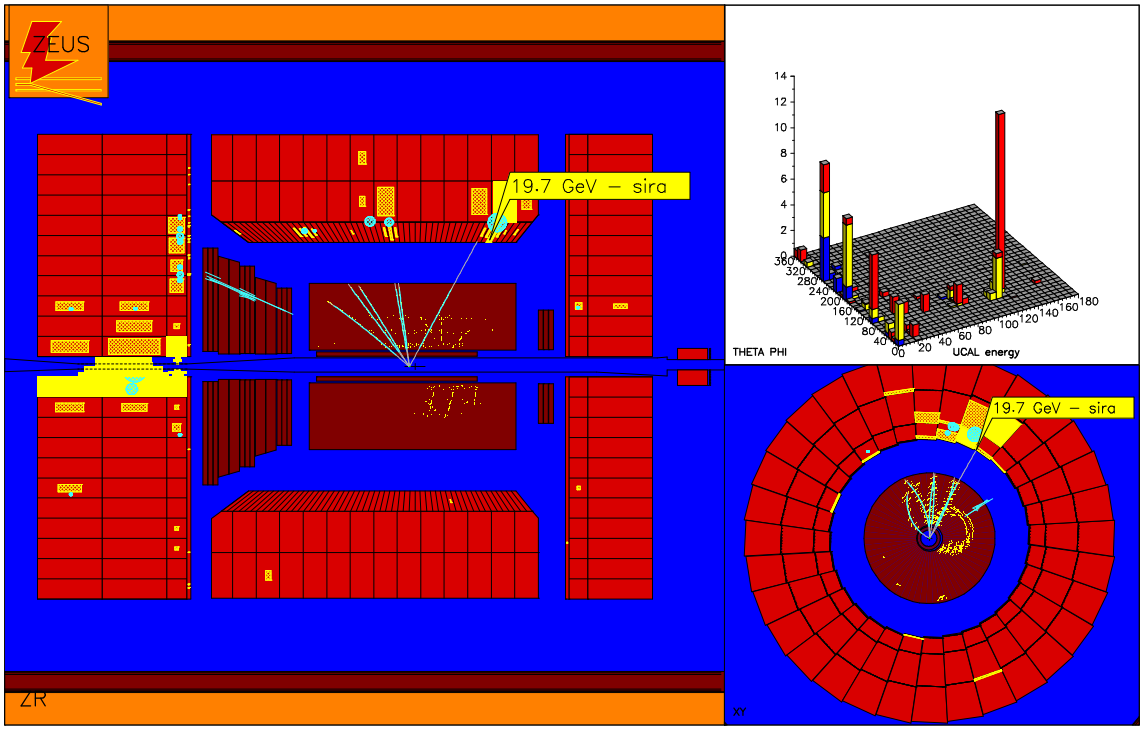

Run Nr.	Event Nr.	E [GeV]	E_T [GeV]	E – pz [GeV]
35081	43983	66.0	28.3	36.9

$\not{p}_T$ [GeV]	$\not{\phi}$ [deg]	zvtx [cm]	njets
23.8	250.9	5.6	2

E_T^τ [GeV]	θ^τ [deg]	ϕ^τ [deg]	p_T^{had} [GeV]	ϕ_{acop} [deg]	M_T [GeV]
21.5	121.3	66.6	2.9	141.6	45.2

ntrk	rmean	rrms	lmean [GeV]	subj	mass [GeV]	D
3	0.081	0.052	2.27	2	2.9	0.966

E_T^e [GeV]	θ^e [deg]	ϕ^e [deg]	SIN95
17.5	122.4	62.1	0.973

Figure 8.12: τ candidate event TAU-4 from the 2000 e^+p data.

In this event the same jet was identified either as a τ jet candidate ($D = 0.966$) and as an electron candidate by SINISTRA (97.3%). For this electron candidate a track with positive charge, which matches the jet could be found. The polar angle of this particle is rather high, but there is no indication of hadronic energy depositions back-to-back with respect to the direction of this particle. Thus, the probability for a NC DIS event is small. This event could represent a CC DIS event, where a produced hadron decays electronically. But it might also be a $W \to \nu\tau$ event, since it lies in phase space not untypical for such kind of events.

TAU-5

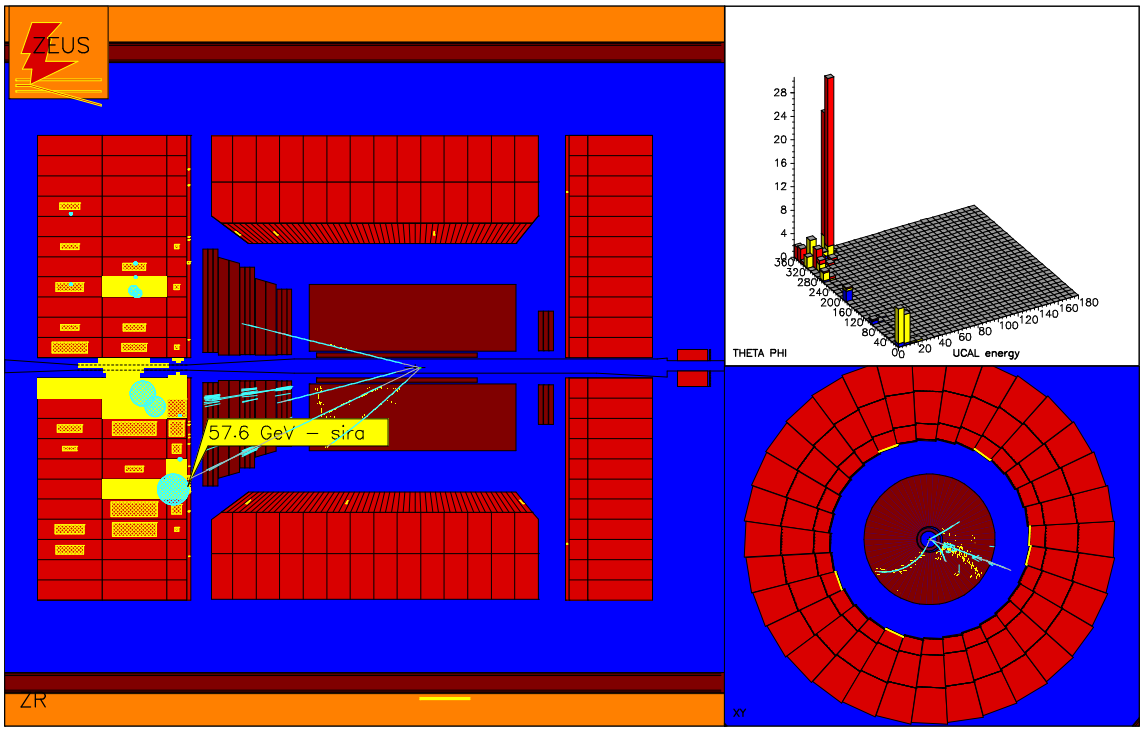

Run Nr.	Event Nr.	E [GeV]	E_T [GeV]	E – pz [GeV]
37543	5615	102.3	31.8	6.6

$\not{p}_T$ [GeV]	$\not{\phi}$ [deg]	zvtx [cm]	njets
29.9	160.0	-5.1	1

E_T^τ [GeV]	θ^τ [deg]	ϕ^τ [deg]	p_T^{had} [GeV]	ϕ_{acop} [deg]	M_T [GeV]
29.2	26.3	338.2	1.2	125.9	59.0

ntrk	rmean	rrms	lmean [GeV]	subj	mass [GeV]	D
1	0.089	0.049	2.13	2	2.5	0.987

Figure 8.13: τ candidate event TAU-5 from the 2000 e^+p data.

In this event the τ jet candidate ($D = 0.987$) is very near the beam pipe. Since it has no second jet and also the transverse momentum of the hadronic system is small (1.2 GeV), this event is more likely to be a CC DIS event than a $W \to \tau\nu$ event.

Summary

Five τ lepton candidate events were found, which fulfill the final cut $D > 0.95$. From these five events three have a second jet and two events contain a τ candidate, which is isolated. These two events seem to be most promising to represent processes, which are not described by the SM, since they contain a hadronic system with atypically high transverse momentum. The probability to find two events after all cuts is found to be 0.45%, which could still be due to a statistical fluctuation. Nevertheless, the two mentioned events possess very interesting topology properties and are worth to be discussed in the future. Unfortunately there was no time left to make a detailed investigation of systematic errors, which would allow a more reliable calculation of the probabilities. Hence, only statistical errors were calculated. In addition, a detailed investigation of the NC DIS and photoproduction background is needed.

Chapter 9

Summary

This thesis has presented a search for single $W^{\pm}$ boson production events with the subsequent decay $W \to \nu\tau$, where the τ lepton decays hadronically. The analysis is based on an e^+p data sample corresponding to an integrated luminosity of $\mathcal{L} = 65.5$ pb^{-1} collected in the years 1999 and 2000 with the ZEUS detector at HERA.

The major challenge was the separation of τ lepton induced jets from gluon and quark induced jets. For this purpose a multiobservable discrimination technique was applied, which combined six observables characterising the jet properties in a single quantity - called discriminant D. These six observables were selected after a detailed investigation of initially thirteen observables. For an efficiency of $\epsilon = 33\%$ a separation power of $S = 211$ has been achieved, which corresponds to a background rejection of $R = 639$. Compared to a published ZEUS analysis the separation power has been improved by a factor of at least three. For a signal efficiency of $\epsilon = 63\%$, a separation power of $S = 11$ has been achieved by the published analysis, which corresponds to a background rejection of $R = 18$. For a similar efficiency ($\epsilon = 62\%$) a separation power of $S = 40$ has been achieved by this analysis, which corresponds to a background rejection of $R = 65$. In addition the new discrimination technique allows to easily adjust the signal efficiency and the separation power to the need of any particular analysis.

The selection of the events is based on cuts which supress non-CC DIS events and which have a high efficiency for single $W^{\pm}$ boson production events. Three different final selection criteria were discussed. The first one requires $D > 0.95$ for the highest discriminant jet in the event. The number of events for this cut is found to be:

D > 0.95

- $N_{CC}^{exp.} = 2.33 \pm 0.16$ (stat.)
- $N_{\tau}^{exp.} = 0.317 \pm 0.004$ (stat.)
- $N_{DATA}^{obs.} = 5$,

According to Poisson statistics the probability to find five or more events, where 2.65 background events are expected, is 7.69%. If one requires in addition two

jets in an event the number of events are:

D > 0.95, njets ≥ 2

- $N_{CC}^{exp.} = 0.32 \pm 0.06$ (stat.)
- $N_{\tau}^{exp.} = 0.175 \pm 0.003$ (stat.)
- $N_{DATA}^{obs.} = 3$

The Poisson probability is found to be 1.26%. If the τ jet is required to be isolated ($D_{j\tau} > 1.8$) the result is:

D > 0.95, njets ≥ 2, $\mathbf{D_{j\tau} > 1.8}$

- $N_{CC}^{exp.} = 0.045 \pm 0.023$ (stat.)
- $N_{\tau}^{exp.} = 0.053 \pm 0.002$ (stat.)
- $N_{DATA}^{obs.} = 2$

These numbers correspond to a probability of 0.45% according to Poisson statistics. This probability is small, but it is not small enough that one can state to have found a significant excess in the data. However, the two remaining events have a topology which is very interesting and which is similar to the one of the events reported by the H1 collaboration. Both events contain a hadronic system with a very high transverse momentum p_T^{had}, which is atypical for $W \to \nu\tau$ events. One of these events might be a candidate for a single top event, since in one of the jets an electron candidate has been found which might indicate a semi-leptonic b-decay. Since the electron signature for this event is not clear enough (the cluster of the electron candidate has no track pointing to the primary vertex), it might also be a $W \to \nu\tau$ event with an atypically high p_T^{had}. Because the second event also contains an atypically high p_T^{had}, it is also a very promising candidate for new phenomena. Which kind of process is worth to be discussed in the future.

Unfortunately, there was not enough time left to investigate systematic errors, which might be a worthwhile task in the future in order to perform a more reliable calculation of the probabilities. Also more systematic investigations of remaining NC DIS and photoproduction events are needed.

Appendix A

Definition of Jets

This chapter gives the definition of jets used in this analysis. Jets are defined by algorithms, which identify clusters of energy deposits in the calorimeter. This analysis uses the inclusive k_T algorithm (KTCLUS), which is invariant under boosts along the z-direction, as described in [35]:

The algorithm is based on the transverse energy $E_{T,i}$, pseudorapidities η_i and azimuthal angles ϕ_i of the particles[1]. The jet transverse energy and position variables are defined by:

$$E_T^{jet} = \sum_i E_{T,i}, \quad \eta_{jet} = \frac{\sum_i E_{T,i}\eta_i}{\sum_i E_{T,i}}, \quad \phi_{jet} = \frac{\sum_i E_{T,i}\phi_i}{\sum_i E_{T,i}}, \tag{A.1}$$

where the sum runs over all particles associated with the jet.

A detailed description of the KTCLUS algorithm is given in the following:

1. Start with a list of particles and an empty list of jets.
2. For each particle i as well as for each pair of particles (i, j) the distances d_i and d_{ij} are calculated, where

   $$d_i = E_{T,i}^2 R_0^2 \text{ and } d_{ij} = \min(E_{T,i}^2, E_{T,j}^2), \text{ with } R_{ij}^2 = \Delta\eta_{ij}^2 + \Delta\phi_{ij}^2 \tag{A.2}$$

   The free parameter R_0 is set to $R_0 = 1.0$.
3. The smallest value of all the d_i and d_{ij} is labelled d_{min}.
4. If d_{min} belongs to the set of d_{ij}, the particles i and j are merged into a new particle using the recombination prescription in Eq. (A.1) and removed from the list of particles.
5. If d_{min} belongs to the set of d_i, the particle i is removed from the list of particles and added to the list of jets.
6. When no particles are left (i.e. all particles are included in jets) the procedure is finished.

In addition usually a cut on the transverse jet energy is applied to select hard jets. The algorithm can in the same way be applied on simulated particles.

[1] In this section a hit calorimeter cell (above the threshold) will be identified as a particle: hit cell $\equiv$ particle. The index i runs over all particles.

Appendix B

Separation of τ Jets from QCD Jets

In sections 7.4 and 7.5 it has been shown that the MODT algorithm gives a good separation of jets induced by τ leptons from CC DIS jets. The preselection was tuned to discriminate the τ signal from the CC DIS background at high missing transverse momentum. Since it is expected that quark or gluon induced jets in CC DIS, NC DIS and photoproduction processes have similar internal structures as characterised by the used jet observables, it is worthwhile to investigate the separation power of the MODT in a little modified framework. The CC DIS, NC DIS and photoproduction events are selected without requirements on the missing transverse momentum.

In this section it will be shown that if the same observables and the same CC DIS MC events without the $\not{p}_T$-cut are used, also good separation powers for CC DIS and photoproduction are obtained. And if the rejection of electrons in NC DIS events is under control, also a good separation can be achieved for NC DIS.

CC DIS

As can be seen in Figure B.1 the jet observable distributions of the CC DIS MC events without the $\not{p}_T$-cut looks very similar to the one with that cut (see Fig. 7.18). The separation power has even been slightly improved at similar efficiencies (see Fig.B.2). E.g for $D > 0.95$ the separation power rise from 210 to 230 at an efficiency of 33% for both frameworks. Without the $\not{p}_T$-cut the distributions of the jet transverse momenta are shifted to lower amounts in a way that the differences of the observable disributions of τ jets and CC DIS jets even grow.

Photoproduction

The Figures B.3 and B.4 show the observable distributions and the separation power functions for the photoproduction MC. Although the CC DIS MC was used as background sample the separation power is even better for separating photoproduction events as can be seen in these diagrams. This fact indicates that quark or gluon induced jets in photoproduction processes are even less collimated than the ones in CC DIS jets (compare Fig. B.3 with B.1).

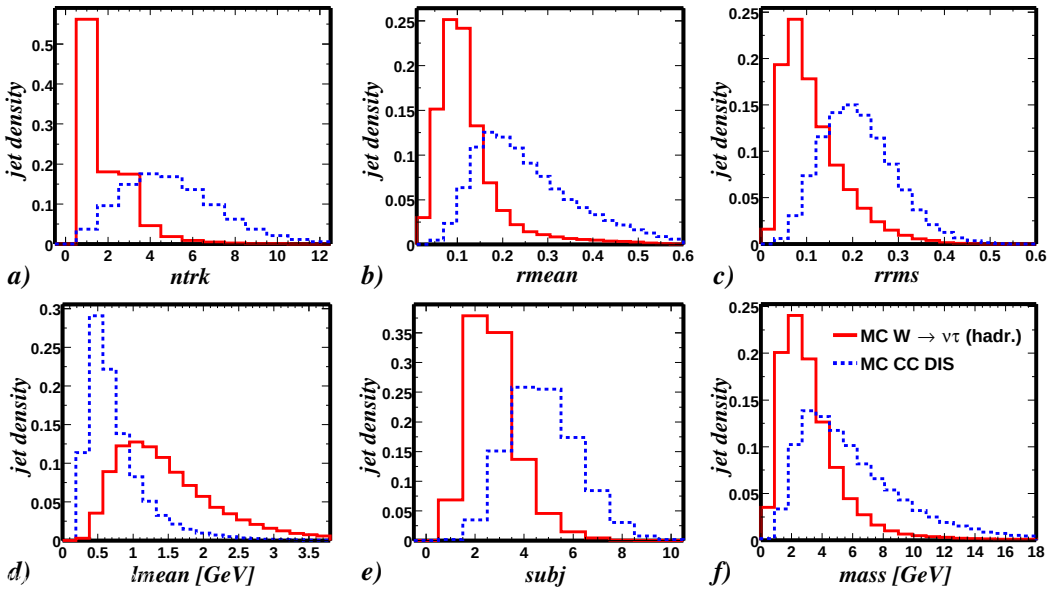

Figure B.1: The shape normalised distributions of the six jet observables without the $\not{p}_T$-cut. The solid line indcates the τ MC sample and the dashed line the CC DIS MC sample.

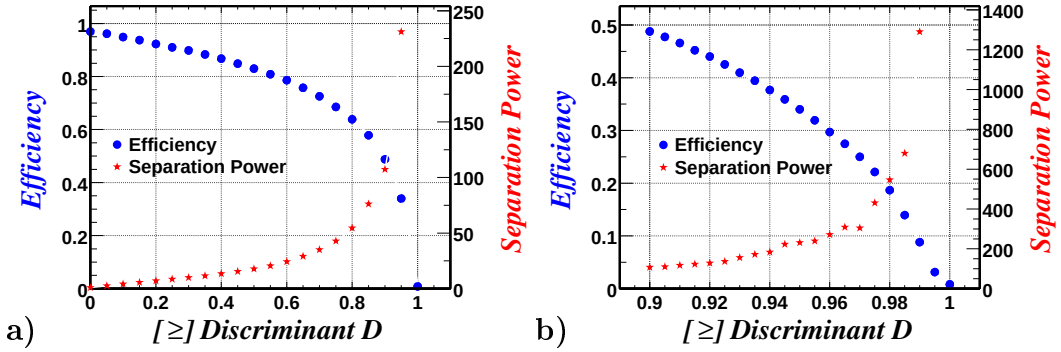

Figure B.2: Efficiency and separation power as a function of the discriminant cut for the τ and the CC DIS MC without the $\not{p}_T$-cut. The dots indicate the efficiency according to the scale on the left ordinate and the stars the separation power according to the scale on the right ordinate, respectively. The term '[≥]' denotes that the event is required to have at least one jet with the highest jet discriminant greater than or equal the x-value. (a) shows the whole discriminant range from 0 to 1, whereas (b) shows an expanded region.

NC DIS

The case for NC DIS events is not as promising as for CC DIS and photoproduction events. In Figure B.6 it can be seen that the maximal obtained separation power is only about 19. All observable distributions shown in Figure B.5 have a similar shape compared with those of CC DIS and photoproduction, except the one for *rmean*. The very high peak at very low *rmean* is an indication that there are still too many electrons left. This means the electron rejection scheme used

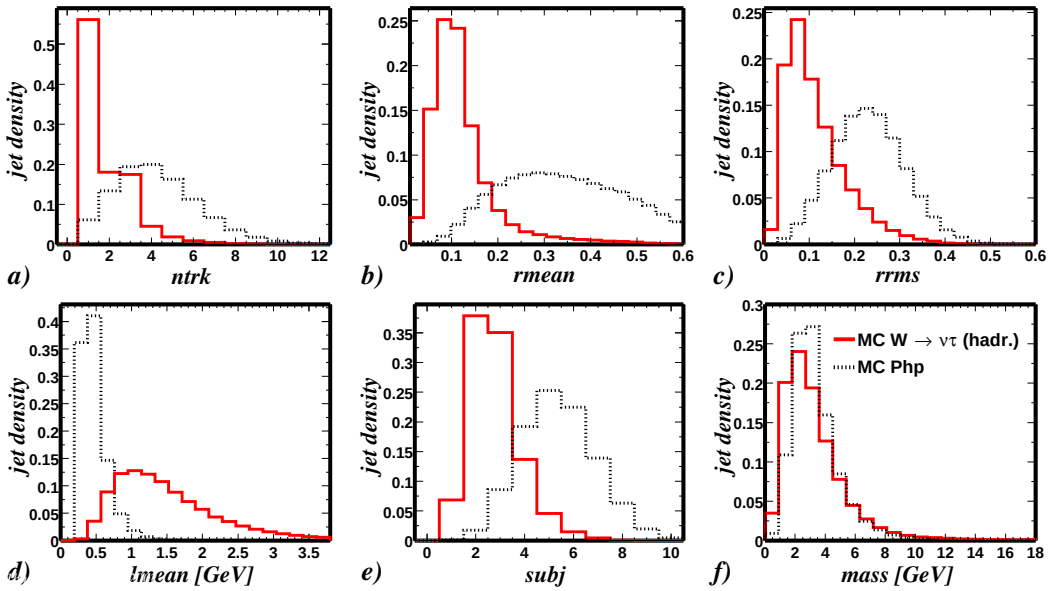

Figure B.3: The shape normalised distributions of the six jet observables without the $\not{p}_T$-cut. The solid line indicates the τ MC sample and the dotted line the photoproduction MC sample.

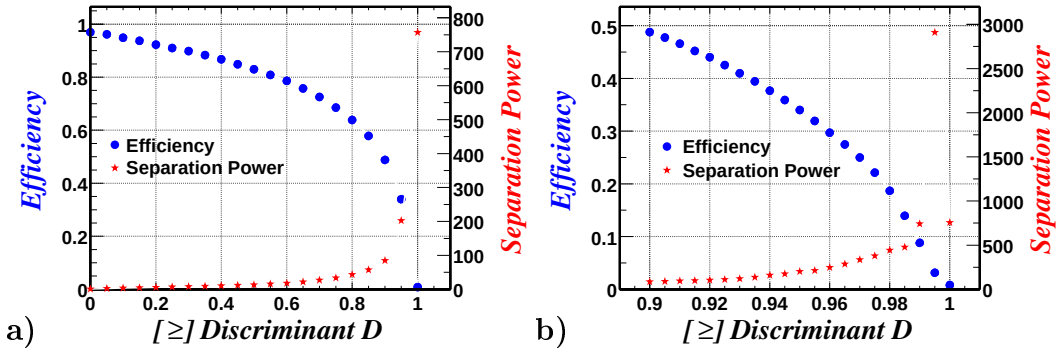

Figure B.4: Efficiency and separation power as a function of the discriminant cut for the τ and the photproduction MC without the $\not{p}_T$-cut. As background sample the CC DIS MC was used. The dots indicate the efficiency according to the scale on the left ordinate and the stars the separation power according to the scale on the right ordinate, respectively. The term '[≥]' denotes that the event is required to have at least one jet with the highest jet discriminant greater than or equal the x-value. (a) shows the whole discriminant range from 0 to 1, whereas (b) shows an expanded region.

so far is not fully efficient to reject electrons in NC DIS events. To improve the electron rejection could be a worthwhile task in the future, in order to investigate whether the separation power would improve.

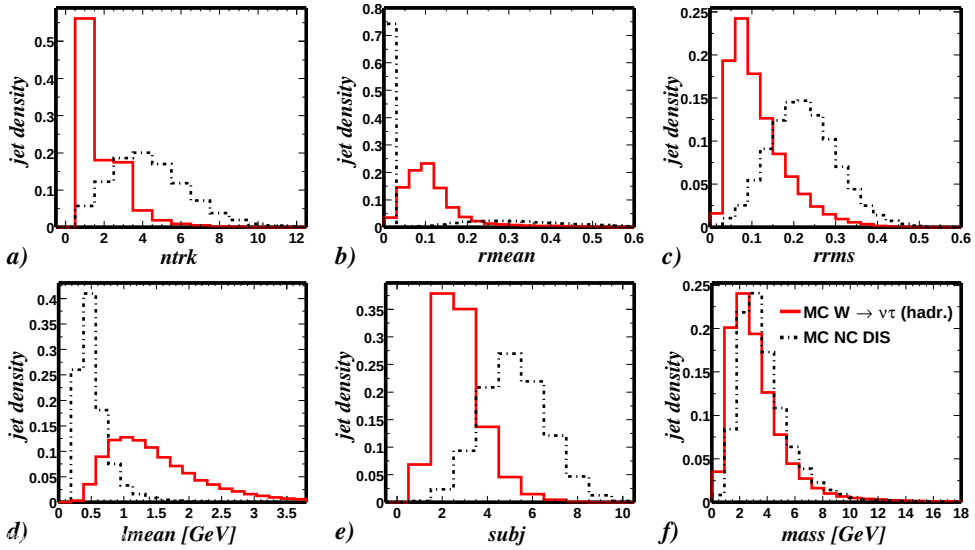

Figure B.5: The shape normalised distributions of the six jet observables without the $\not{p}_T$-cut. The solid line indcates the τ jets in the $W \to \nu\tau$ MC sample and the dashed-dotted line the jets and electrons in the NC DIS MC sample.

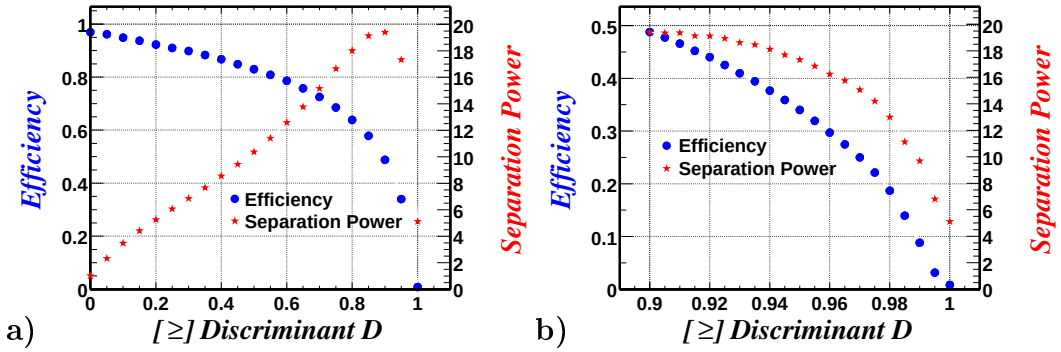

Figure B.6: Efficiency and separation power as a function of the discriminant cut for the τ and the NC DIS MC without the $\not{p}_T$-cut. As background sample the CC DIS MC was used. The dots indicate the efficiency according to the scale on the left ordinate and the stars the separation power according to the scale on the right ordinate, respectively. The term '[≥]' denotes that the event is required to have at least one jet with the highest jet discriminant greater than or equal the x-value. (a) shows the whole discriminant range from 0 to 1, whereas (b) shows an expanded region.

Conclusion

It has been shown that good separation of τ jets from jets in photoproduction and CC DIS are obtained without requiring much missing transverse momentum. The separation of τ jets from NC DIS jets can very likely be improved, if the rejection of electrons would be under control. The improvement of electrons in NC DIS events would be a worthwhile task in the future in order to investigate whether the τ jet discrimination can be improved in this way.

Bibliography

[1] S. Weinberg, Phys. Rev. Lett. 19 (1967) 1264;
A. Salam, Elementary Particle Theory, Ed. N. Svartholm (Almquist and Wiksells, Stockholm, 1969);
S.L. Glashow, J. Iliopoulos and L. Maiani, Phys. Rev. D2 (1970) 1285.

[2] Super-Kamiokande Collaboration, Y. Fukuda et al., Phys. Rev. Lett. 81 (1998) 1562;
Super-Kamiokande Collaboration, Y. Fukuda et al., Phys. Lett. B433 (1998) 9;
Super-Kamiokande Collaboration, Y. Fukuda et al., Phys. Lett. B436 (1998) 33;
SNO Collaboration, Q.R. Ahmad et al., Phys. Rev. Lett. 87 (2001) 071301.

[3] T. Kon, T. Kobayashi and S. Kitamura, Phys. Lett. 376 (1996) 227.

[4] H. Fritzsch and D. Holtmannspötter, Phys. Lett. 457 (1999) 186.

[5] ZEUS Collaboration, J. Breitweg et al., Phys. Lett. B471 (2000) 411.

[6] H1 Collaboration, C. Adloff et al., Eur. Phys. J. C5 (1998) 575.

[7] J. Dingfelder, Searches for $\not{R}_p$ SUSY and other exciting Phenomena at HERA, Talk given at HIGGS AND SUSY Conference, Orsay (France), March 19.-22. 2001.

[8] ZEUS Collaboration, HERA Luminosity Upgrade, DESY-HERA 98-05, Hamburg (Germany) (1998).

[9] U. Baur, J.A.M. Vermaseren and D. Zeppenfeld, Nucl. Phys. B325 (1989) 253.

[10] Particle Data Group, D.E. Groom et al., Europ. Phys. J. C15 (2000).

[11] E. Boos, M. Dubinin, V. Ilyinm A. Pukhov, V. Savrin, preprint INP MSU 94-36/358, 1994 (hep-ph/9503280)
in: Proc. of X Workshop on High Energy Physics and Quantum field Theory, ed. by B. Levtchenko, V. Savrin, Moscow (1996) 101.

[12] U. Baur, J.A.M. Vermaseren and D. Zeppenfeld, Nucl. Phys. B375 (1992) 3.

[13] ZEUS Collaboration, J. Breitweg et al., Phys. Lett. B479 (2000) 1-3, 37.

[14] ZEUS Collaboration, J. Breitweg et al., The Europ. Phys. J. C11 (1999) 3, 427.

[15] ZEUS Collaboration, J. Breitweg et al., The Europ. Phys. J. C12 (2000) 3, 411.

[16] ZEUS Collaboration, The ZEUS detector, Status Report 1993, U. Holm, Ed., Hamburg (Germany) (1993).

[17] H. Abramowicz and A. Caldwell, Rev. Mod. Phys. 71 (1999) 1275.

[18] A.T. Doyle, G. Grindhammer, G. Ingelman, H. Jung, (Eds.), Proc. Workshop Monte Carlo Generators for HERA Physics, DESY-PROC-1999-02, DESY, Hamburg (Germany) (1999) 714.

[19] R. Brun et al., GEANT 3.13, CERN DD/EE/84-1, Geneva (Switzerland) (1987).

[20] T. Sjöstrand, Comp. Phys. Comm. 82 (1994) 74.

[21] G. Corcella et al., HERWIG 6, CERN-TH/2000-284, Geneva (Switzerland) (2000);
G. Marchesini et al., Comp. Phys. Comm. 67, 465 (1992).

[22] A. Kwiatkowski, H. Spiesberger, H.-J. Möhring, Comp. Phys. Comm. 81 (1992) 155.

[23] G. Ingelman, A. Edin, J. Rathsman, Comp. Phys. Comm. 81 (1994) 381.

[24] L. Lönnblad, Comput. Phys. Comm. 71 (1992) 15.

[25] T. Abe, Comp. Phys. Comm. 136 (2001) 126.

[26] T. Carli and B. Koblitz, Adv. Comp. Analysis Techniques in Phys. Research (Batavia, USA, 2000), P. Bath and M. Kasemann, Eds., 110 (hep-ph/0011224).

[27] B. Koblitz, Search for Instanton-Induced Processes with the H1 Detector in Deep-Inelastic-Scattering Electron Proton Collisions at HERA, Hamburg University Ph.D. Thesis, April 2002.

[28] R. Sedgewick, Algorithms in C++, Addison Wesley, 1992, Chapter 26.

[29] ZEUS Collaboration, A Microvertex Detector for ZEUS, Proposal to the PRC, ZEUS-NOTE 97-006, Hamburg (Germany) (1997).

[30] J.R. Forshaw and M.H. Seymour, JHEP 9909 (1999) 009.

[31] R. Kerger, Search for the Lepton-Flavour Violating Process $ep \to \tau X$ in the e^+p Data of 1994-1997, Bonn University Ph.D. Thesis, March 2001.

[32] ZEUS Collaboration, S. Chekanov et al., Search for the Lepton-Flavor Violation in e^+p Collisions at HERA, DESY-01-222, Hamburg (Germany) (2001).

[33] K. Nagano, Measurement of the Charged Current e^+p Deep Inelastic Scattering Cross Sections at $\sqrt{s} = 300$ GeV, University of Tokyo Ph.D. Thesis, December 1998.

[34] A. Lopez-Duran and S. Schlenstedt, Electron Finder Efficiencies and Impurities. A Comparison between SINISTRA95, EM and EMNET, ZEUS-NOTE 99-077, Hamburg (Germany) (1999).

[35] S. Catani, Yu.L. Dokshitzer, M.H. Seymour and B.R. Webber, Nucl. Phys. B406 (1993) 187;
S.D. Ellis and D.E. Soper, Phys. Rev. D48 (1993) 3160.

Danksagung

Ganz besonders danken möchte ich Tancredi, der mir in diesem einem Jahr der Diplomarbeit nicht nur immer mit Rat und Tat zur Seite stand, sondern es auch verstand, mir seine Begeisterung für die Teilchenphysik zu vermitteln. Bedanken möchte ich mich auch bei Herrn Professor Klanner für seine sehr hilfreichen Hinweise und bei Frau Professor Naroska für die Begutachtung dieser Arbeit. Großer Dank gilt Dominik, der mir mir bei unzähligen Fragen, vor allem in der Einarbeitungszeit, aber auch später geholfen hat. Bedanken möchte ich mich bei Robert Kerger für seine Unterstützung und bei Birger für die Bereitstellung des Range-Searching-Quell-Codes. Thanks to James Ferrando for supporting me in running the EPVEC generator. Also thanks to Bruce Straub, Masahiro Kuze, Elisabetta Gallo and the whole *Exotics*-Group. Many questions were answered by Vincenzo, Magherita, Katarzyna and Alberto, thanks to them. Achim war immer ein sowohl kritischer, aber deswegen auch immer hilfreicher Ratgeber, sowohl in der Diskussion als auch bei der Durchsicht dieser Arbeit - vielen Dank. Besonderen Dank gilt auch Benjamin und Ingo für die anregenden Diskussionen. Natürlich bedanke ich mich bei allen Mitgliedern der gesamten Gruppe *Nukleare Metechnik*, die alle sehr aufgeschlossen und hilfreich waren und die alle gemeinsam eine so schöne Atmosphäre geschaffen haben, in der das Arbeiten wirklich sehr viel Spaß gemacht hat.

Erklärung

Ich erkläre hiermit ehrenwörtlich, daß ich diese Diplomarbeit selbstständig verfaßt, keine anderen als die angegebenen Hilfsmittel und Quellen verwendet, mich auch sonst keiner unerlaubten Hilfsmittel bedient und diese Diplomarbeit weder im In- noch im Ausland in irgendeiner Form als Prüfungsarbeit vorgelegt habe.

Chi Nhan Nguyen — Hamburg, 25. April 2002